Ricardo Miguel Ribeiro Adão

Bachelor Degree in Sciences of Physics Engineering

Development of a Nanoscale-Sensitive DNA Sensor using Functionalized Graphene Substrates and Fluorescence Lifetime Characterization

Dissertation submitted in partial fulfillment
of the requirements for the degree of

Master of Science in
Physics Engineering

Adviser: Prof. Dr. Ana G. Silva,
Assistant Professor,
Faculdade de Ciências e Tecnologia of UNL

Co-adviser: Dr. Jana B. Nieder,
Research Group Leader,
International Iberian Nanotechnology Laboratory

Examination Committee

Chairperson: Prof. Dr. Isabel Catarino
Raporteurs: Prof. Dr. Yuri Nunes
Member: Dr. Jana B. Nieder

FACULDADE DE
CIÊNCIAS E TECNOLOGIA
UNIVERSIDADE NOVA DE LISBOA

September, 2017

Development of a Nanoscale-Sensitive DNA Sensor using Functionalized Graphene Substrates and Fluorescence Lifetime Characterization

This document was created using the (pdf)LaTeX processor, based in the "unlthesis" template[1], developed at the Dep. Informática of FCT-NOVA [2].
[1] https://github.com/joaomlourenco/unlthesis [2] http://www.di.fct.unl.pt

Research Infrastructures Used

The laboratory work developed during this master thesis counted with the extensive use of International Iberian Nanotechnology Laboratory (INL) infrastructures:

- **Nanophotonics Facilities**: The main characterization component of the work required optical instruments and setups for techniques such as custom-built Fluorescence Lifetime Imaging Microscopy, ellipsometry, confocal Raman spectroscopy and dark-field optical microscope.
- **Cleanroom facilities**: Most of the nanofabrication work was developed in INL's cleanroom infrastructures for techniques such as plasma-ashing, spin-coating, Plasma-Enhanced Chemical Vapor Deposition and interferometry-based optical profilometry.
- **Nanochemistry Facilities**: Nanofabrication and general sample preparation required the use of INL's wet chemistry lab tools such as spin-coating, ultra-sound bath, vortex sample homogenizer, centrifuger and micropipettes.

"He who is certain he knows the ending of things when he is only beginning them is either extremely wise or extremely foolish; no matter which is true, he is certainly an unhappy man, for he has put a knife in the heart of wonder."
Tad Williams in The Dragonbone Chair (1988)

Acknowledgements

Throughout this work many have provided me with great support, both technical and emotional, whom I would like to thank:

To Prof. Dr. Ana G. Silva for providing such an extraordinary opportunity and for her tireless dedication and counseling.

To Dr. Jana B. Nieder for her expert advise, assertiveness and inspiring leadership. For her confidence and rewarding feedback.

To Dr. Pedro Alpuim and the *2D Materials and Devices* group for their expertise in graphene-based biosensing and for providing the graphene used in this work. In particular, to Dr. Rui Campos for his extensive cleanroom and lab guidance and assistance in the substrate transfer of graphene and DNA biosensor sample preparation. For his dedication to the project, which didn't stop at weekends or holidays. To Dr. Fátima Cerqueira, for performing the Raman spectroscopy measurements of the graphene samples.

To Dr. Dmitri Petrovykh for the orientation in the ellipsometry measurements. To Catarina Abreu, for her solicitude and cleanroom assistance. To Hélder Fonseca, for his cleanroom collaboration in the deposition of SiO_2 layers.

To Dr. Edite Figueiras, for her guidance in FLIM measurements, cleanroom and sample preparation. For her MATLAB scripts and skills, which were vital at the early stages of the developed software in MATLAB. To Dr. Christian Maibohm, for his expertise in laser optics and physics, for the fascinating discussions and his ever-cheerful and charismatic presence. To Dr. Oleksandr Savchuk, my vigorous table tennis partner, for his help in assembling the stage-top incubator and all the stress-releasing moments. To Dr. Óscar Silvestre, for group-activity creativity. To Thomas Exlager, for the late-night measuring sessions and cherishing episodes. To Ana Rita Faria and Raquel Gonçalves for their joviality when I most needed it.

To Dylan Marques, my dear friend and colleague, for his priceless support. For the good and the rough, the hilarious and frustrating moments together. For the precious brainstorming and for being the best flat-mate I could have wished for. To João Fernandes and his everlasting stress-releasing goofiness. To all my friends and family who have accompanied me through this amazing adventure. To my parents, for their endless love and support. To my brother, for making me proud every day.

To Ana Samouco, whose loving friendship has strengthen me through the difficult moments and inspired me to give the best of my effort.

Abstract

Fluorescence Lifetime Image Microscopy (FLIM) of nanostructured graphene substrates was used to measure the recently observed nanoscale distance-scaling of the fluorescence lifetime of dyes located in the vicinity of graphene sheets, at distances up to about 30 nm. The results were compared with a Resonant Energy Transfer (RET) theoretical model and used to establish an experimental fluorescence lifetime-to-nanoscale distance conversion function.

In the following, this nano-optical relation was used for the design of a Deoxyribonucleic Acid (DNA) biosensor. Graphene was functionalized with fluorescently labeled DNA molecular beacons that unfold during hybridization with complementary DNA, and thereby change the distance of the fluorescent dye from the graphene surface. The spatial distribution of DNA molecular beacons binding to the surface of a graphene flake was studied, as well as the temporal kinetics of the hybridization reaction using time-lapse FLIM measurements. The results showed a vertical ascent of a fluorescent label relative to the graphene surface with a distance extension that is in accordance with the expected molecular length of the specific DNA sequence used. Interestingly, an intermediate state associated to a distance of a few nanometers was identified with a lifespan of about 85 minutes.

The developed graphene-based DNA sensor was shown to enable optical detection of nanoscale distances in liquid media. These findings indicate that the fluorescence lifetime-based detection coupled with nanoscale interaction effects may find applications in various biosensing applications such as health and food-quality tracing.

For the processing of FLIM data, several fluorescence lifetime calculation algorithms were compared and integrated into a specially designed and implemented analysis software toolbox in MATLAB.

Keywords: Graphene; nanoscale distance sensing; fluorescence lifetime; FLIM; energy transfer; DNA biosensing; MATLAB

Resumo

Imagens de Microscopia de Tempo de Vida de Fluorescência (FLIM) de substratos de grafeno nano-estruturados foram usadas para a medição da recentemente observada alteração do tempo de vida de fluorescência de corantes quando localizados na vizinhança de grafeno para distâncias até cerca de 30 nm. Os resultados foram comparados com um modelo teórico de Transferência Ressonante de Energia (RET) e utilizados para o estabelecimento de uma função de calibração experimental entre tempo de vida de fluorescência e distâncias à nano-escala.

Posteriormente, esta relação nano-ótica foi utilizada para o desenvolvimento de um biossensor de Ácido Desoxirribonucleico (ADN). Substratos de grafeno foram funcionalizados com sinais moleculares (*molecular beacons*) de ADN que se desdobram durante a hibridização com ADN complementar, alterando a distância do corante fluorescente à superfície de grafeno. A distribuição espacial da ligação de sinais moleculares de ADN à superfície do grafeno foi estudada, bem como a cinética de reação de hibridização, usando medições de FLIM por lapso de tempo. Os resultados mostraram a ascensão vertical dos marcadores fluorescentes relativamente à superfície, com uma deslocamento total que está de acordo com o comprimento molecular esperado para a sequência de ADN utilizada. Curiosamente, um estado intermedio associado a uma distância de alguns nanómetros foi identificado, tendo este uma duração de cerca de 85 minutos.

Foi então demonstrado que o sensor de ADN desenvolvido permite a deteção ótica de distâncias à nano-escala em meio líquido. Estes resultados indicaram que a deteção baseada em tempo de vida de fluorescência, acoplada aos efeitos desta interação ótica à nano-escala pode ser utilizada em várias aplicações de biodeteção, tal como na saúde e no rastreamento da qualidade alimentar.

Para o tratamento de dados de FLIM, vários algoritmos de cálculo de tempo de vida foram comparados e integrados num programa de análise especificamente desenhado e implementado para o efeito, em ambiente MATLAB.

Palavras-chave: Grafeno; medição de distância à nanoescala; tempo de vida de fluorescência; FLIM; transferência de energia; biosensor de ADN; MATLAB

Contents

List of Figures

List of Tables

Acronyms

APD Avalanche Photodiode.

CPS Chance, Prock and Silbey.

CVD Chemical Vapor Deposition.

DMF Dimethylformamide.

DNA Deoxyribonucleic Acid.

FLIC Fluorescence Interference Contrast.

FLIM Fluorescence Lifetime Image Microscopy.

FRET Förster Resonance Energy Transfer.

FWHM Full Width at Half Maximum.

INL International Iberian Nanotechnology Laboratory.

IPA Isopropyl Alcohol.

IRF Instrument Response Function.

NA Numerical Aperture.

NHS N-Hydroxysuccinimide.

PBSE 1-Pyrenebutyric Acid N-Hydroxysuccinimide Ester.

PECVD Plasma-Enhanced Chemical Vapor Deposition.

PMMA Poly(methyl methacrylate).

PVA Polyvinyl alcohol.

RET Resonance Energy Transfer.

RPM Revolutions Per Minute.

SPC Single Photon Counting.

TCSPC Time-Correlated Single Photon Counting.

TIRF Total-Internal Reflection Fluorescence.

Chapter 1

Introduction

1.1 Motivation and importance of the work

Biosensing has been gaining more and more relevance as a technique in applications ranging from medical purposes to food-quality tracing, including the prevention of outbreaks of food-borne illnesses and in the combat against attempts of fraudulent malpractice in billion euro businesses. Particularly, the use of Deoxyribonucleic Acid (DNA)-based detection systems revolutionized biosensing for introducing reliable methods of biological fingerprinting. However, most of the established techniques for DNA biosensing merely output "on-off" electrochemical signals at the presence of specific molecules, which makes them poorly descriptive of the system and its interactions. A new generation of DNA biosensors however, rises with the application of graphene a sensing platform.

In recent years, graphene has been shown to hold extraordinary optical, electronic and mechanical properties, revealing a fascinating versatility for endless applications. Among its qualities, its strong non-radiative electromagnetic coupling to light-emitting molecules, has recently left its mark in the world of nanoscale distance sensing, for enabling a reversible distance-dependent fluorescence lifetime reduction when at the nanoscale vicinity of fluorescent dyes.

This work brings together the virtues of the two techniques by using the lateral resolution of Fluorescence Lifetime Image Microscopy (FLIM) for a spatial characterization of the biosensing platform and the nanoscale axial resolution provided by the interaction with graphene for the implementation of a DNA biosensor through the measurement of molecule-sized distances.

In particular, the DNA sequence of a port wine grape for the biosensor experiments exemplifies this biosensor applicability to the fingerprinting of port wine and food-origin validation.

1.2 State of the Art

At the beginning of this century, most high-resolution fluorescence-based microscopy techniques could only provide resolution in the lateral directions [1]. Indeed, only Total-Internal Reflection Fluorescence (TIRF) [2] and Fluorescence Interference Contrast (FLIC) [3] stood out for their resolution in the axial direction. However, these techniques (and many others) relied on the measurement of fluorescence intensity, which is highly vulnerable to intrinsic spatial and temporal fluctuations, mainly due to heterogeneous labeling and photobleaching. Alternatively, FLIM [4, 5] stood out for its independence of concentration and photobleaching [6] and great success in the labeling and study of dynamic live cellular structures [7, 8, 9], yet again it was only able to provide lateral resolution.

On a complementary level, fluorescent molecules have been known to interact with other molecules and theoretically studied since the 1940's [10, 11][1]. In 1948, Theodor Förster published in German his worldwide highly cited paper describing the principles of intermolecular energy transfer [11]. It described the resonant energy transfer between the oscillating dipoles of a fluorescence emitter and an energy acceptor in its surroundings, leading to what eventually became universally known by Förster Resonance Energy Transfer (FRET). In the 1960's the fluorescence lifetime of fluorophores near metal surfaces was studied [14], leading to the famous Chance, Prock and Silbey (CPS) model [15] and many other publications regarding the interaction of fluorescent molecules near metal interfaces, by the 1980's [16, 17]. More recently, the distance dependence of fluorescence quenching and lifetime reduction by metal nanostructures has been studied, such as gold nanoparticles [18, 19, 20]. In the last decade, axially-resolved nanometer and sub-nanometer accuracy optical rulers have been studied from interactions with metallic thin films [21, 22, 23], transparent conductive oxides [24] and ultimately for graphene [25, 26, 27, 28]. In particular, Gaudreau et al [25] experimentally quantified the distance dependence of fluorescence lifetime with the distance to graphene (see Figure 1.1) due to FRET. Their results are in good agreement with previously derived theoretical models [29, 30]. These works together opened new routes for innovation in biosensing technologies.

Simultaneously to the progresses in the understanding of interactions of fluorescent dyes with 2D layers and materials like graphene, in the field of biotechnologies, huge advances in DNA biochemistry were made. Last-decade research has provided a remarkable broadening of nanoscale biological understating and bio-applications, namely in the DNA biochemistry and biosensing areas [31, 32], which have great impact in health and food-quality tracing [33, 34]. Several DNA hybridization-based biosensors have been implemented [35] such as the hairpin DNA molecular beacon [36], which relies on the configuration change of a DNA-beacon (probe DNA) upon hybridization with a complementary target DNA [37, 38]

Particularly, a number of DNA-based biosensing devices has been developed with

[1] Original versions in German and translated to English in 2012 [12] and 1993 [13], respectively.

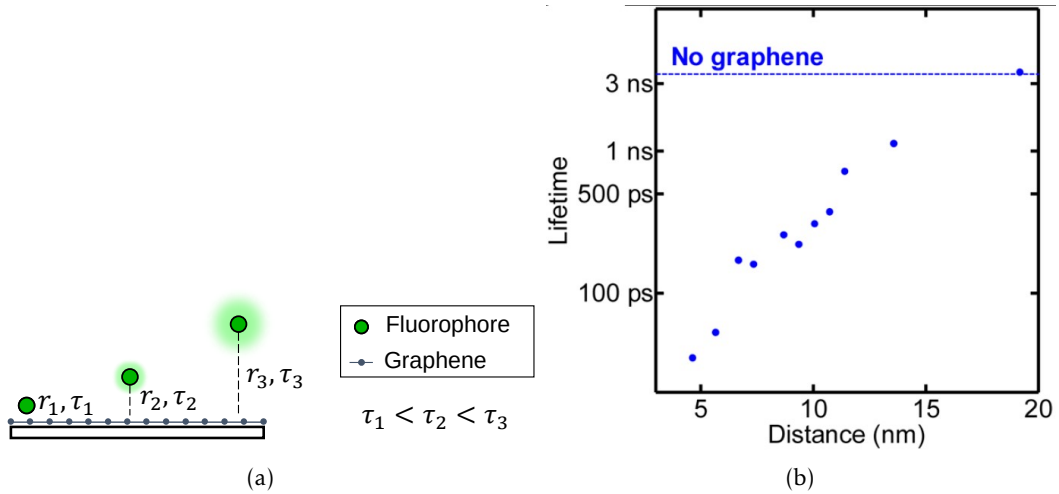

(a) (b)

Figure 1.1: Fluorescence lifetime dependence on distance to graphene. (a) Shorter distances yield stronger RET and therefore shorter lifetimes. (b) Experimental evidence of the interaction by Gaudreau et al [25].

applications ranging from medical purposes to food-quality tracing techniques [33]. In the latter scope, which encompasses the prevention of outbreaks of food-borne illnesses [33] and the combat against attempts of fraudulent malpractice in billion euro businesses [34].

1.3 Objectives and Goals

The main goals of this master thesis are: a) the study of the dependence of the fluorescence lifetime of fluorophores at nanoscale distances to graphene for the development of a nanoscale distance sensing technique, using recently described graphene near-field effects; and b) the validation of this technique's applicability in biosensing, by the development of a fluorescence lifetime-based DNA molecular beacon biosensor (Figure 1.2).

For this purposes, it is required the design and nanofabrication of a calibration sample that allows obtaining nanoscale distance information from fluorescence lifetime measurements and the surface functionalization of graphene with biosensor-probe DNA molecules, such that time-lapse FLIM measurements of the hybridization process upon the addition or target DNA molecules can be used as a biosensing technique.

In parallel with the experimental work, c) the implementation of a multifaceted analysis software in MATLAB to provide a user-friendly interface for the processing of FLIM data.

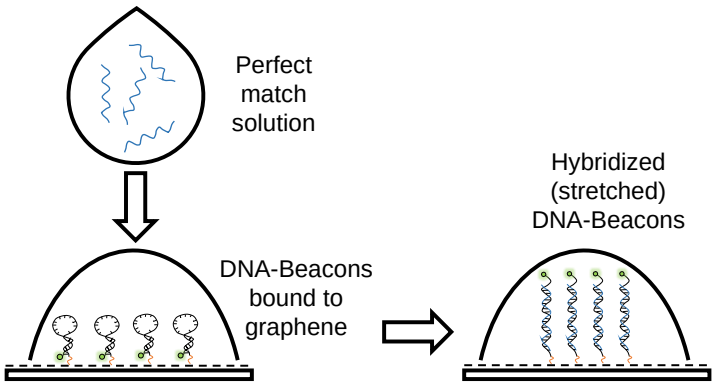

Figure 1.2: DNA-beacon biosensor experiment schematic. A graphene surface is functionalized with fluorescently labeled DNA-beacons (probe DNA) and the fluorescent lifetime is characterized before and after the addition of complementary (target) DNA. The hybridization of probe and target DNA produces a nanoscale increase in the fluorophore distance to graphene and therefore an increase in the fluorescence lifetime which, from the biosensing point of view is indicative of the presence of target DNA.

Chapter 2

Theoretical Background and Principles

2.1 Physical Principles

2.1.1 Fluorescence

Fluorescence is the emission of light by a molecule that has been excited by some form of electromagnetic radiation. In particular, it is the consequence of a radiative electronic transition from an excited state to a lower energy level. Following the Franck–Condon principle, when a molecule is optically excited it will most likely be excited onto a higher-energy vibrational level within the excited electronic level (see Figure 2.1). At that point, it will release part of it energy by non-radiative decay to reach the vibrational ground-state and finally return to the electronic ground state by means of either a nonradiative or a radiative decay (fluorescence emission). [39].

The measured fluorescence intensity I_f can be written as a function of overall detection efficiency k and fluorescence quantum yield ϕ_f as

$$I_f = k\phi_f I_0(1 - 10^{-\alpha cl}) \tag{2.1}$$

where k is the detection efficiency, ϕ_f is the quantum yield, α is the molar absorption coefficient, c is the molar concentration of the fluorescent dye and l is the light path length within the sample. The quantum yield is defined as

$$\phi_f \equiv \frac{\text{Number of photons emitted}}{\text{Number of photons absorbed}} = \frac{\text{Intensity of light emitted}}{\text{Intensity of light absorbed}} \tag{2.2}$$

Considering a simple two-level model as the one depicted in Figure 2.2, the number of molecules in the excited state s_1 varies with the difference between the number of molecules being excited from s_0 to s_1 and the number of molecules decaying from s_1 to s_0

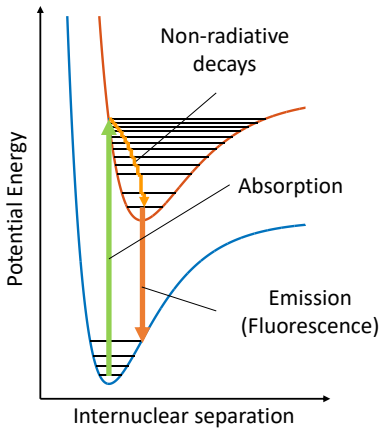

Figure 2.1: Fluorescence sequence. After radiation absorption, the molecule undergoes non-radiative decays to reach the vibrational ground-state. In the case of fluorescence, a radiative decay brings the molecule back to the electronic ground state. Figure adapted from [39].

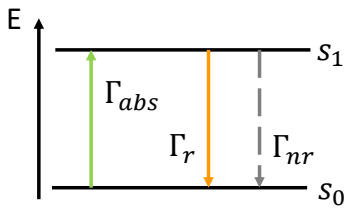

Figure 2.2: Two level energy scheme. Upon external excitation, the molecule is excited from the ground state s_0 to an excited state s_1 with an absorption rate Γ_{abs} and return to s_0 by means of a radiative or non-radiative decay, with the rate Γ_r and Γ_{nr}, respectively.

$$\frac{\mathrm{dn}_1}{\mathrm{d}t} = \Gamma_{abs} n_1 - (\Gamma_r + \Gamma_{nr}) n_1 \tag{2.3}$$

where Γ_{abs}, Γ_r and Γ_{nr} are the absorption rate and radiative and non-radiative decay rates, respectively.

Considering that an equilibrium state is achieved (steady-state), where the number of molecules transiting into the excited state s_1 matches the number of molecules transiting out of it, the rate $\mathrm{d}n_1/\mathrm{d}t$ becomes zero and Equation 2.3 can be written as

$$\Gamma_{abs} n_1 = (\Gamma_r + \Gamma_{nr}) n_1 \tag{2.4}$$

In such case, intensity of light absorbed $I_{abs} = \Gamma_{abs} n_1$ and the intensity of light emitted $I_{emi} = \Gamma_r n_1$ and the two intensities can be replaced in Equation 2.2 to form

$$\phi_f = \frac{\Gamma_r}{\Gamma_r + \Gamma_{nr}} \frac{n_1}{n_1} = \frac{\Gamma_r}{\Gamma_r + \Gamma_{nr}} \tag{2.5}$$

In other words, the quantum yield is the ratio of rate at which photons decay radiatively to the rate at which they are excited.

2.1.1.1 Absorption and emission spectra

Both the absorption and emission of radiation are energy-dependent and therefore wavelength dependent ($E = hc/\lambda$). As a consequence, the quantum yield, can be expressed as the sum of all steady-state fluorescence intensity per absorbed photons $F(\lambda_f)$ as function of the wavelength of the emitted photons λ_f [40] by

$$\phi_f = \int_0^\infty F(\lambda_f)\lambda_\mathrm{f}\mathrm{d}\lambda_f \tag{2.6}$$

where $F(\lambda_f)$ is the molecule's fluorescence emission spectrum and the shape of its plot is characteristic of the vibrational structure of the lower electronic state. For the absorption, the product $\alpha(\lambda_a)cl$ represents the wavelength-dependent absorption spectrum and the shape of its plot is characteristic of the vibrational structure of the excited upper state. Due to the different excitation-relaxation possible transition combinations, the emission and absorption spectra often show a mirror image of each other, with an overlap (Figure 2.3(a)). Figure 2.3(b) shows the measured emission spectra for fluorescein [41]. Wavelengths corresponding to the absorption-emission overlap may result in auto-excitation and therefore to the *inner filter effect*, which can induce significant changes in the emission spectrum and fluorescence lifetime.

Additionally, the absorption of light occurs most efficiently along the direction of its absorption moment [40]. For an unpolarized light source, only part of the radiation is absorbed and therefore the coupling between excitation light beam and average transition moment of the fluorophores must be taken into consideration in the excitation efficiency.

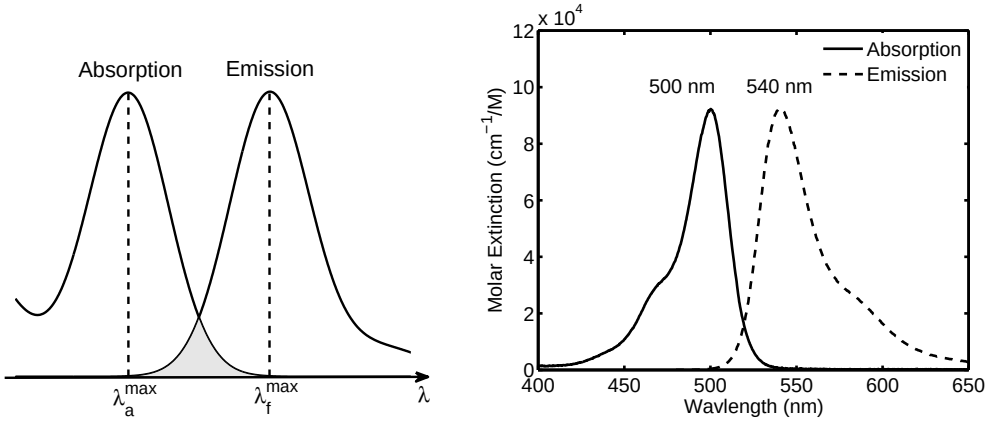

Figure 2.3: Absorption and emission spectra. Their shapes are characteristic of the vibrational structure of the upper and lower states, respectively. Absorption and emission often show a mirror-like image of each other and an overlap for certain wavelengths. (a) Derived model of the typical shapes of the spectra. Adapted from [40]. (b) Absorption an Emission spectra of fluorescein [41].

2.1.2 Fluorescence Lifetime

The fluorescence lifetime is the average time that an excited fluorescent molecule takes to decay from an excited state s_1 back to the ground state s_0. Considering a pulsed excitation source, at the moment when the excitation source is switched off the absorption rate Γ_{abs} becomes zero, and Equation 2.3 becomes [42]

$$\frac{\mathrm{d}n_1}{\mathrm{d}t} = -(\Gamma_r + \Gamma_{nr})n_1 \tag{2.7}$$

whose solution is:

$$n_1(t) = n_1(0)\, e^{-(\Gamma_r+\Gamma_{nr})t} = n_1(0)\, e^{-\frac{t}{\tau_f}} \tag{2.8}$$

where τ_f is the fluorescence lifetime

$$\tau_f = \frac{1}{\Gamma_r + \Gamma_{nr}} \tag{2.9}$$

Interestingly, the quantum yield from Equation 2.5 can be related to the fluorescence lifetime as

$$\phi_f = \tau_f \Gamma_r \tag{2.10}$$

which replaced in Equation 2.1 expresses the fluorescence intensity dependence on the fluorescence lifetime.

According to Equation 2.8, the fluorescence intensity over time assumes the form of an exponential decay whose fluorescence lifetime τ_f is an intrinsic characteristic of the fluorophore (see Figure 2.4(a)). In practice however, apart from single-molecule measurement conditions, a measured fluorescence decay is most likely the result of the contribution from several fluorophores in the sample, which may have different lifetimes. In such cases, the measurement will take the form of multi-exponential decay

$$I(t) = \sum_i^n (I_{i0} e^{-t/\tau_i}) \tag{2.11}$$

where the relative intensity $I_{i0}/\sum_i^n I_{i0}$ of each lifetime is proportional to their concentration and quantum yield[1]. In this case, a weighted average lifetime is commonly defined by

$$\tau_f = \frac{\sum_i^n (I_{i0}\tau_i)}{\sum_i^n I_{i0}} \tag{2.12}$$

Figure 2.4(b) shows the difference in shape between a single (full line) and double (dashed line) exponential curve. In the double exponential curve $I_{10} = I_{20} = 1/2$, both

[1] A first order Taylor approximation of Equation 2.1 yields $I_f \approx k \log(10) \phi_f I_0 \alpha c l$ for low concentrations and therefore I_f is proportional to ϕ_f and c

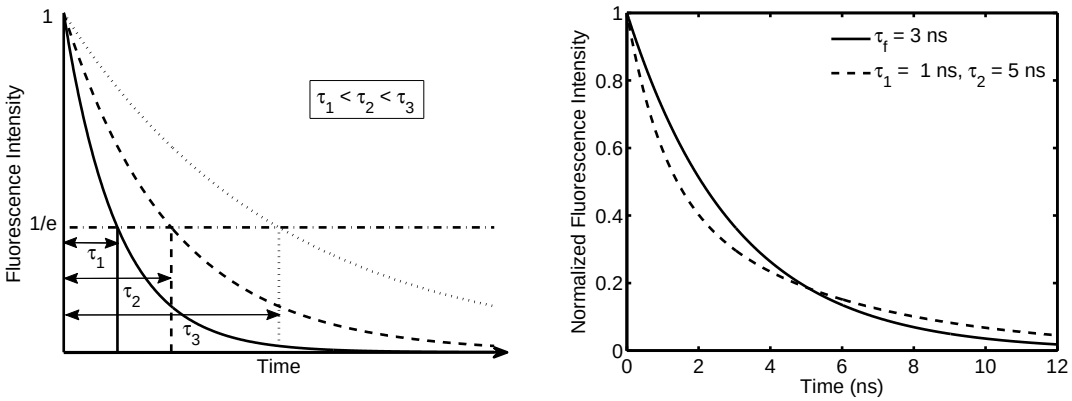

Figure 2.4: Fluorescence lifetime. (a) The influence of lifetime in the shape of the decay curve for a single-exponential decay. (b) Single (full line) and double-exponential (dashed line) decays. Both curves have an average lifetime of 3 ns, however the dashed curve decreases sharply until 3 ns and smoothly afterwards.

curves have an average lifetime of 3 ns, however the two curves carry very distinct information. Different lifetimes may surge due to different fluorescent species or due to the occurence of lifetime reduction mechanisms.

2.1.3 Fluorescence Quenching and Lifetime Reduction

The fluorescence lifetime, quantum yield and emission spectrum can be affected by the surrounding medium. In particular, the fluorescence intensity can be quenched by means of physical or chemical interactions with *quenchers* [40, 42].

Four different mechanisms can be defined as [43]: Non-radiative complex formation, where the energy is used in the chemical formation of a non-fluorescent product (Figure 2.5(a)); Collision quenching, where the energy is lost to another molecule by physically colliding with it (Figure 2.5(b)); Re-absorption, where a photon with energy within the absorption-emission overlap is emitted by a fluorophore and absorbed by another (Figure 2.5(c)); and Resonance Energy Transfer (RET), where there is a radiationless electromagnetic energy transfer from a fluorophore to a quencher by means of a resonant interaction (Figure 2.5(d)).

Collision quenching and RET are examples of *dynamic quenching*, for the number of light emitters remains constant, but the fluorescence lifetime decreases. RET is a physical interaction that depends on the dimensionality of the acceptor, which can assume the form of a single molecule (point dipole - 0D), an array of molecules (1D), a surface (2D) or a bulk material (3D). In particular for this work, the main interest lies on the study of distance-dependent RET to a graphene surface - 2D.

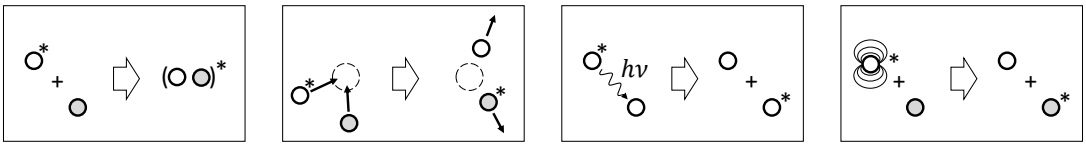

Figure 2.5: Energy transfer mechanisms. (a) Non-radiative complex formation. (b) Collision quenching. (c) Re-absorption. (d) Resonant Energy Transfer

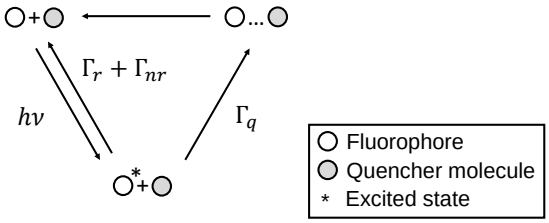

Figure 2.6: Dynamic quenching scheme. A fluorophore is excited with an incident energy $h\nu$ and decays with the sum of radiative and non-radiative decay rates Γ_r and Γ_{nr}, respectively. Upon interaction with a quencher molecule, an additional dynamic quenching decay rate Γ_{dq} appears. Figure adapted from [40]

2.1.3.1 Dynamic quenching and Stern-Volmer kinetics

The Stern-Volmer kinetics are usually applied for interactions between fluorophores and single molecules (0D), however, its elucidating equations can be generalized for acceptors with any dimensionality. The schematic image of Figure 2.6 shows a simplistic model of the dynamic quenching. The fluorophores are excited with a photon energy $h\nu$ and decay back to the ground state with a total rate $\Gamma_r + \Gamma_{nr}$, as they would in free-solution. At the presence of quencher molecules Q, they transfer part of their energy to Q at the dynamic quenching rate Γ_q. Therefore, the number of fluorophores at the excited state n_1 as function of time can be written as:

$$n_1(t) = n_1(0)e^{-(\Gamma_r+\Gamma_{nr}+\Gamma_q)t} = e^{-t/\tau} \tag{2.13}$$

where the lifetime τ can be expressed as

$$\tau = \frac{1}{\Gamma_r + \Gamma_{nr} + \Gamma_q} \tag{2.14}$$

According to Equation 2.10, the quantum yield comes as $\phi = \tau\Gamma_r$ and therefore

$$\phi = \frac{\Gamma_r}{\Gamma_r + \Gamma_{nr} + \Gamma_q} \tag{2.15}$$

It is thus clear that both the fluorescence intensity and lifetime are reduced due to the presence of energy acceptors by a quenching rate Γ_q.

2.1.4 Resonant Energy Transfer

A great work has been done by Theodore Förster on this topic to develop a theoretical model of what is commonly known by the Förster Resonance Energy Transfer (FRET). Its formalism describes the interaction between two classical point-dipoles (donor and acceptor molecules) and quantifies the decay rate of the donor as function of the distance to the acceptor; its detailed deduction can be found in ref. [43].

Section 2.1.4.1 presents the main equations of this model and Section 2.1.4.2 presents an intuitive adaptation for the case of RET to a graphene surface.

2.1.4.1 Förster Resonant Energy Transfer

According to Equation 2.14, the decay rate $\Gamma = 1/\tau$ can be written as

$$\Gamma = \Gamma_0 + \Gamma_q \tag{2.16}$$

where $\Gamma_0 = \Gamma_r + \Gamma_{nr}$ is the unquenched total decay rate.

In Förster's model the rate of energy W_A being transferred to the acceptor is evaluated by solving the motion equation for a forced Harmonic oscillator. The quenching rate Γ_q is then calculated through

$$\frac{\mathrm{d}W_A}{\mathrm{d}t} = \Gamma_q W_D \tag{2.17}$$

where W_D is the energy being irradiated by the donor. The quenching rate results in

$$\Gamma_q = \frac{1}{\tau_0}\left(\frac{R_0}{r_{AD}}\right)^6 \tag{2.18}$$

where $\tau_0 = 1/\Gamma_0$ is the free-space lifetime of the donor, R_0 is the Förster distance and r_{AD} is the distance between the donor and the acceptor. Replacing Γ_q in Equation 2.16, the total decay rate then becomes

$$\frac{\Gamma}{\Gamma_0} = 1 + \left(\frac{R_0}{r_{AD}}\right)^6 \tag{2.19}$$

The Förster distance R_0 corresponds to the distance at which the transfer rate Γ_T matches the rate of decay $\Gamma_r + \Gamma_{nr}$. In other words, the probability of an excited molecule do decay to its ground state by fluorescence or any other non-radiative process is equal to the probability of transferring its energy to an acceptor at distance R_0. The dependence of the decay rate with d^{-6} is characteristic of the point dipole-point dipole interaction [44], which is not the case for graphene. However, Equations 2.18 and 2.19 can now be used explain the model developed by Blanco et al [45] and experimentally verified by Gaudreau et al [25] for the graphene case, without having to go through all the calculations.

2.1.4.2 Resonant Energy Transfer to Graphene

The resonant energy transfer to a graphene is described by modeling the graphene surface as two-dimensional array of acceptor dipoles (Figure 2.7). As a result, Equations 2.18 and 2.19 are changed by the dimensionality of the acceptor [26] n according to

$$\Gamma_q = \frac{1}{\tau_0}\left(\frac{R_0(n)}{r}\right)^{3+n} \tag{2.20}$$

$$\frac{\Gamma}{\Gamma_0} = 1 + \left(\frac{R_0(n)}{r}\right)^{3+n} \tag{2.21}$$

where $R_0(n)$ is the dimension-dependent Förster distance. To a 3D, 2D, 1D or 0D acceptor corresponds an $n = 0$, 1, 2 or 3, respectively. Therefore, to the case of graphene $n = 1$ and the decay rate assumes a distance dependence of the form r^{-4} [46].

Gaudreau et al quantified the Förster distance R_{0G} for the case of graphene [25]

$$R_{0G} = \frac{9\kappa^2\alpha\lambda^4}{256\pi^3(\epsilon+1)^2} \tag{2.22}$$

which replaced in Equation 2.21 results in

$$\frac{\Gamma}{\Gamma_0} = 1 + \frac{9\kappa^2\alpha}{256\pi^3(\epsilon+1)^2}\left(\frac{\lambda}{r}\right)^4 \tag{2.23}$$

where κ^2 is dipole orientation coefficient, α is the fine structure constant ($\alpha \approx 1/137$ [47]), λ is the donor emission wavelength and ϵ is the dielectric constant of the surrounding medium. A first approximation of the dipole orientation factor ($0 < \kappa^2 < 4$) yields $\kappa^2 = 2/3$ for an isotropic distribution [48].

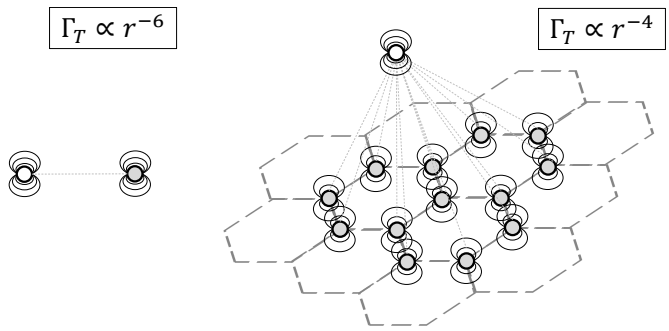

(a) (b)

Figure 2.7: Dependence of the transfer rate on the dimensionality of the acceptor (Equation 2.20). (a) Transfer between two point-dipoles: acceptor is 0D $\Rightarrow n = 3$. (b) Transfer between a point-dipole and a two dimensional array of point-dipoles: the acceptor is 2D $\Rightarrow n = 1$

In practice, it is customary to calculate fluorescence lifetimes, rather than decay rates. Equation 2.23 can be easily converted to lifetime by calculating its inverse form ($\tau/\tau_0 = (\Gamma/\Gamma_0)^{-1}$).

$$\frac{\tau}{\tau_0} = \frac{1}{1 + R_{0G}/r^4} \tag{2.24}$$

2.2 Optical Technologies

This section presents a brief introduction to some of the optical techniques used in this work, whose results are discussed in chapter 4. It includes the concepts of Time-Correlated Single Photon Counting (TCSPC) for the measurement of time-resolved fluorescent decays; confocal microscopy and how it can be used in Fluorescence Lifetime Imaging Microscopy (FLIM) and Raman spectroscopy - the Raman spectrum of graphene is also mentioned; and ellipsometry.

2.2.1 Time-Correlated Single Photon Counting

Time-Correlated Single Photon Counting (TCSPC) is the measurement of the arrival times from single photons emitted from a fluorescent dye upon repetitive excitation with short laser pulses [49]. Within the scope of time-resolved spectroscopy, the main challenge is the measurement of emission times which may last from hundreds of picoseconds to a few tens of nanoseconds, with intensities that may be as low as that of a single-fluorescent molecule regime.

Alternatively to photo-diodes and a fast oscilloscopes, which may at first glance seem like a reasonable approach, TCSPC systems overcome such difficulties by the repetitive and precisely timed registration of single photons. Using the excitation pulse as time reference, a histogram of single photon's arrivals is recorded in order to reproduce the time-resolved intensity profile of a fluorescence decay.

A key factor in this technique is to guarantee that indeed only single photons are counted (and not the summed effect of the arrival of multiple photons). This requirement can (and must) be met by the sufficient low light intensity that reaching the detector, such that the probability of a detecting a photon arrival between two laser pulses becomes virtually zero. In other words, the detection of more than one photon per pulse is forced to be highly unlikely (Figure 2.8(a)).

As photons are counted, a fluorescence time arrival histogram is built to trace the shape of the fluorescence exponential decay (Figure 2.8(b)).

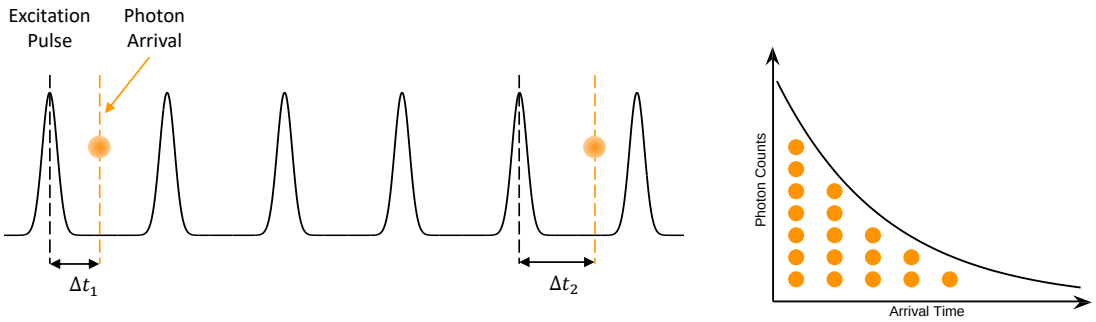

(a) (b)

Figure 2.8: Time Correlated Single Photon Counting. Adapted from ref. [49]. (a) The measurement is performed at low fluorescent signal intensities so that the detection of more than one photon per pulse is highly unlikely. When photon is measured, its time arrival relative to the laser pulse is stored. (b) A histogram of photon time arrivals is built to produce a measure of the fluorescence decay curve.

2.2.2 Confocal Microscopy

Confocal microscopy is a sample- or laser-scanning microscopy technique, which uses light collimation to increase the spatial resolution. Figure 2.9 shows a schematic of the principle. The field of illumination projected onto the sample is reduced by placing a first pinhole in the microscope axis and focusing the light beam with a lens. Then, the field of view is limited further by placing a second pinhole in the image plane, confocally to the illumination spot in the sample and to the first pinhole [50]. The measured signal is therefore originating from a very small volume of the sample, at a fixed working distance to the objective.

In confocal setups, an image is formed by scanning across the sample with a stage, whose step size, combined with the spot size of the light beam defines the resolution of the image. This setup can be used for a number of imaging modes, including Raman spectroscopy, fluorescence spectroscopy and FLIM.

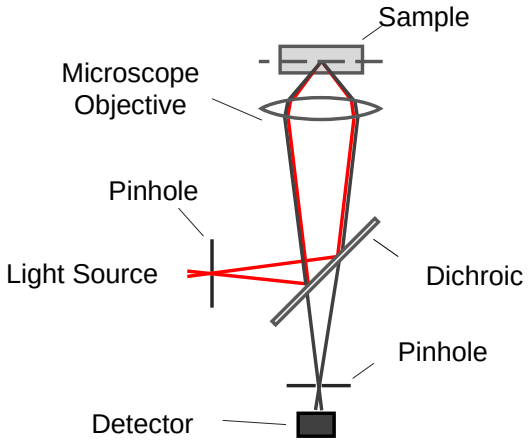

Figure 2.9: Principle of a confocal microscope. A first pinhole reduces the illumination on the sample and a second reduces the field of view coming from it. Thus, the measured signal comes from a very small volume of the sample.

2.2.3 Fluorescence Lifetime Imaging Microscopy (FLIM)

Fluorescence Lifetime Image Microscopy (FLIM) is the spatial mapping of the fluorescence lifetime distribution of a sample [4]. Typically TCSPC is combined with confocal microscopy in FLIM setups [51]. The main advantages of FLIM over its fluorescence intensity-based alternatives are due its independence of intensity variations (namely due to photobleaching [6]), fluorophore concentration and excitation light-path, which can be difficult to control in biological systems [5].

TCSPC systems require much shorter integration times compared with their analogic electronics, such as time-gated detection [52].

The spatial resolution of a confocal microscope is diffraction-limited, according to Abbe's diffraction limit: $d = \lambda/(2n\sin\theta)$ and therefore approximately half the excitation wavelength (typically between about 200-350 nm for visible wavelengths.

FLIM is widely used in cell biology studies [4, 7, 8, 9], as it can be used to monitor biochemical processes such as protein interactions [53], measurement of intracellular pH [54] and temperature [55].

2.2.4 Raman Spectroscopy

Raman spectroscopy is typically used for the observation of vibrational and rotational states in a molecule, by means of inelastic (Raman) scattering of photons [56].

Raman scattering (named after the Indian Physicist Chandrasekhara Venkata Raman [57]) arises from the resonant interaction between the polarization of the incident light and the polarization of the molecule. The result of such interaction leads to a change in the dipole moment of the molecule with respect to its vibrational motion, creating

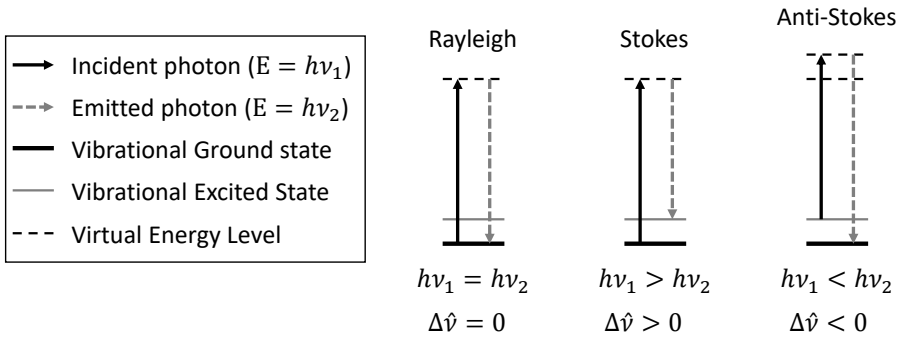

Figure 2.10: Energy level diagram of Rayleigh and Raman scattering. The energy of the emitted photon is shifted from that of the absorbed photon depending on the initial and final vibrational state.

an induced dipole moment in the molecule (virtual energy level), whose emitted light contains the observed Raman scattering [58, 59].

The scattering of light can occur in three different ways usually known by Rayleigh, Stokes and anti-Stokes scattering. The Rayleigh scattering corresponds to the fraction of light with the same frequency as the incident light, whereas in the Stokes and anti-Stokes scattering there is a shift in the emitted photon energy which can either be lost (Stokes) or gained (anti-Stokes) in the molecule.

If the incident and emitted photons have energies $E_1 = h\nu_1$ and $E_2 = h\nu_2$, respectively, where $\nu = c/\lambda$ is the light frequency and λ is the wavelength, then the difference in wavenumber of the two photons is given by

$$\Delta\hat{\nu} = \frac{1}{c}(\nu_1 - nu_2) = \left(\frac{1}{\lambda_1} - \frac{1}{\lambda_2}\right) \tag{2.25}$$

This is known by the Raman shift and is usually measured in cm^{-1}(see Figure 2.10). In terms of energy levels, when a molecule is excited from the vibrational ground state to the an excited virtual energy level, it can return to either the vibrational ground state (Rayleigh scattering) or to an excited vibrational level (Stokes scattering). Alternatively, if the molecule is already at an excited vibrational state before being excited into a virtual energy level, then it may de-excite onto an energy level with lower energy than that of its initial state (anti-Stokes scattering). Hence, the Raman shift $\Delta\hat{\nu}$ carries information of the intrinsic vibrational energy structure of the molecule, which can be used as a fingerprint for molecule identification purposes.

2.2.4.1 Raman Spectrum of Graphene

Monolayer graphene is most commonly identified by considering three main features in its Raman spectrum commonly denoted by the D, G and 2D peaks ($\Delta\hat{\nu_D} \approx 1360\ \text{cm}^{-1}$, $\Delta\hat{\nu}_G \approx 1570\ \text{cm}^{-1}$, $\Delta\hat{\nu_{2D}} \approx 2722\ \text{cm}^{-1}$, respectively) [60]. The D peak is associated with impurity defects of graphene, the G peak reflects the lattice symmetry of graphene and

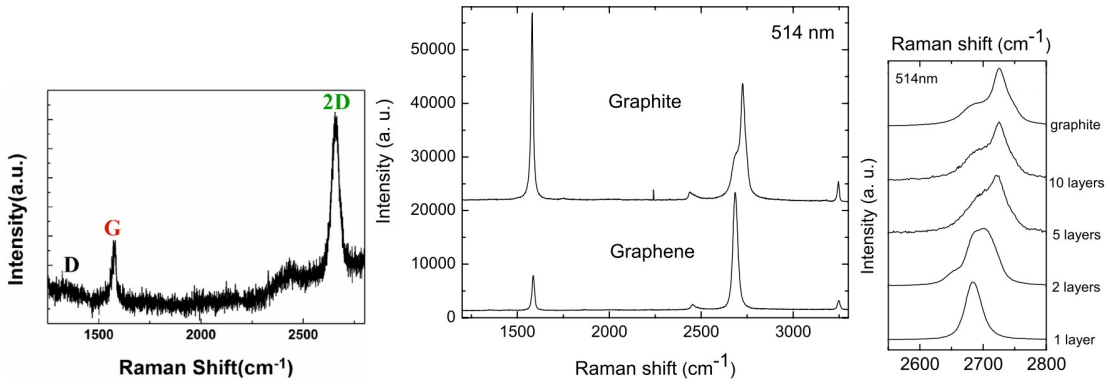

Figure 2.11: Raman features of graphene. (a) Monolayer graphene Raman spectrum [60]. (b) Comparison of Raman spectra of graphite and graphene [61]. (c) Comparison of the Raman spectra for different layers in multi-layer graphene.

order degree of carbon atoms and the 2D peak is the result of a second-order process involving two phonons with opposite momentum [60, 61] - see Figure 2.11(a).

In simpler terms, a low intensity of the D peak can be interpreted as an indicator of the graphene quality, and the G and 2D peaks can be regarded as the fingerprint peaks of Graphene, where an intensity ratio of peaks 2D over G larger than 2 is a typical feature of monolayer graphene. In that sense, Figure 2.11(b) shows a comparison between the Raman spectra of graphite and monolayer graphene, highlighting the difference in the intensity ratio of peaks 2D over G for the two cases and the broadening of the 2D peak from a single Lorentzian for the case of graphene to a double Lorentzian peak shape for the case of graphite. Indeed, as is shown in Figure 2.11(c) this double-peaked shape of the 2D component intensifies progressively with the number of layers.

Raman spectroscopy measurements can also be performed in a confocal setup, for spatial mapping of the Raman features of a sample.

2.2.5 Ellipsometry

The geometric orientation of the electric field of a propagating monochromatic light beam can be expressed in terms of two transverse components $\mathbf{E}_p$ and $\mathbf{E}_s$. Plotting the electric filed vector $\mathbf{E} = \mathbf{E}_p + \mathbf{E}_s$ over a full oscillation cycle leads to an elliptical shape - the polarization ellipse (Figure 2.12(a)).

The name ellipsometry arises from the measurement of the polarization ellipse. Briefly, ellipsometry is a measurement of the change in the polarization of a beam of light upon reflection on a surface - usually coated with a thin film (Figure 2.12(b)). In practice, the measurements are compared with models such that optical parameters like the thickness d, refractive index n or extinction coefficient k of thin film can be extracted. In summary, if the incident and reflective fields are written as function of their phases (neglecting z and ωt) [62]

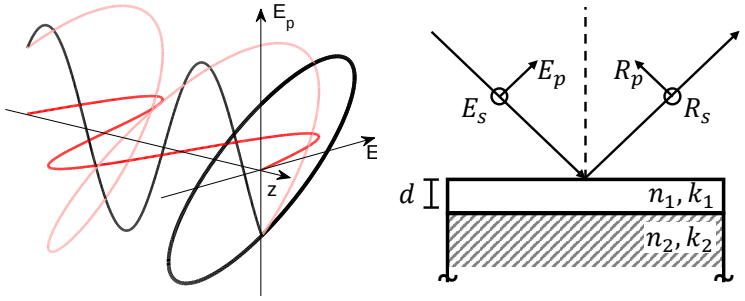

(a) (b)

Figure 2.12: Ellipsometry. (a) Polarization ellipse of propagating light. (b) Reflection of an incident beam on a film with thickness d, refractive index n_1, and extinction coefficient k_1.

$$E_m = E_{0m} e^{i\alpha_m} \tag{2.26}$$

$$R_m = R_{0m} e^{i\beta_m} \tag{2.27}$$

where $m = (p, s)$, then the main ellipsometry quantities are the amplitude ratio

$$\tan(\Phi) = \frac{R_{0p}/E_{0p}}{R_{0s}/E_{0s}} \tag{2.28}$$

and the phase angle

$$\Delta = (\beta_p - \beta_s) - (\alpha_p - \alpha_s) \tag{2.29}$$

where E_{0p}, E_{0s}, α_p and α_s are the parallel (p) and perpendicular (s) components of the incident electric field E and the respective polarization phases before reflection and R_{0p}, R_{0s}, β_p,β_s are the parallel and perpendicular components of the reflected field R and the respective polarization phases after reflection.

2.3 Biomolecular Technologies

In recent years, several biofunctionalization techniques were developed for the implementation of sensitive, accurate and relatively simple DNA sensors [35]. In the scope of this master thesis a so-called hairpin molecular DNA beacon is employed. This section presents a very brief introduction of the biological background regarding DNA hybridization and surface functionalization required for the understanding of hairpin molecular DNA-beacon biosensors.

2.3.1 Molecular DNA-beacon Technology

Deoxyribonucleic Acids (DNA) are sequences of nucleobases (usually in the form of double-stranded helices) which encode the genetic information of all living beings. [63].

Nucleic acid hybridization is the bonding between two complementary single-stranded nucleic sequences to form double-stranded DNA sequences [64]. The bonds are established between complementary nucleobases. For the case of DNA, adenine (A) binds with thymine (T) and guanine (G) binds with cytosine (C). A perfect-match between two single-stranded DNA molecules occurs when the sequence of nucleobases in one of them completely matches the complementary of the other.

Nowadays, custom DNA sequences are established as commercially available technology to be ordered upon interest. Particularly, if the sequence is such that there is complementarity between the nucleobases at two ends of the molecule, the molecule is said to be self-complementary and single-stranded molecules can fold onto themselves to form double-stranded like loop structures such as is shown in Figure 2.13.

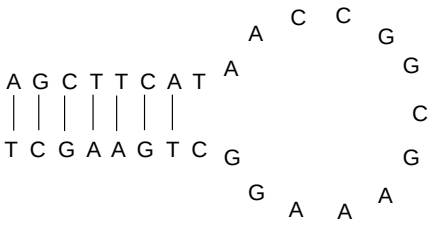

Figure 2.13: Self-complementarity of DNA beacon. When single-stranded, the molecule assumes a folded configuration. DNA beacons are commercially available where at the endgroup a fluorescent dye is attached.

2.3.2 Chemical Surface Functionalization Technologies

Chemical surface functionalization is the modification of the chemical properties of a surface. Among its rather vast range of applications, it is widely used for promoting surface bio-compatibility and, in particular, for the binding of DNA molecules, which can be used for biosensing applications [65].

The attachment of DNA molecules to graphene surfaces can be performed by using a linker molecule that establishes a connection between them. Figure 2.14(a) shows an example of a 1-Pyrenebutyric Acid N-Hydroxysuccinimide Ester (PBSE). The butyric pyrene group of the PBSE-linker binds to graphene noncovalently, but irreversibly (See Figure 2.14(b)) and the reactive succinimide ester conjugates with the amino-labeled oligonucleotides of the DNA molecule [66, 67].

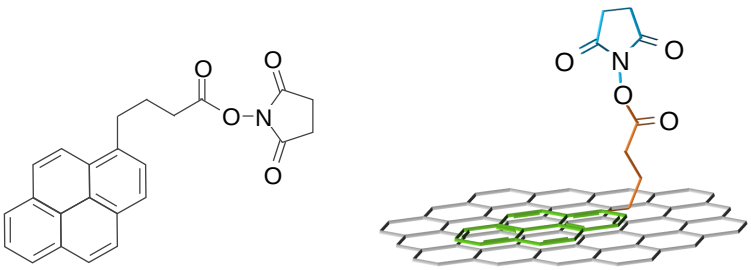

(a) (b)

Figure 2.14: 1-Pyrenebutyric acid N-hydroxysuccinimide ester (PBSE) linker molecule. (a) Schematic of the molecule. (b) 3D representation of bonding with graphene.

Chapter 3

Methods and Materials

This chapter presents a description of the experimental techniques and procedures used throughout the preparation and characterization of samples throughout this thesis. Section 3.1 lists the commercial equipment used and describes in more detail the custom-built FLIM setup used for the fluorescence lifetime characterization. Section 3.2 presents the experimental details and procedures for the nanofabrication of a fluorescence lifetime-distance calibration sample and the functionalization of graphene with fluorescently labeled DNA beacons for the development of a DNA biosensor.

3.1 Experimental Setups and Sample Preparation Techniques

3.1.1 Nanofabrication and Nanocharacterization Setups

This section refers particularly to the main commercial equipment used in this thesis. The main tools used for the nanofabrication/characterization in the cleanroom facilities of International Iberian Nanotechnology Laboratory (INL) included: The wet benches and fume hoods, used for sample cleaning and transfer of graphene from Cu foil to a glass substrate; Plasma Asher (PVA Tepla GIGAbatch 360M - Figure 3.1(a)), used for graphene removal from the backside of Cu foil; Photoresist Coater (Karl Suss Gamma Cluster - Figure 3.1(b)), used for deposition of Poly(methyl methacrylate) (PMMA) film on graphene sample; Plasma-Enhanced Chemical Vapor Deposition (PECVD) (SPTS MPX CVD - Figure 3.1(c)), used for deposition of SiO_2 spacers in calibration sample; Optical Profilometer/Interferometer (Oceon Optics NanoCalc XR - Figure 3.1(d)), used for measuring the thickness of SiO_2 spacers.

From the wet-chemistry labs, a spin-Coating (APT Spin150 - Figure 3.1(e)) was used for the deposition of a fluorescently doped PMMA layer.

Figure 3.1: Cleanroom equipment[(a)-(d)]; Wet chemistry equipment (e); Optics equipment [(f),(g)]. (a) Plasma Asher. (b) Resist coater. (c) PECVD. (d) Optical profilometer/interferometer. (e) Spin-coater. (f) Confocal Raman spectroscope. (g) Ellipsometry system. (h) Optical bright and dark field microscope.

From the NanoPhotonics facilities, the characterization tools used included: Confocal Raman Spectroscopy (Witec Alpha 300R - Figure 3.1(f)), used for the characterization of graphene; Ellipsometry System (Woollam M-2000 - Figure 3.1(g)), used for the measurement of the thickness of fluorescent thin film; Bright and Dark-field Optical microscope (Nikon Eclipse LV100ND - Figure 3.1(h)), used for the imaging of graphene sample in dark field mode.

3.1.2 Custom-Built FLIM setup

The fluorescence lifetime study performed in this thesis was performed with a custom made FLIM setup, whose schematic is shown in Figure 3.2. A picosecond pulsed laser

source (467nm, 70ps, and at variable repetition rate – typically operated at 20MHz, PLP-10, Hamamatsu) is coupled to an inverted microscope setup RM21 (MCL), equipped with the oil immersion objective Nikon CFI plan APO 100x (NA: 1.45, 0.17 WD 0.13), with a combined micro and nanoscanner (NanoLPS200, MCL), and an Avalanche Photodiode (APD) detector (PD50CTD, MPD), which is placed in quasi-confocal configuration to focus the signal onto a small surface area. The laser is mounted on the optical table and the beam profile cleaned up using a spatial filter composed of a pair of lenses (f1=50 mm and f2= 50 mm, LA4148-A, Thorlabs) with f1 focused onto a 100 μm pinhole. A shadow mask is used to control the illumination and a clean-up filter (470.0 nm, 470FS10-25, Thorlabs) is used for securing the monochromaticity of the laser sources. The beam expander system is composed of a pair of lenses (f1=40 mm and f2= 250 mm, AC254-040-B and AC254-250-B, Thorlabs) that is integrated into a cage system, and which is directly connected with the RM21 body for high stability of the setup. A kinematic 30 mm fluorescence filter cube (DFM1/M, Thorlabs) is mounted directly at the end of the 500 mm cage system. The filter cube is used to mount a 480LP Dichroic (F38-482, AHF Analysentechnik) and the long-pass filter (from AHF, F76-472). At the bottom of this kinematic cube, a mirror guides the emission signal towards the output port where it is focused via a lens onto an APD detector.

The TCSPC is implemented using a single-photon counting card (SPC130, Becker&Hickl) to which the sync of the pulsed laser source and the detector output (NIM pulses) are fed. An incubator with an electrically heated chamber and stage top incubator's controller (UNO-T-H-PREMIXED, H301-MCL-NANO-LPS, Okolab) is used for temperature and humidity control of the sample.

3.1.2.1 Measurement of the Instrument Response Function

The Instrument Response Function (IRF) is the temporal response of the TCSPC system to an infinitely short light pulse. Its shape and width is characteristic of the specific TCSPC setup used for the measurement and it describes the temporal resolution of the setup. The resolution may be determined by different hardware components such as the pulse with of the laser or the read-out speed of the detector. In the specific case of the used FLIM setup, where a picosecond laser with 70 ps short pulses was used, the temporal resolution limiting device is the detector. The resolution is predominantly limited by the transit-time spread of the photoelectrons on their path through the detector [68].

The IRF should be characterized experimentally for each setup. The experimentally determined IRF is often used in fluorescence lifetime fitting algorithms, as tested in Section 4.3. In this work it was measured using a sample with an ultrafast decay, where a saturated aqueous KI (potassium iodide) solution[1] was used to chemically reduce the fluorescence lifetime of fluorescein [69].

[1] The highly saturated KI solution was prepared with equal volume of water and KI.

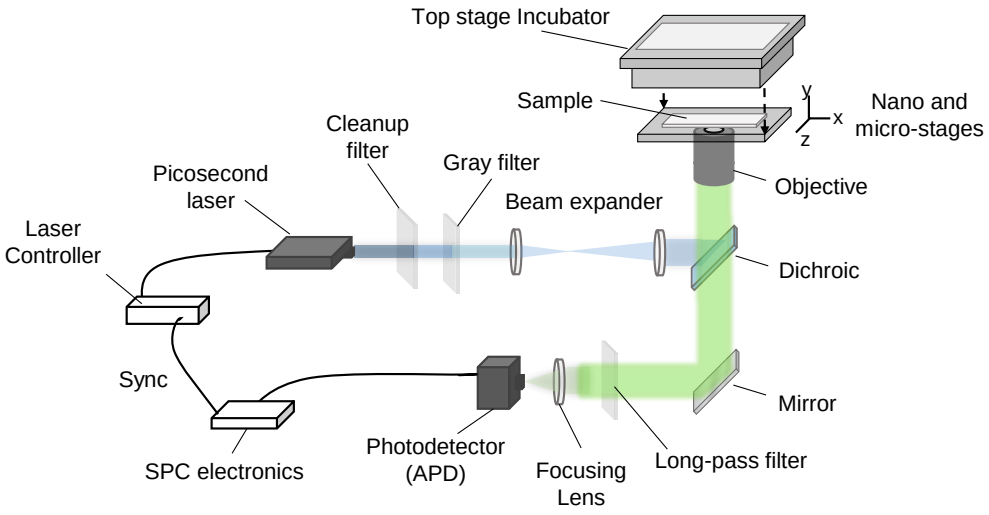

Figure 3.2: Scheme of the custom built FLIM setup used in this thesis. A picosecond laser is expanded and guided to an inverted microscope equipped with a high NA objective and an APD in confocal geometry. Suited filters guide the laser to the sample, while longer wavelength emission can pass the dichroic filter as well as the long pass filter placed in front of the detector. The APD generates NIM pulses which are read out by fast SPC electronics allowing the collection of TCSPC traces. The sample is scanned via nano- and micropositioning system, while temperature and humidity of the sample are controlled via a top stage incubator.

3.2 Sample Preparation and Characterization

The experimental procedure of this master thesis was divided into two main phases: the nanofabrication of a fluorescence lifetime-distance calibration sample and the development of a fluorescence lifetime-based DNA-Beacon biosensor, whose laboratorial details are presented in Sections 3.2.1 and 3.2.2, respectively.

3.2.1 Fabrication of a Nanostructured Calibration Sample

The preparation of this sample was divided into three main components: The growth and transfer of the graphene sheet onto the glass substrate, the deposition of the SiO_2 stair-like structure (Figure 4.1(b)) on top of the graphene, and the deposition of a fluorescent dye on top of that structure.

3.2.1.1 Transfer of graphene to glass substrate

The graphene is not grown directly on any given substrate but rather on a temporary substrate and then transferred onto the final substrate. The transfer procedure is summarized in Figure 3.3.

All the graphene used in this master thesis was prepared prior to this work and provided by the 2D Materials and Devices group of the Quantum Materials, Science and Technology Department - INL The graphene transfer was performed under the close orientation of Dr. Rui Campos.

The acquired samples consisted on a Cu foil with graphene grown on both sides (Figure 3.3(a)). Because only one graphene sheet from each Cu foil could be transferred onto a new substrate, the graphene in one of the sides of the Cu foil had to be removed by plasma ashing[2] (Figure 3.3(b)). Following, a PMMA thin film was spin-coated on the graphene side[3] (Figure 3.3(c)). This temporary substrate provided the physical support for the graphene once the Cu foil was dissolved away with a $FeCl_3$ solution[4] (Figure 3.3(d)). After several water rinsing iterations to clean any $FeCl_3$ residues, the transfer process was completed by scooping the sheet onto a microscope glass coverslip (Figure 3.3(e)) and dissolving the PMMA layer in an acetone bath[5] (Figure 3.3(f)).

Having finalized the graphene transfer process, confocal Raman measurements were used to probe the graphene surface coverage and monolayer character. The confocal Raman measurements were performed by Dr. Fatima Cerqueira. The results of this analysis are shown in Section 4.1.1.1.

[2]Time: 6 minutes; Gas flow rates: (O_2 200 sccm), (Ar 200sccm); chamber temperature: 50 Celsius; pressure: 0.60 mbar; voltage: 1500 mV; power: 230 W; frequency: 2.43 GHz

[3]Rotation speed: 16000 RPM; soft-baking temperature 80 Celsius.

[4]For each iteration: 5 minutes in 0.48 M $FeCl_3$, 5 minutes in water, 30 minutes in 2% HCl

[5]The ample was dipped in acetone and left overnight, followed by a 2 hour 300° bake

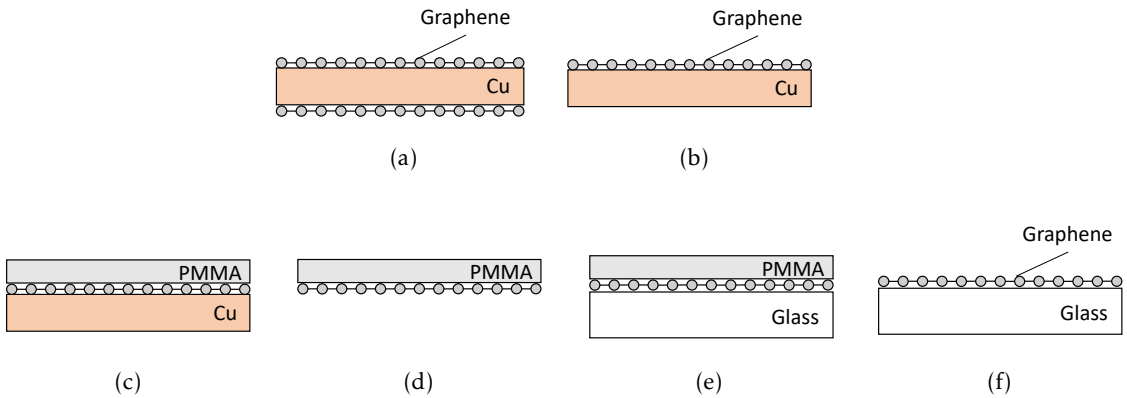

Figure 3.3: Graphene deposition and transfer process. (a) CVD-grown graphene on both sides of a Cu foil. (b) Graphene is plasma-ashed from one side. (c) A PMMA thin film is spin-coated on the graphene. (d) Cu foil is dissolved using a $FeCl_3$ solution. (e) The sheet is transferred onto a microscope glass coverslip. (f) The PMMA film is dissolved in acetone and the transfer process is finished.

It is important to mention that this procedure was performed twice - a first time for the nanofabrication of the calibration sample, and a second time for some of the DNA-biosensor samples, as the first batch was not enough for all the samples. As it shall be discussed in Section 4.1.2.2, the graphene from the two batches had very different surface coverages, but their monolayer character was similar.

3.2.1.2 SiO_2 Stair-like Nanostructure Deposition

For the study of the fluorescence lifetime as function of fluorophore distance to a graphene substrate, a SiO_2 stair-like structure was deposited on top of the graphene substrate, according to the schematics presented in Figure 4.1(b). The SiO_2 depositions in the cleanroom facilities were performed with the support of Dr. Edite Figueiras and Hélder Fonseca.

The design developed for this calibration sample is shown in Section 4.1.1. The objective was to nanofabricate a structure which would introduce well defined spacings between the graphene substrate and a fluorescent dye (Figure 4.1(a)). Ideally, the spacings would start a 0 nm (dye sitting directly on top of graphene) and increase up to 21 nm in 3 nm steps (7 SiO_2 depositions). The depositions were preformed by successive PECVD, where a shadow mask (large microscope coverslip) was moved 1.5 mm after each deposition[6]. For this calibration, several attempts for depositing 3 nm were performed, from which a 0.801 $nm.s^{-1}$ deposition rate was found. The sequence of depositions and expected thicknesses are shown in Table 3.1.

[6]Gas flow rates: (N_2O 1420 sccm), (SiH_4 10 sccm), (N_2 392 sccm); pressure: 6 mTorr; chamber temperature: 75 Celsius, power: 30 W

Table 3.1: Deposition times for depositing a 100 nm SiO_2 layer on an auxiliary Si wafer and seven 3 nm SiO_2 layers on both auxiliary and graphene sample. The deposition times were derived by considering a deposition rate of 0.789 $nm.s^{-1}$ for the 100 nm and 0.801 $nm.s^{-1}$ the 3 nm.

	Auxiliary Si wafer		Graphene sample	
Deposition #	time (s)	Thickness (nm)	Time (s)	Thickness (nm)
0	126.77	100	0	0
1	3.745	103	3.745	3
2	3.745	106	3.745	6
3	3.745	109	3.745	9
4	3.745	112	3.745	12
5	3.745	115	3.745	15
6	3.745	118	3.745	18
7	3.745	121	3.745	21

The thickness of SiO_2 depositions is usually measured by means of an optical interferometer, which is specifically calibrated for SiO_2 films on top of a Si (reflective) substrate, and thus there was no direct way for measuring the layer thicknesses deposited on top of the graphene. This problem has been worked around by previously depositing a 100 nm SiO_2 layer on a Si wafer[7] and simultaneously exposing this sample to the same PECVD depositions as the graphene sample. Assuming a similar SiO_2 deposition rate for the graphene and SiO_2 substrates, an optical interferometer profile was acquired from the latter sample in order to estimate the SiO_2 thickness in the graphene sample.

3.2.1.3 Spin-coating of a thin fluorescently labeled polymer layer

After the nanofabrication of the calibration sample's SiO_2 structure, a fluorescently doped Polyvinyl alcohol (PVA) layer was deposited by spin-coating. Each sample was prepared on a (18×18) mm glass coverslip using 0.02 μl of 5 mM fluorescein on Isopropyl Alcohol (IPA) and 200 μl of 0.1% PVA ($^{w}/_{w}$) in water.

The spin-coating conditions and the concentrations of PVA and fluorescein were optimized to produce to reduce the layer thickness while keeping a measurable fluorescence intensity. Lower PVA concentration produces a thinner film with lower fluorescence intensity (less volume to be excited). Higher fluorescein concentration produces stronger fluorescence intensity, however, too high concentration leads to self-excitation, which increases its fluorescence lifetime and should therefore be avoided. For the spin-coating, it was found that dropping the solution on a still sample would create inhomogeneities, while dropping it on a fast rotating sample would result in a lack spin-time of control. Hence, this procedure was divided in two steps (according to Table 3.1), where a first 500 Revolutions Per Minute (RPM) step was used for dropping the solution (dropping time at ≈ 10 s) and a second 3000 RPM step was used for the actual spin-coating process.

[7] This 100 nm SiO_2 layer was used exclusively for enhanced interferometer accuracy purposes, as it is much easier to sense distances around 100 nm than distances very close to zero.

Table 3.2: Parameters for the double stepped Spin-coating of fluorescein-doped layer.

Step	Duration (s)	Speed (RPM)	Acceleration (RPM.s^1)
1	20	500	3000
2	60	3000	3000

These conditions were optimized by performing iterative ellipsometry measurements for characterizing the thickness of the spin-coated layer. The ellipsometry measurements were performed with the support of Dr. Dmitri Petrovykh. The ellipsometry measurements required well known reflective substrates, so the different spin-coating procedures were first tested on auxiliary Si wafers and the results for the final conditions are presented in Section 4.1.1.3.

The nanofabricated calibration sample was then characterized using FLIM in each SiO_2 step in order to characterize the fluorescence lifetime as function of the fluorophore distance to graphene. The results are shown in Section 4.1

3.2.2 Functionalization of Graphene Surface with Fluorescent-Labeled DNA Beacon

This section presents the laboratorial procedures for the development of a functionalized graphene DNA-beacon biosensor, using the nanometer-sensitive lifetime measurements. The derived biosensor design is presented in Section 4.2.1 and the derived experiment for the biosensing is summarized in Figure 1.2.

A graphene surface was functionalized with fluorophore-labeled DNA-beacons and characterized with FLIM. Then, a DNA-target (perfect match) solution was added and time-lapse FLIM images were acquired on the same location as before in order to monitor the hybridization process. Table 3.3 shows the particular nucleobase-sequence of the probe and target DNA molecules used[8].

3.2.2.1 Biosensor Sample Preparation

The samples were prepared on (18×18) mm^2 glass coverslips. The experimental procedure was performed with the help of orientation of Dr. Rui Campos according to the following steps:

Table 3.3: Sequence of nucleobases of the DNA molecules used for the testing of a hairpin molecular DNA-Beacon biosensor.

Designation	Sequence
Probe	5' - AGC TTC ATA ACC GGC GAA AGG CTG AAG CT - 3'
Target	5' - AG CTT CAG CCT TTC GCC GGT TAT GAA GCT - 3'

[8]Metabion International AG, 3Atto488, HPLC, 0.2 μmol, dry, QC: MALDI-TOF, DNA Oligo

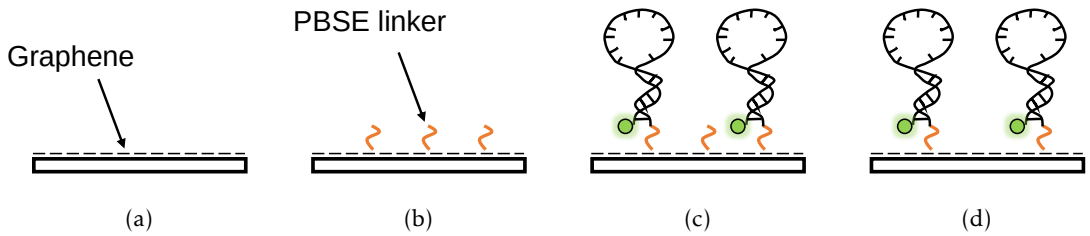

Figure 3.4: Surface functionalization procedure. (a) Graphene substrate. (b) Graphene functionalization with PBSE linker. (c) Drop-casting of biosensor-probe DNA. (d) Passivation of surface with ethanolamine to remove remnant PBSE.

1. Functionalization of the graphene with PBSE linker molecule (10 μL drop of a 10 mM solution in Dimethylformamide (DMF)). The solution was drop-casted on the surface and allowed to react for 2 hours followed by rinsing with DMF, H_2O and drying with N_2 (Figure 3.4(b));

2. A 10 μl drop of 10 μM probe DNA was left overnight, in wet chamber at 4 ^{o}C, to react via N-Hydroxysuccinimide (NHS) reaction with the ester of PBSE (Figure 3.4(c));

3. The DNA-modified surface was rinsed with buffer (0.75 M NaCl + 75 mM trisodium citrate) and, in order to passivate the remaining of the surface, 10 μl of 100 mM solution of ethanolamine (10 mM PB, pH 8.5) was allowed to react for 30 minutes with the molecules of PBSE that did not react with the amino group of the probe DNA (Figure 3.4(d)).

Figure 3.5(a) shows a derived molecular model for the final configuration of the probe DNA in the biosensor. Each sample has essentially the size of a 10 μl solution drop, which allowed for the preparation of multiple samples in a single graphene substrate (Figure 3.5(a)).

The biosensing was tested using a 10 μL drop of 10 μM target DNA solution .

3.2.2.2 Biosensor Experiment

Testing the biosensor required the addition of the DNA-target solution during FLIM measurement sessions, which required the production of home-made plastic sample holders (see Figure 3.5(b)).

After the optimization of the measurement conditions, a temperature and humidity control chamber was coupled to the nanoscan stage of the FLIM to prevent sample evaporation during long measurements (Figure 3.5(c)). The humidity level to prevent evaporation was kept constant using water-soaked paper towel inside the chamber and keeping the lid closed.

Several iterations were performed in order to optimize sample preparation parameters such as the sample rinsing after DNA-probe addition and sample holder development

and coupling technique, so that a better lifetime contrast could be obtained in the FLIM images.

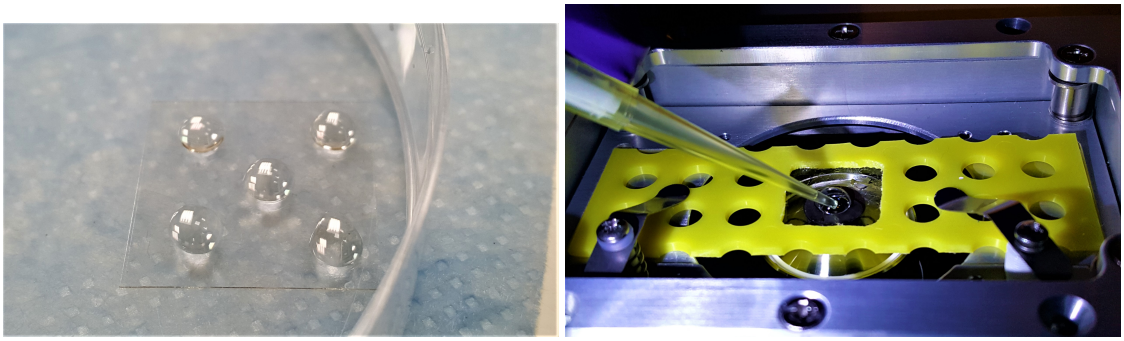

(a) (b)

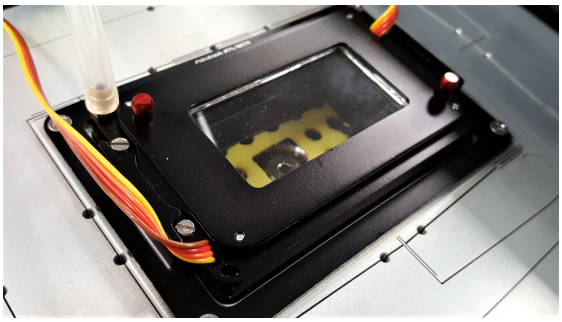

(c)

Figure 3.5: Fluorescence lifetime-based DNA molecular beacon biosensor experiment. (a) Five 10 μl samples drop-casted on a graphene surface on a microscope glass coverslip. (b) Addition the target DNA solution during FLIM measurement session. (c) Temperature and humidity control chamber mounted on the nanopositioning stage of the of the FLIM setup to prevent sample evaporation.

Chapter 4

Results And Discussion

This chapter is divided into four sections: Section 4.1 shows a study of the Nanoscale distance quenching of a fluorescent dye near graphene; Section 4.2 shows the development of a DNA biosensor through the study of the interaction of DNA-beacons with complementary DNA, using fluorescence lifetime to probe nanoscale distance changes between fluorescent labels and graphene during hybridization; Section 4.3 describes and compares the lifetime determination algorithms used in this thesis; Section 4.4 describes the data analysis software for MATLAB implemented in this thesis.

4.1 Study of Graphene Nanoscale Distance Quenching

Recent theoretical [70] and experimental [25] publications show that a fluorescent dye can undergo efficient energy transfer to a graphene sheet by means of a FRET interaction (Section 2.1.4).

The first objective of this work was the nanofabrication of a calibration sample such that the fluorescence lifetime of a fluorescent dye could be measure as function of the distance to graphene, using FLIM. This section describes the design conceived for this structure and the characterization results of the nanofabricated sample.

4.1.1 Design and Fabrication of a Calibration Sample

Figure 4.1 shows a schematic of the calibration sample's design. Briefly, it consists on a stair-like SiO_2 nanostructure which introduces discrete nanometer-sized distances between a fluorescent dye and a graphene surface. The base substrate is a transparent ($18\ \text{mm} \times 18\ \text{mm} \times 170\ \mu\text{m}^2$) glass coverslip.

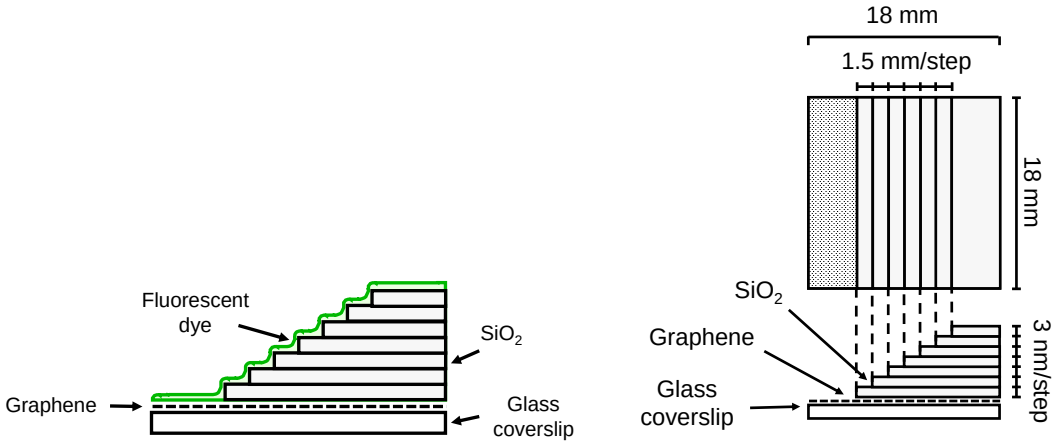

(a) (b)

Figure 4.1: Schematic of the calibration sample's design. (a) SiO_2 spacer steps introduce well defined nanometer nanometer sized distances between a fluorescent dye (fluorescein) and graphene. (b) Schematic with the dimensions of the sample.

(a) (b) (c)

Figure 4.2: Graphene transfer results. (a) Graphene sheet deposited around a Cu foil. (b) PMMA film deposited on top of graphene sheet. (c) Graphene on a PMMA film after the Cu foil dissolution in $FeCl_3$. (a), (b) and (c) correspond to the steps shown in Figures 3.3(a), 3.3(c) and 3.3(d), respectively.

4.1.1.1 Transfer of Graphene from a Cu Substrate onto Glass Coverslip

The first step for the preparation of this calibration-sample was the transfer of graphene from a Cu foil to a glass substrate. Figure 4.2 shows photographs of the transfer process. In particular 4.2(a), 4.2(b) and 4.2(c) show the initial graphene deposited on both faces of a Cu foil, the PMMA film deposited on the graphene face after plasma-ashing and the graphene on PMMA after the Cu foil dissolution in $FeCl_3$.

For the case of CVD-grown graphene transferred to glass, the two main points of interest are the graphene monolayer character and its surface coverage on the sample. Figure 4.3 shows a dark-field optical microscopy image of a graphene sample. The optical dark-field microscopy is typically used for enhancing the contrast of transparent or non-colored samples. In its images, void areas appear as dark areas and non-void as bright areas, thus opposite to normal optical bright-field microscopy images [71]. It has been experimentally shown that CVD-grown graphene patches scatter light in such way that

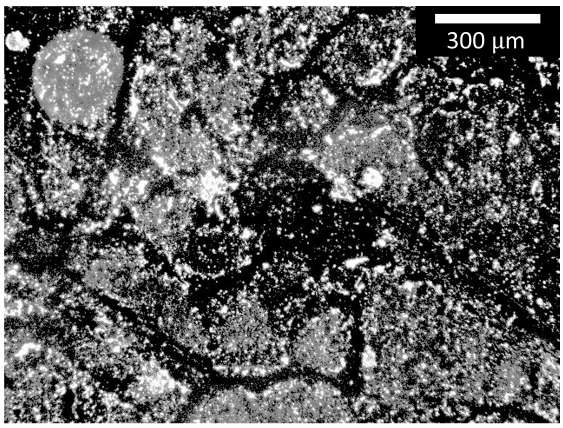

Figure 4.3: Dark-field optical microscopy image of graphene sample. The enhanced contrast of the dark field mode allows the qualitative analysis of the graphene surface coverage.

their shape can be identified by simple dark-field optical microscopy imaging [72].

The enhanced contrast of the dark-field reveals the edges of the graphene flakes [72] showing a non-continuous surface coverage with the formation of flakes with great dispersion in size and shape.

Figure 4.4(a), shows two Raman spectroscopy measurement. In the red line, the D peak is found to be of relatively low intensity, demonstrating a small number of significant defects in the graphene. Furthermore, the 2D peak shows a sharp single-peak shape, with roughly twice the intensity of the G peak, which indicates the presence of monolayer graphene. The blue line in Figure 4.4(a) also shows a single-peak Lorentzian shape in the 2D peak, which indicates monolayer graphene (see Figure 2.11(c). However, its much higher D peak and the intensity ratio $I_{2D}/I_G \approx 1/2$ reveal a much higher number of defects. The red and blue lines can therefore be regarded as monolayer graphene with a low and high number of defects, respectively. Figure 4.4(b) shows a confocal Raman spectroscopy map where the color of each pixel encodes the correlation with either of the spectra shown in Figure 4.4(a) which reveals that inside a graphene flake, nearly 99% of the area is covered by non-defect monolayer graphene.

It is worth mentioning that this work counted with the use of several graphene sample with roughly the same monolayer character, but rather different surface coverage. Particularly, the lifetime-distance calibration sample and most of the DNA-biosensor samples were prepared using a first batch of graphene that showed the formation of relatively small flakes whole the second graphene batch used for the final DNA-biosensor samples showed a nearly continuous surface coverage.

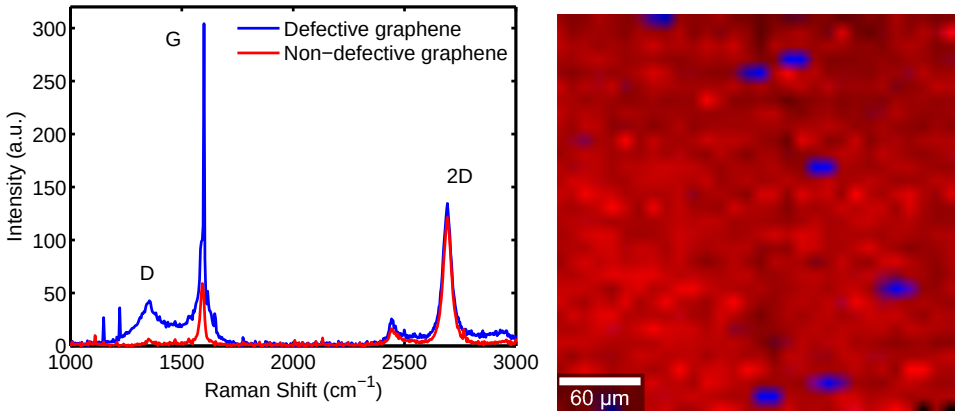

(a) (b)

Figure 4.4: Raman spectroscopy analysis of graphene sample. (a) Comparison between non-defect and defect graphene Raman spectra. For the red line, the relatively small intensity of the D peak and the ration $I_{2D}/I_G \approx 2$ indicate a small number of significant defects and the presence of monolayer graphene, respectively. (b) 300×300 μm Raman map of graphene sample. The red and blue areas in encode the spectral correlation with the spectra in (a).

4.1.1.2 Nanofabrication of Stairlike SiO_2 Layers

Section 3.2.1 describes how PECVD was used for the deposition of seven SiO_2 steps, to be used as spacers between a fluorescent film and a graphene substrate in the nanofabricated fluorescence lifetime-distance calibration sample. Figure 4.5(a) shows the designed method of the SiO_2 depositions and a photograph of the experimental implementation.

The depositions were performed assuming a constant SiO_2 deposition rate over the several layers. However, in order to obtain an accurate calibration curve, the spacer thicknesses were measured using spectral reflectance optical profilometry.

This technique is typically used to measure the thickness of thin films deposited on reflective substrates by comparing their spectral reflection with those of the empty substrates [73]. Because the glass coverslip substrate is not reflective, the thickness of the depositions was measured on an auxiliary Si wafer with a pre-deposited 100 nm SiO_2 later[1] - Figure 4.5(b) - and the results indicate a successful deposition of a stair-like nanostructure, with remarkable resemblance to the projected outcome in spite of the extremely simple deposition method.

The mean and standard deviation of the thickness corresponding to each step are shown in Table 4.1. The mean difference from step to step is (2.5 ± 0.4) nm, revealing that in average each step is shorter the expected 3 nm per step (Section 3.2.1). As a consequence, the distance resolution in the lifetime-distance calibration curve is slightly increased, but the full distance range is shortened from 21 nm to 17.4 nm.

[1] The initial 100 nm SiO_2 layer was used exclusively for enhanced profilometer accuracy purposes and can henceforth be ignored.

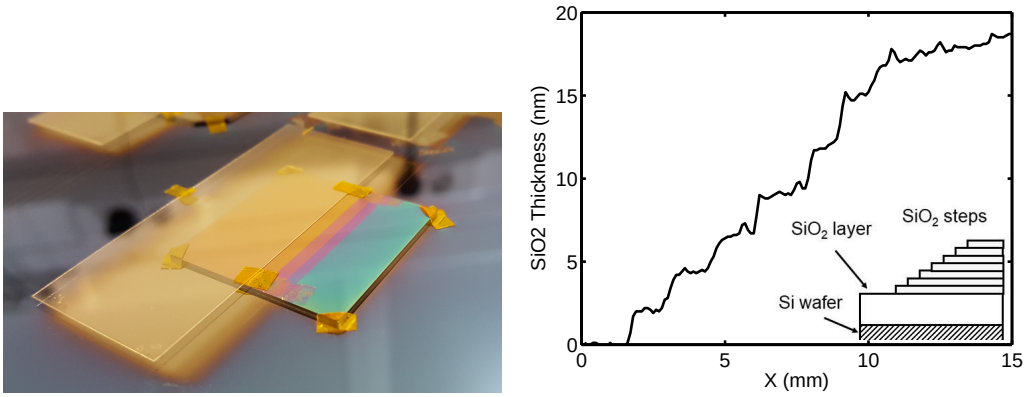

(a) (b)

Figure 4.5: Successive SiO_2 depositions to form discrete spacing between graphene and fluorophores. A moving shutter partially blocks the SiO_2 deposition, allowing the steps to form. (a) Photograph of shutter implementation. (b) Optical interferometer measurement of SiO_2 thickness profile. In this plot, the zero has been set at the top of a 100 nm thick SiO_2 layer on a Si wafer, which were deposited merely for enhanced interferometer accuracy purposes

Table 4.1: Mean and standard deviation of the thickness (h) of each step in the interferometer results of Figure 4.5(b).

Step #	0	1	2	3	4	5	6	7
$\bar{h}$ (nm)	0.0	2.2	4.4	6.9	9.2	12.0	15.0	17.4
$\sigma(h)$ (nm)	0.1	0.2	0.1	0.4	0.3	0.2	0.3	0.2

4.1.1.3 Functionalization of the SiO_2 Step Sample with a Fluorescein-Doped Polymer Layer

After the deposition of the SiO_2 spacers on top of a graphene substrate, an aqueous solution of PVA and fluorescein was deposited using spin-coating (experimental details in Section 3.2.1.3). The thickness of the resulting fluorescent film was measured using ellipsometry in an auxiliary Si wafer. For the sake of completeness, the ellipsometry results are plotted in Figure 4.6(a)), however there is no direct interpretation from curves. Instead, the film thickness is extracted from the model used for fitting the results (plotted in black dots).

Two measurements were performed: **Blank (reference) Si wafer**: the native oxide thickness was calculated to be approximately 3.58 nm. **Si wafer with spin-coated PVA film**: using a generic polymer model (Figure 4.6(b)), the thickness of PVA film was calculated to be 2.04 nm.

It is worth mentioning that, according to the results shown in Table 4.1, the fluorescent film is roughly of the size of one SiO_2 step. This means that in spite of being remarkably thin, it is likely to insert an additional error in the lifetime-distance calibration curve. Henceforth in this report, fluorophore-graphene distances will be considered

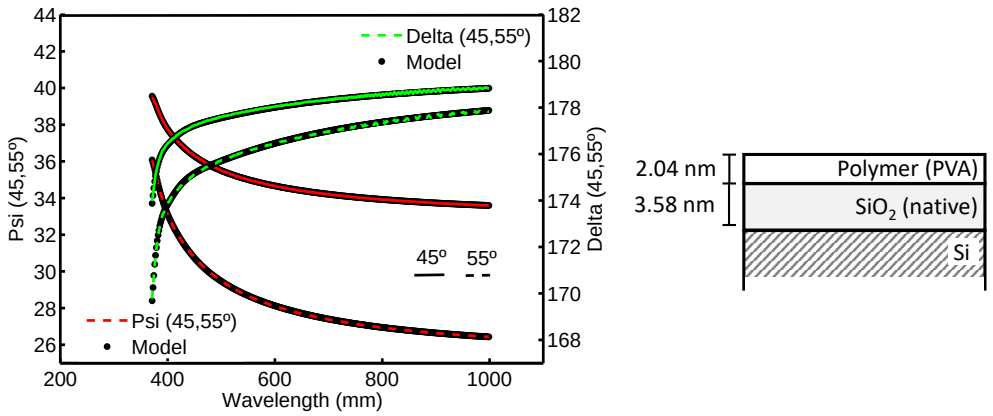

(a) (b)

Figure 4.6: Ellipsometry results. The thickness of the PVA layer has been derived from the model used to fit the ellipsometry measurements. (a) Measurement results (full lines) and fitting models (dots). (b) Structure of the model used for fitting the results of (a).

with a positive offset of 1 nm to the results of Table 4.1, which compensates for this error by assuming that the fluorescence intensity originates at half of the height of the fluorescent film.

4.1.1.4 Discussion of Nanofabrication and Characterization Limitations

The results presented thus far in this section rely on several assumptions. First of all, it is highly unusual to deposit dielectric materials like SiO_2 on top of graphene - usually only the reverse is done - which is why it is difficult to find reports regarding the deposition rate of SiO_2 on graphene. Here, it is being assumed that for such short thicknesses as those of Table 4.1, the deposition rate of SiO_2 on graphene is similar to that of SiO_2 on SiO_2.

Secondly, the spectral reflectance optical profilometer used to obtain the results Figure 4.5(b) is calibrated for the measurement of thicknesses ranging from tens or hundreds of nanometers to several microns. Here, the results show measurements lying up to 2 orders of magnitude below these values, which might lead to inaccurate measurements.

Finally, the PECVD has an uncertainty of around 2 nm for depositions of SiO_2 in Si substrates.

In sum, the depositions produced thicknesses that are of the same order of magnitude as the error of the equipment, on top of an unusual substrate, with an unknown deposition rate. As a consequence, the thickness distribution of the nanofabricated SiO_2 structure may not fully match the results shown in Figure 4.5(b).

4.1.2 FLIM Analysis of Fluorescein-coated Graphene Flakes

This section shows the results for the distance-dependent interaction of graphene with fluorescein. It starts by describing the FLIM system alignment and resolution in Section 4.1.2.1, then the fluorescence quenching and fluorescence lifetime reduction of fluorescein in the proximity of graphene in Section 4.1.2.2, the quantification of the nanoscale distance effect in the fluorescence lifetime in Section 4.1.3 and finally, the derivation of a semi-empirical model in Section 4.1.4.

4.1.2.1 FLIM Alignment and Lateral Resolution

The custom-built FLIM setup used for the fluorescence lifetime characterization is described in Section 3.1.2. The alignment of the system consisted on the manual adjustment of the position of the detector relative to the objective with micrometer screws (detection alignment), and the angles of the mirrors (omitted in Figure 3.2 for simplicity) that guide the laser beam from the source to the microscope objective inside the integrated cage system (excitation alignment). Adjustable pinholes were used to collimate the laser beam during the alignment process.

The resolution of the system was optimized and tested by imaging of alignment beads with a diameter of 0.5 μm[2] and the results are shown in Section 4.1.2.1. Figure 4.7(a) shows the confocal fluorescence intensity image of an alignment microsphere (0.5 μm in diameter). When a misalignment preponderates over either the x or y direction, an elliptical or double-peaked shape appears. In this case, the circular shape indicates that the system is correctly aligned.

Figure 4.7(b) shows the intensity profile of the measurement in the x and y directions at the location of maximum intensity. The Full Width at Half Maximum (FWHM) of the curves were estimated to be 0.85 μm and 0.75 μm in the x and y directions, respectively showing an average deviation of 0.2 μm. The lateral resolution of the system is usually determined using microsphere with diameters below the diffraction limit (0.1 μm for instance), however in this case, such was not possible.

4.1.2.2 Observation of Fluorescence Quenching of Fluorescein by Graphene

This section introduces the interpretation of FLIM images of graphene samples and several data processing procedures that shall be used many times throughout this chapter for extracting (additional) relevant information from FLIM images. Fluorescence intensity and lifetime images are generated from the combination of multiple confocal TCSPC measurements. In each pixel, the fluorescence intensity is integral of a decay curve and the lifetime can be extracted by an exponential curve-fit (details in Section 4.3. Hence, the fluorescence intensity and lifetime images are formed displaying either one of the quantities in the form of a color scale in each of its pixels.

[2] TetraSpeck Fluorescent Microspheres Sampler kit

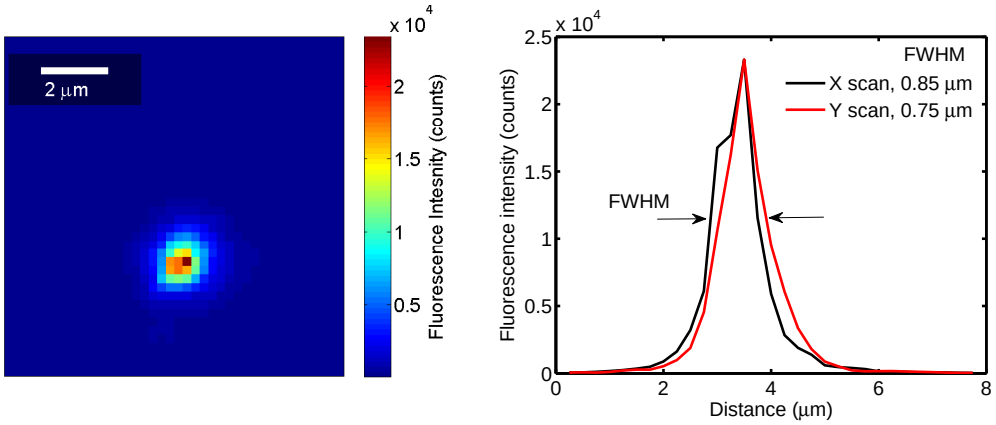

(a) (b)

Figure 4.7: Fluorescence intensity of alignment microsphere with 0.5 μm in diameter. The shape and diameter of the image was used to estimate the lateral error of the custom-built semi-confocal FLIM setup. The lateral resolution is usually obtained by imaging microspheres with diameters below the diffraction limit (0.1 μm for instance), however in this case this was not possible. (a) Fluorescence intensity image of the bead. (b) Intensity profile of the image at the location of maximum intensity.

Figure 4.8 shows fluorescence intensity images from two fluorescent-coated graphene samples with very different surface coverage. The physical interpretation of these images is explained in Section 4.1.2.2.

Figure 4.9 shows the fluorescence intensity (Figure 4.9(a)) and lifetime (Figure 4.9(b))

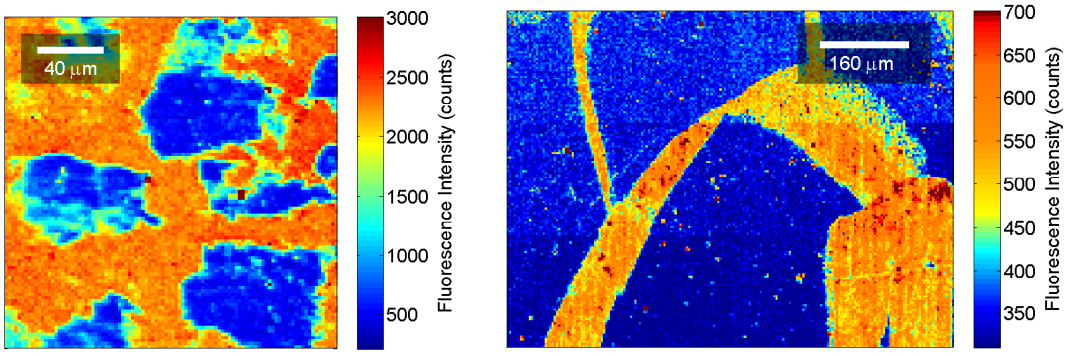

(a) (b)

Figure 4.8: Fluorescence intensity images of fluorescein deposited on graphene samples. Dark blue areas correspond to graphene flakes and orange areas correspond to the glass surroundings. (a) Single measurement of 200×200 μm^2 showing small graphene flakes . (b) A 600×800 μm^2 scan composed of twelve 200×200 μm^2 measurements appended together in a 3:4 matrix shows a much more homogeneous graphene surface coverage than that of (a).

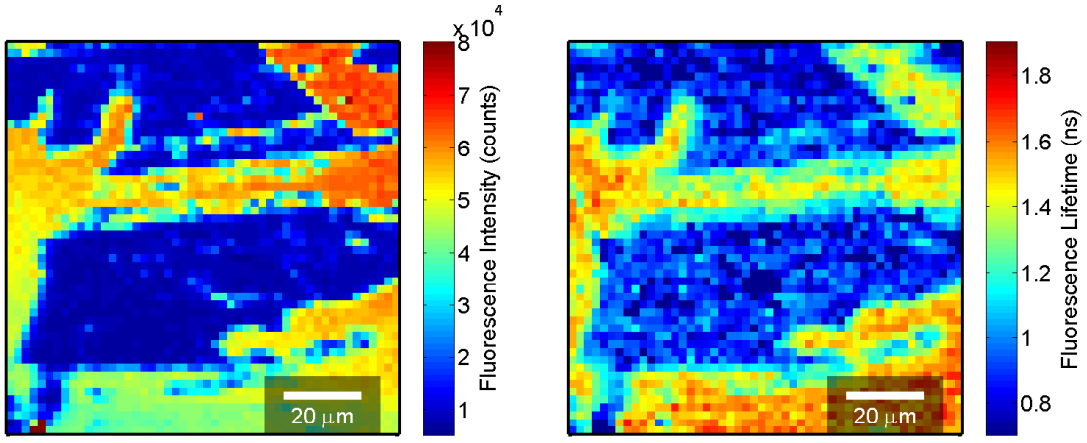

(a) (b)

Figure 4.9: Fluorescence images of fluorescein deposited on a graphene flake. (a) Fluorescence intensity image. (b) Fluorescence lifetime image. Both fluorescence intensity and lifetime of the Fluorescein layer are reduced upon the presence of a graphene patch.

of yet another graphene flake. Its physical interpretation is shown in Section 4.1.2.2

Discussion of the fluorescence intensity results

When fluorescent molecules are excited in the vicinity of graphene, part of their energy is transferred to the graphene surface through FRET, which would otherwise be released by emission of light. In the results of Section 4.1.1.1, it was shown that the CVD-grown graphene does not fully cover the entire sample as continuous sheet, but rather it forms flakes. Therefore, at the locations of the graphene flakes, the intensity is quenched to much lower intensities due to FRET, but not outside of the flakes, where the fluorescence assumes its full unquenched intensity. Around the edges of the flakes, the spatial distribution of graphene may be slightly more diffuse and the measured signal reflects the contribution of quenched and unquenched fluorophores. Thus, the dark-blue areas in Figures 4.8(a) and 4.8(b) correspond to graphene flakes, the orange areas to the glass surroundings and the cyan areas to the flake edges.

It is important to notice the difference in scale in Figures 4.8(a) and 4.8(b). Indeed, the large-area scan shown in Figure 4.8(b) is composed of twelve separate 200×200 μm^2 FLIM measurements appended together in a 3:4 matrix (the junctions of these images are actually visible). The area per patch in the two samples was estimated[3] to be 3700 μm^2/patch and 162800 μm^2/patch, respectively. This means that the graphene flakes in the sample of Figure 4.8(b) are over forty times larger than those of Figure 4.8(a). In fact, these samples were produced in two different batches, as the first one was not enough for all the samples prepared in this work.

[3]Considering 4 flakes in Figure 4.8(a) and 2 (incomplete) flakes in Figure 4.8(b)

The twelve figures of Figure 4.8(b) were measured under the exact same conditions, however they show a progressive loss in contrast from the bottom left to the top right corner. This is a good example of the major vulnerability of the fluorescence intensity to environmental conditions and focus.

Discussion of the FLIM results

A direct consequence of FRET is the reduction of lifetime. Indeed, the results shown in Figure 4.9(b) confirm that in the presence of graphene, not only the fluorescence intensity is quenched, but also the lifetime is substantially reduced.

The histogram of lifetimes (which will many times in this report be referred to as the *lifetime distribution*) of Figure 4.9(b) has been bar-plotted in Figure 4.10(a). The colored lines show a four-peak Gaussian curve fit of the lifetime distribution, according to

$$I_{Gauss} = \sum_{i}^{N} a_i \exp\left(-\frac{(\tau - \tau_i)^2}{c} \right) \quad , \quad c = \mathrm{FHWM}_i^2/(4\log(2)) \tag{4.1}$$

where N,a_i, τ_i and FWHM_i are the number of curves, their intensity, central lifetime and Full Width at Half Maximum of each curve, respectively. For the fit of Figure 4.10(a) $N = 4$ and, from shortest to longest τ_i are 0.52 ns, 0.90 ns, 1.28 ns and 1.51 ns.

In order to enhance the structural contrast of a FLIM image, it was calculated an image where all lifetimes were reduced to the central lifetime values τ_i and the interceptions of consecutive Gaussian peaks $\tau_{i,j}$ were used as boundaries. More specifically, the reduced lifetime τ_r of a given pixel is given by

$$\tau_r = \begin{cases} \tau_1 & \text{if } 0 < \tau < \tau_{1,2} \\ \tau_2 & \text{if } \tau_{1,2} < \tau < \tau_{2,3} \\ \vdots & \vdots \\ \tau_{N-1} & \text{if } \tau_{N-2,N-1} < \tau < \tau_{N-1,N} \\ \tau_N & \text{if } \tau_{N-1,N} < \tau \end{cases} \tag{4.2}$$

The result of applying this operation to Figure 4.9(b) is shown in Figure 4.10(b). In simple words, it shows what the FLIM image would look like if only those discrete lifetimes were present. Henceforth in this report, this shall be referred to as the *reduced lifetime image*. A comparison between the FLIM image of Figure 4.9(b) and its respective reduced lifetime image in Figure 4.10(b) again emphasizes the existence of three main components: quenched, non-quenched and intermediate fluorophores located inside, outside and at the edges of the graphene patches, respectively.

The fluorescence lifetime distribution and reduced fluorescence lifetime distribution image highlights the structures in FLIM images, and smooths out irrelevant artifacts.

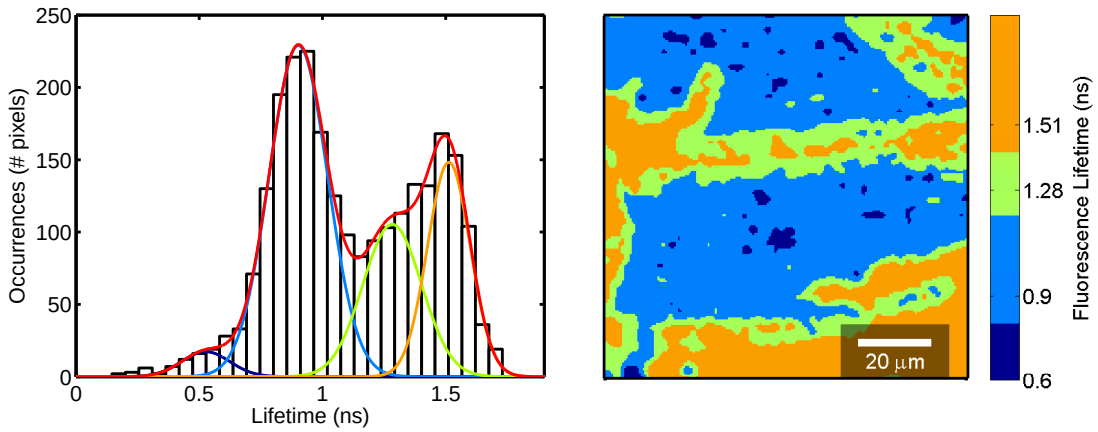

(a) (b)

Figure 4.10: Fluorescence lifetime distribution of the FLIM image from Figure 4.9(b). (a) Lifetime histogram with a four-peak Gaussian-curve fit. (b) Reduced lifetime distribution image, where the lifetimes in the FLIM image of Figure 4.9(b) were *reduced* to the central values of the Gaussian peaks in (a). The enhanced structural contrast of this operation highlights three main components corresponding to the inside (blue), outside (orange) and the edges (green) of a graphene flake.

4.1.3 Quantification of the Nanoscale Distance Effect

This sections presents the results of the FLIM measurements taken at each of the SiO_2 spacers of the lifetime-calibration sample. Each image comprised and area of $50 \times 50\ \mu m^2$ and they are shown in Figure 4.11 - the distances shown in the insets are in accordance to Section 4.1.1.3. The results reveal a pronounced increase in lifetime with distance which demonstrates the sensitivity of this method to nanoscale distance changes.

Similarly to the image processing of Section 4.1.2.2 the lifetime distribution of each image was calculated and plotted in Figure 4.12 as function of the SiO_2 thickness. The red dots plotted on top of the box show the mode of each lifetime distribution and they were taken as the characteristic lifetime of each measurement. These have been plotted function of distance in Figure 4.13(a).

In accordance to the overall tendency of the FLIM images of Figure 4.11, the results of Figure 4.13(a) show a strong dependence with distance, however with an apparent discontinuity between the 7.9 nm and the 10.2 nm measurements. Figure 4.13 shows the comparison of the experimental results with the theoretical model presented in Section 2.1.4.2 (Equation 2.24). There is partial agreement with the model, however, the lifetime does not tend to 0 ns at 0 nm. Interestingly, the measurements for thicknesses equal or larger than 10.2 nm seem to be in better agreement with the model.

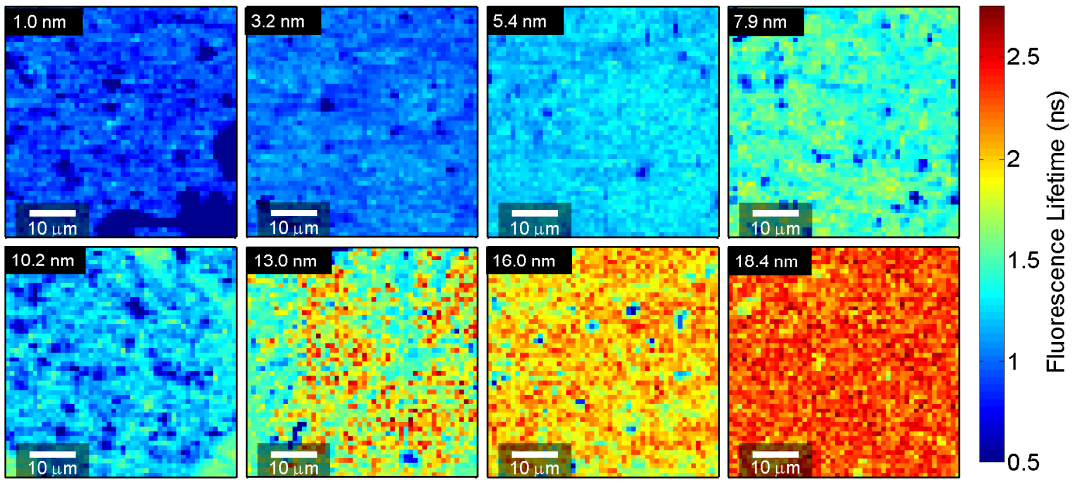

Figure 4.11: FLIM images of each spacer step of the nanofabricated calibration sample. The top-left insets on the images indicate the SiO_2 spacer thicknesses. As a consequence of the near-field RET interaction of fluorescein with the graphene, the fluorescence lifetime is highly dependent on the nanoscale distance, showing a remarkable reduction for shorter distances.

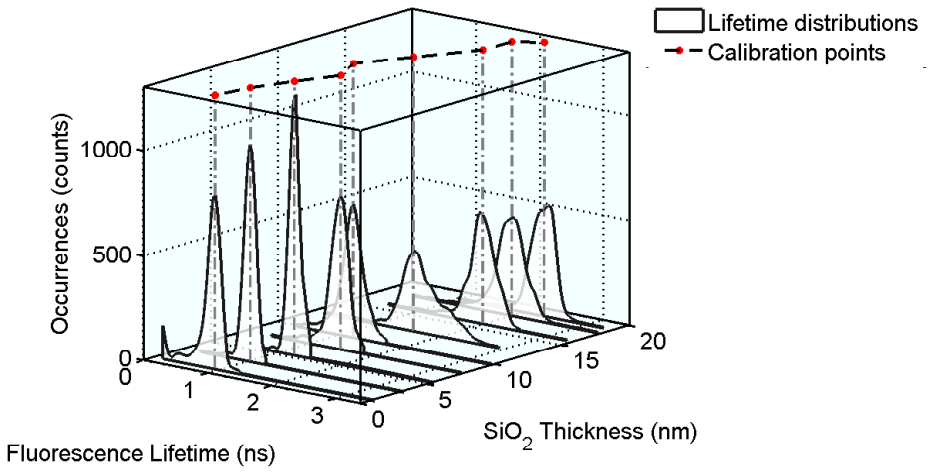

Figure 4.12: 3D *waterfall* representation of fluorescence lifetime distributions as function of SiO_2 thickness. The red dots at the top of the box indicate the modes of each distribution. These shall be the values used for the determination of an experimental fluorescence lifetime-distance calibration curve.

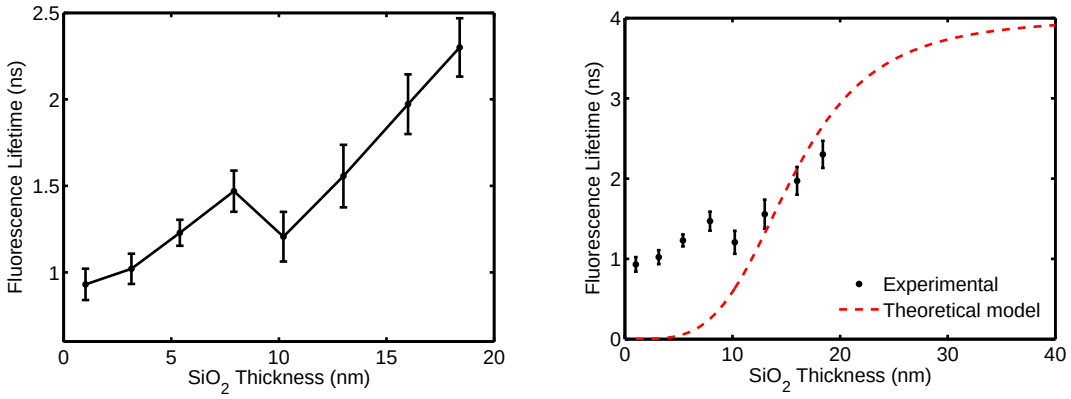

(a) (b)

Figure 4.13: Fluorescence lifetime-distance calibration curve. (a) Characteristic lifetimes of each of the FLIM images of Figure 4.11 obtained by calculating the mode of their lifetime distributions (Figure 4.12). The fluorescence lifetime shows a clear dependence with the distance, however there seems to be a discontinuity for SiO_2 thicknesses between 7.9 nm and 10.2 nm. (b) Comparison between the results of (a) and the theoretical model derived in Section 2.1.4.2 (Equation 2.24). The fluorescence lifetimes for SiO_2 thickness above or equal to 10.2 nm appear to be in better agreement with theory than those for SiO_2 thickness below 10.2 nm.

4.1.3.1 Discussion of the results

There are two major sources of errors in the results - experimental errors and analysis errors. Section 4.1.1.4 presented several sources of errors on the calibration sample nanofabrication process, which shall not be repeated here. The ellipsometry results shown in Section 4.1.1.3 estimates a thickness of 2 nm of the fluorescent film, which is why the distances were considered to have a 1 nm offset relative to the SiO_2 thicknesses of Section 4.1.1.2. However, this measurement was obtained in a single point of a flat auxiliary Si sample, where an homogeneous distribution was assumed. There is thus no concrete way of guaranteeing that a 2 nm PVA film is homogeneously spread over the entire area of the fabricated calibration sample, whose topography is much more complex than the one measured with ellipsometry.

A direct consequence of a thicker fluorescent film is that many fluorophores within the excitation volume of the laser may contribute to the fluorescence signal, which may have different FRET efficiencies, and therefore different lifetimes. Longer lifetimes usually yield higher fluorescence intensities which may mask the shorter lifetime signals. This could explain why the lifetimes of the shorter SiO_2 spacers do not converge to zero (See schematic of Figure 4.14).

Nanofabrication-wise, particularly in the nanoscale SiO_2 depositions, the thinner the layer, the more sensitive it is to experimental errors. In that sense, it is possible that the spacers with thickness from 1 nm to 7.9 nm might have been more affected by

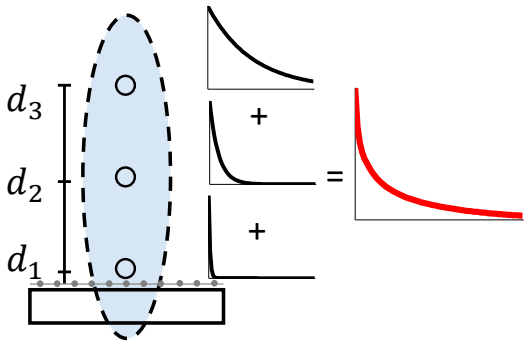

Figure 4.14: Derived model of a thick fluorescent film, where multiple fluorophores within the excitation volume of the laser are contributing to the fluorescence signal. Even if $d_1 = 0$ nm, the average lifetime of the contribution of the three fluorophores is larger than zero. The non-zero thickness of the fluorescent film is therefore masking the shorter lifetime contribution.

experimental parameters than the others.

On the data-analysis side, the lifetime determination on its own is not trivial. Furthermore, the results shown in this chapter were obtained by deconvolving the IRF from the TCSPC data. This is in principle a good option, but it may also cause errors. Further considerations about the lifetime determination are presented in Section 4.3. Nevertheless, Figure 4.15(a) compares the results of IRF deconvolution (black dots) and reconvolution[4] and the theoretical model. The IRF deconvolution results diverge even more from theory, as they do not account for the characteristic signature of the particular experimental setup used for the measurements.

4.1.4 Derivation of a Semi-Empirical Model

This section takes into consideration the statements of Section 4.1.3.1 to derive a semi-empirical model, based on the equations presented in Section 2.1.4.2, but modifying some parameters in order to have a better fit with the results obtained.

An independent measurement of a fluorescein sample revealed, using IRF deconvolution a free-space lifetime of 2.8 ns, which is very different from the 4 ns that can be found in literature for fluorescein in water at pH = 7 and ambient temperatures [74]. Such short value can be the consequence of a fitting error in the data analysis, or due to a chemical quenching of the fluorescein's lifetime in the PVA film.

According to Section 2.1.4.2, the theoretical model plotted in Figures 4.13 and 4.15(a) is given by

$$\tau(\tau_0, \epsilon) = \tau_0 \frac{r^4}{r^4 + R_{0G}(\epsilon)} \tag{4.3}$$

[4]The IRF reconvolution results shown in Figure 4.15(a) were obtained in exactly same way but using a different fitting algorithm for the lifetime calculations.

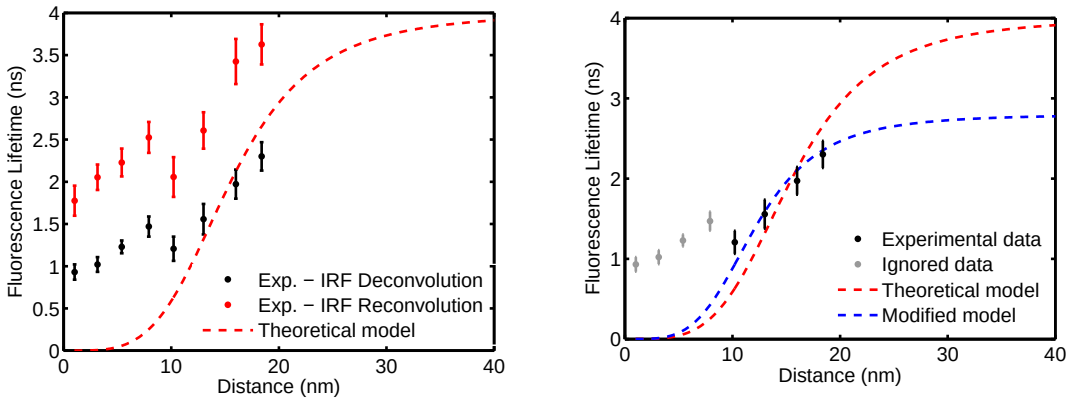

(a) (b)

Figure 4.15: Fluorescence lifetime-distance results calculated using IRF deconvolution and reconvolution algorithms. (a) Comparison with the theoretical model presented in Section 2.1.4.2 (Equation 2.24). The IRF reconvolution results show a similar slope for SiO_2 thicknesses above 10.2 nm, but an overall larger error than the IRF deconvolution. (b) Derived semi-empirical model. The blue dashed line was obtained by ignoring the measurements below 10.2 nm and modifying the model presented in Section 2.1.4.2, using a free-space lifetime $\tau_0 = 2.8ns$ and inserting an experimental coefficient in the dielectric function $A\epsilon$, where $A = 1.92$.

where τ_0, ϵ, r and λ are the lifetime of the fluorophores in free-solution, the dielectric constant of the medium, the distance to graphene and the emission wavelength respectively, and R_{0G} is the Förster distance of graphene, which is given by

$$R_{0G}(\epsilon) = \frac{9\kappa^2\alpha\lambda^4}{256\pi^3(\epsilon+1)^2} \tag{4.4}$$

where κ and α are the geometric factor and the fine-structure constant. The calculations for λ and ϵ are shown in Appendix A.1 to result in 534.0 nm and 2.19, respectively.

Assuming that there was indeed an experimental error in the nanofabrication of the first four SiO_2 depositions, then their lifetimes can either be ignored, or pictured with an offset such that they tends to zero for distances close to zero. Then, by fixing the free-space lifetime τ_0 to the measured 2.8 ns, the dielectric constant ϵ can be replaced by $A\epsilon$, where A is an experimental parameter that can be used as fitting parameter to adjust the remaining experimental points.

$$R_{Emp} = \frac{9\kappa^2\alpha\lambda^4}{256\pi^3(A\epsilon+1)^2} \tag{4.5}$$

In this case, $\tau_0 = 2.8$ ns and $A = 1.92$, and the result is plotted in the blue of Figure 4.15(b).

4.2 Study of DNA-Beacon Functionalized Graphene Interacting with Complementary DNA

In this work it is proposed a fluorescence lifetime-based hairpin molecular DNA-beacon biosensor. Section 4.1.3 demonstrated how the fluorescence lifetime of fluorophores can be modified at nanoscale distances from graphene. This effect is used to study conformational changes in graphene functionalized with DNA-beacons upon hybridization with complementary DNA, which is used for fluorescence lifetime-based DNA biosensing.

The design of the biosensor is described in Section 4.2.1 and the initial and final states of the biosensor (before and after the addition of target DNA) are compared in Section 4.2.2. Section 4.2.3 then uses the semi-empirical method derived in Section 4.1.4 to obtain axially-resolved nanoscale images of the biosensor and experimentally determine the molecular length of the DNA strands. Finally, Section 4.2.4 presents a study of the kinetics of hybridization using time-lapse FLIM.

4.2.1 Design of a Nanoscale Sensitive DNA Biosensor

In this DNA molecular beacon biosensor, a graphene surface is functionalized with fluorescent-labeled self-complementary DNA strands (beacons). Due to their self complementarity, they assume a folded configuration if isolated (Figure 4.16(a)), but acquire a linear upright configuration (Figure 4.16(b)) if hybridized to complementary (target) DNA [37, 38]. In this design, the nanoscale increase in the distance from the fluorophore to the graphene causes an increase in the fluorescence lifetime that is indicative of the presence of complementary DNA. This fluorescently labeled DNA molecular beacon has been chosen, because the binding process with target DNA is directly linked to a translocation of the fluorescent label away from the graphene surface, a change on the nanometer scale that potentially can directly be observed via changes of its fluorescence lifetime.

Figure 4.17 shows the schematic for the linker molecule, the Atto 488 labeled DNA sequence used and the reaction between them. When the reactive succidimine ester reacts with the amino-labeled oligonucleotides of the DNA molecule, the NHS ester group is dropped as a subproduct of the reaction and the 5'-Amino-Modifier C6 binds in its place. The reaction promotes the attachment DNA molecule to the graphene surface, according to the three-dimensional representation of Figure 2.14(b).

The length of the linker molecule can therefore be approximated [75] by

$$r_{linker} \approx 3r(\mathrm{C}-\mathrm{C}) + 2r(\mathrm{C}-\mathrm{N}) + 6r(\mathrm{C}-\mathrm{C}) = 1.68 \text{ nm} \tag{4.6}$$

and the length of the DNA molecule [76]

$$r_{DNA} \approx 28r\Big(\text{Adjacent nucleobases}\Big) = 9.52 \text{ nm} \tag{4.7}$$

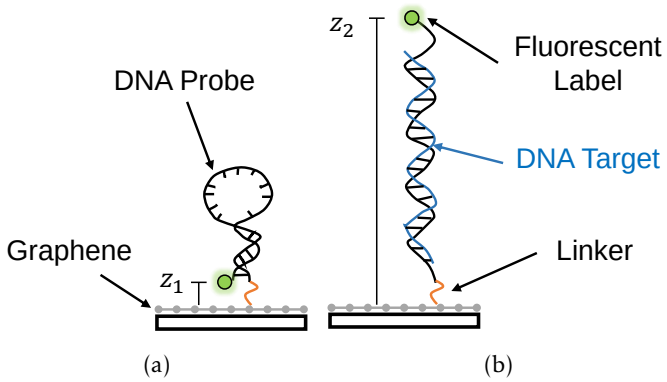

Figure 4.16: Design of a fluorescence lifetime-based DNA molecular beacon biosensor. A graphene substrate is functionalized with biosensor-probe self complementary DNA beacons (represented in black) which, upon hybridization with biosensor-target complementary DNA (represented in blue) changes from a folded (a) to an open (b) configuration. In this process, a fluorescent label is moved from extremely close to the graphene surface to a DNA strand-long distance from the graphene. The nanoscale increase in the distance to the graphene produces an increase in the fluorescence lifetime of the label which indicates the presence of target DNA

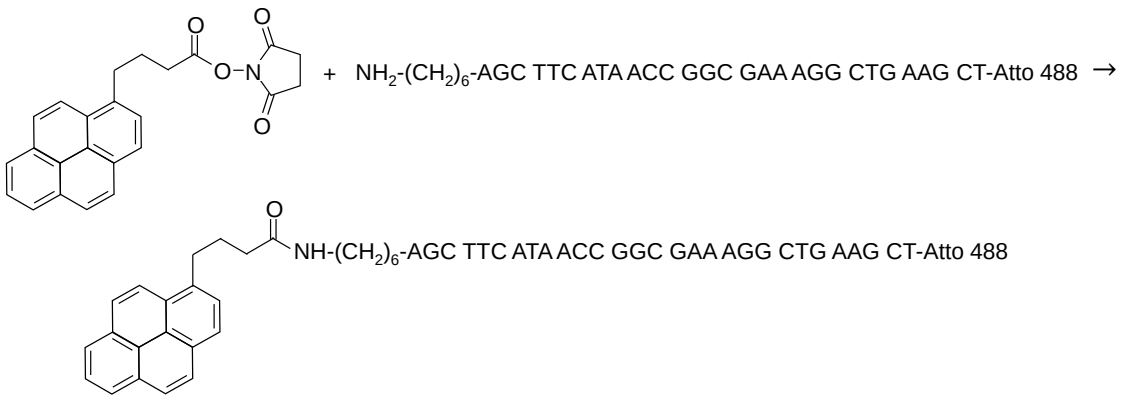

Figure 4.17: Conjugation of NHS-Ester modification to amino-labeled oligonucleotide. The DNA sequence corresponds to the fluorophore(Atto-488)-labeled DNA molecule used in the biosensing experiments.

therefore, the distance between the fluorophore and the graphene changes from 1.68 nm to 11.20 nm from the single-stranded folded configuration to the double-stranded hybridized configuration, upon hybridization.

The angle of inclination of the molecule in the hybridized state depends on what end of the molecule attaches to the graphene. The example shown in Figure 4.17 shows a fluorescent label at the 3' end of the DNA molecule, which in turn binds to the graphene at its 5' end (details about DNA directionality notation see ref. [77]). In such case, the molecule establishes a 90° angle with the surface of the substrate, as is depicted in Figure 4.16.

4.2.2 FLIM Characterization Before and After Reaction with Target DNA

The FLIM measurements of the initial and final states (before and after addition of target DNA) are shown in Figure 4.18. The FLIM image of the initial state before addition of target DNA, Figure 4.18(a) shows regions with longer lifetimes (larger than 1.7 ns), but most of the area is covered with shorter lifetimes. After the addition of target DNA, the FLIM image shows a large block with longer lifetimes, in particular, in regions that previously showed shorter lifetimes (Figure 4.18(b)). This remarkable increase in lifetime can be associated to the predicted fluorescence lifetime change during DNA hybridization of the molecular beacon with target DNA that will lead to a nanoscale increase in distance of the covalently linked Atto488 dye, which demonstrates the applicability of this technique for DNA-biosensing. In fact, at the areas where the most prominent lifetime difference occurred, there was an increase from 0.5 ns to 1.7 ns

4.2.2.1 Discussion of FLIM Structures

There are two major aspects in Figure 4.18 there are worth mentioning:

- The DNA-beacons should only bind to regions where there is graphene, otherwise, there is no linker molecule to which they can attach. As a consequence, at the initial state, all the fluorophores should be quenched by the graphene and the initial FLIM image should consist only on pixels with very short lifetimes, and pixels where there is no fluorescence intensity at all;

- A considerable number of pixels with short lifetimes in the initial state increased in lifetime upon the addition of DNA target solution, yet a large fraction didn't.

This is because short lifetimes in the initial state can either reveal the presence of graphene, or simple voids, where there are no DNA probes, and therefore no fluorophores. In the latter case, the measured signal is likely to correspond to the IRF, which virtually has a zero lifetime. Long lifetimes however should not appear in the initial state altogether. Their appearance can be related to a phenomenon of non-specific binding, where the DNA probes attach to the glass surface, inspite of the absence of linker molecules (Figure 4.19).

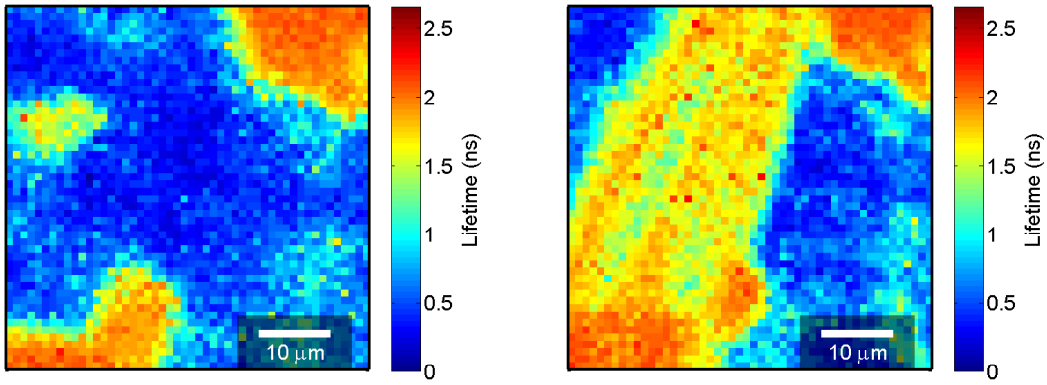

(a) (b)

Figure 4.18: FLIM images of the DNA-beacon biosensor sample before and after reaction with target DNA. (a) Initial state of the biosensor. Most of the area is covered with short fluorescence lifetimes which result from the strong RET between the atto-488 label fluorophores and the graphene. The longer lifetimes correspond to non-specifically bound beacons which resisted the surface passivation procedure. (b) Final state of the biosensor. Large fraction of the image shows a remarkable increase in fluorescence lifetime relative to (a) where beacons hybridized with target DNA. Short lifetime areas a likely to correspond to empty glass without any graphene or beacons.

Many attempts have been done during the experimental procedure to try to eliminate this effect by introducing additional rinsing steps in the sample preparation protocol. However, intensive rinsing also removed part of DNA-probes attached to graphene, which caused the fluorescence of the quenched areas to drop to prohibiting low intensities, whose TCSPC measurements could not be properly fitted.

Those areas that show a substantial increase in lifetime indicate the location of a graphene flake and shall henceforth be referred to as the *biosensor active areas*. Areas showing long lifetimes at the initial state shall henceforth be referred to as *non-specific binding areas*. Areas showing short lifetimes at both initial and final state shall henceforth be referred to as *void areas*.

4.2.2.2 Quantitative FLIM Analysis of the DNA-Hybridization

Figure 4.20(a) shows the lifetime distributions for the initial (black points) and final (red points) states of this biosensor and the respective multiple-peak Gaussian-curve fits (lines). These show a significant increase in the number of pixels with $\tau \in [1.3; 1.85]$ ns and decrease in $\tau \in [0.1; 0.9]$ ns. Furthermore, the number of pixels with $\tau > 1.85$ ns remained approximately constant.

Similarly to the analysis of Section 4.1.2.2 to obtain a *reduced lifetime distribution image*, the multiple-peak Gaussian curve-fits of Figure 4.20(a) were used to create the reduced lifetime distribution images of the initial and final states (not shown). Figure 4.20(b)

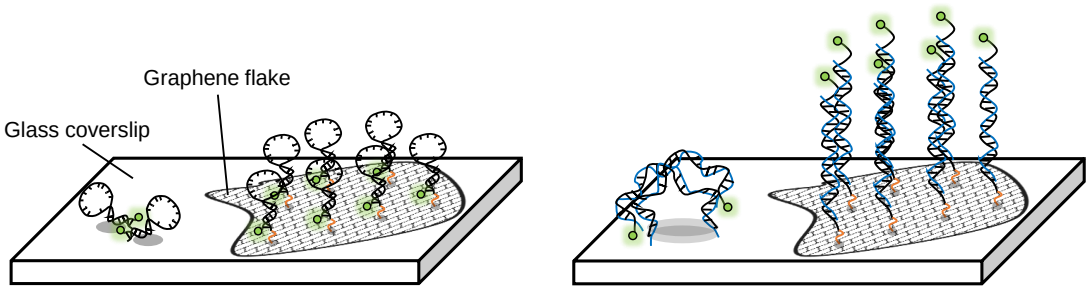

(a) (b)

Figure 4.19: Derived molecular model of the DNA-beacon unfolding process. (a) Initial state of the biosensor. Biosensor-probe DNA molecules are attached to graphene but also to glass by non-specific binding. The fluorescence lifetime of the fluorophore labeled beacons attached to graphene is reduced by RET, but remains unchanged for those on the glass surface. (b) Final state of the biosensor. Biosensor-target DNA molecules hybridized with all beacons, but only those attached to graphene display an increase in their fluorescence lifetime.

Table 4.2: Derived fluorescence lifetime-difference thresholds and respective designations, for the identification of structures in Figure 4.20(b). In areas outside of graphene were separated in *void areas*, where no DNA beacons attached and *non-specific binding areas* where DNA beacons attached to glass instead of graphene. In both cases the fluorescence lifetime remained nearly constant ($\delta\tau \approx 0$ ns) however their initial lifetimes τ_0 are different.

τ_0	$\Delta\tau$	Region Designation
< 1 ns	≈ 0 ns	*Void areas*
< 1 ns	1.2 ± 0.2 ns	*Biosensor active areas*
> 1.85 ns	≈ 0 ns	*Non specific binding areas*

shows the difference between these two reduced images. The bright-colored areas in the image show where the most relevant lifetime increase occurred and therefore highlight the biosensor active area. Lifetime-variation thresholds were used to isolate areas of interest in the image.

Figures 4.21(a) and 4.21(b) show areas with a variation of lifetime $\Delta\tau > 1$ ns, which correspond to the biosensor active areas. Additionally, Figure 4.21(c) shows the areas where $\Delta\tau < 0.05$ ns and $\tau_0 > 0.5$ ns, isolating the regions non-specific binding occurred. Although it is not clear why these structures appear they reveal what in principle corresponds to the fluorescence lifetime of the fluorophores in solution, at the particular chemical environment of the buffer solution used.

Based on the conditions used for obtaining the images of Figure 4.21, it is possible to define the three previously identified regions of interest, which are shown in Table 4.2.

Figure 4.22 shows the lifetime distributions of Figures 4.21(a), 4.21(b) and 4.21(c) in blue, green and red line, respectively, where the illustrations for the folded beacon,

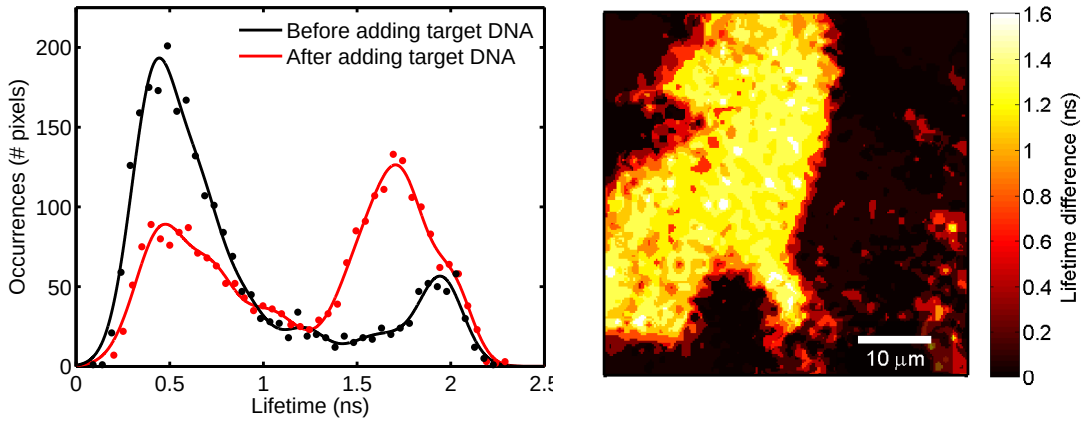

(a) (b)

Figure 4.20: Fluorescence lifetime distribution before and after reaction with biosensor target DNA. (a) Histograms of fluorescence lifetime at the initial (red) and final (black) states of the biosensor. Hybridization lead to the appearance of a distinct feature around $\tau \in [2.5; 3.7]$ ns, corresponding to the lifetime of the DNA beacons in the stretched configuration. (b) Difference between reduced fluorescence lifetime distribution images before and after hybridization. The reduced lifetime distribution images of Figures 4.18(a) and 4.18(b), were obtained analogously to the treatment in Section 4.1.2.2 and then subtracted. The resulting image highlights the areas in which there was a lifetime increase: the *biosensor active areas*.

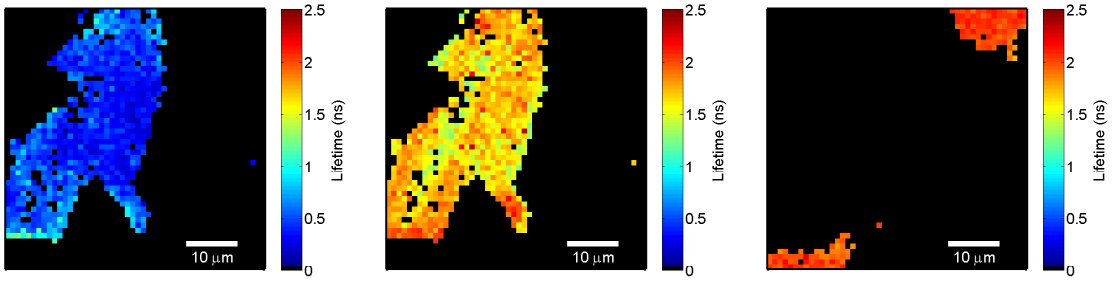

(a) (b) (c)

Figure 4.21: Identified areas of interest obtained by isolating areas from Figure 4.20(b) based on the conditions of Table 4.2. (a) Initial state of the biosensor active area. (b) Final state of the biosensor active area. The remarkable difference between (a) and (b) indicate the occurrence of DNA hybridization. (c) Non-quenched areas (outside of graphene patch). The DNA beacons attached to these locations did not interact and therefore their fluorescence lifetime remain constant.

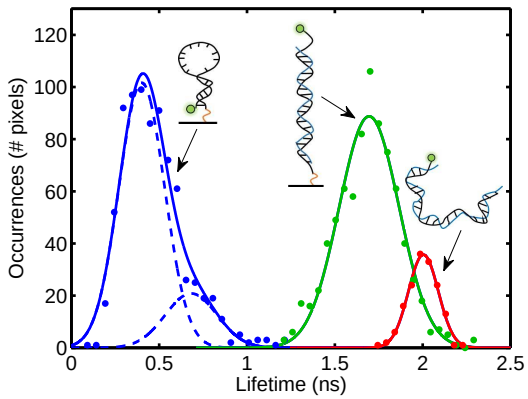

Figure 4.22: Lifetime distribution of isolated areas of interest from Figure 4.21(a) to 4.21(c) and respective Gaussian fits. The derived molecular illustrations of Figure 4.19 were used as legends. From short to longer lifetimes, the Gaussian peaks correspond to: (blue) Active area before addition of target DNA @(t=0 mins)(τ_c = 0.40, FWHM= 0.31) ns; (green) active area after addition of target DNA @(t=125 mins)(τ_c = 1.72, FWHM= 0.35) ns; (red) Non-specific binding @(t=0 mins)(τ_c = 2.00, FWHM= 0.20) ns. In the derived lifetime to distance model the change from 0.4 to 1.7 ns is associated with an ≈10 nm translocation of the fluorescent labels (from round 9 nm to 19 nm) away from the graphene surface.

hybridized beacon and non-specifically bound DNA have been used as legends, according to the interpretation of Table 4.2. Indeed, Figure 4.22 summarizes the three major states of interest for demonstrating the applicability of this technique to biosensing.

4.2.3 Obtaining Nanoscale Distances Information from FLIM

Using the semi-empirical formulation of Section 4.1.4 (Equations 4.3 and 4.5), the distance-fluorescence lifetime model (inverse of Equation 4.3) was defined by

$$r = \left(\frac{R_{Emp}}{\tau_0/\tau - 1} \right)^{\frac{1}{4}} \tag{4.8}$$

According to the results shown in Figure 4.22, for the chemical environment of the buffer solution used, $\tau_0 \approx 2.0$ ns. Then, using the experimental correction factor $A = 1.92$ determined in Section 4.1.4, the fluorophore-graphene distances for the folded state, hybridized state and non-specific binding were calculated[5] and displayed in Table 4.3.

In this case, the distances shown in table 4.3 for the folded and hybridized states correspond to the length of the PBSE linker and the length of the stretched DNA beacon, respectively. The expected values are 1.68 nm to 11.20 nm, however, the increase in distance from the initial to the final state is approximately 10 nm, which is in good agreement with the expected 9.52 nm, the extension of the fully stretched DNA strand.

[5]Using $\tau_0 = 2.0$ ns is of course a crude approximation, once the FLIM results actually show pixels with lifetimes larger than 2 ns. Nevertheless, it is a good enough for the estimation of the molecular lengths.

Table 4.3: Calculated fluorophore-graphene substrate distance, based on the semi-empirical model from Equation 4.8. The errors have been calculated using the standard deviations of the Gaussian peaks in Figure 4.22.

Designation	Calculated distance (nm)
Folded state	(9 ± 2)
Hybridized state	(19 ± 7)
Non-specific binding	∞

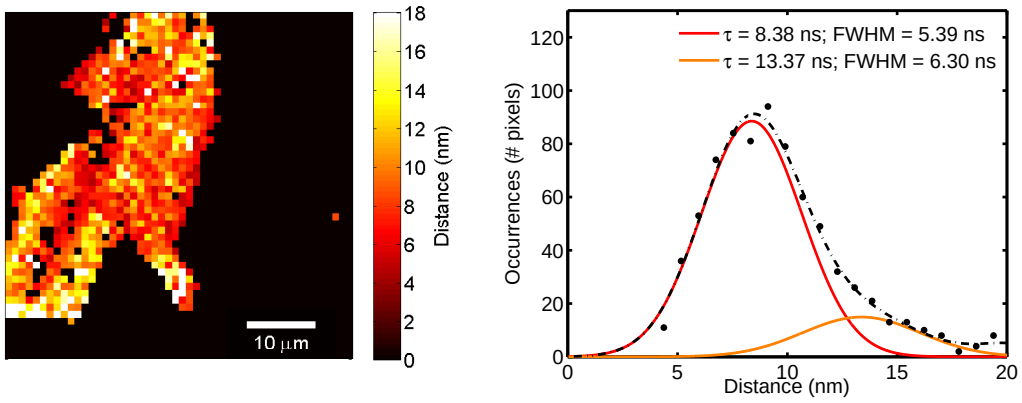

(a) (b)

Figure 4.23: Fluorophore distance to graphene. The distance was calculated by applying the semi-empirical model derived in Section 4.1.4 to the FLIM image of Figure 4.21(b) and subtracting the background level of 9.27 nm. (a) Spatial distribution of fluorophore distance to graphene. (b) Histogram of distance occurrences. The molecular length of the DNA sequence was estimated to be 8.4 ± 2.3 nm

Again, the results point to the existence of an error in lifetime determination algorithm which affects the exactness of the lifetime values, yet the relative results are very much in accordance with the expected behavior.

The semi-empirical model derived in Section 4.1.4 was also used to determine mapping of the fluorophore distance to graphene. Applying this model to the FLIM image of Figure 4.18(b) revealed a background level[6] of 9.37 nm, which was subtracted from the image to obtain the molecular length of the DNA strands. Figure 4.23 shows the resulting image and the histogram of distance occurrences which has been Gaussian curve-fitted. The center and standard deviation of the most prominent Gaussian contribution were used to estimate the molecular length of the DNA to be 8.4 ± 2.3 nm, which again is in agreement with the calculated 9.52 nm.

Figure 4.24 shows a derived three-dimensional model of the fluorophore distance to graphene before and after the addition of target DNA using the same approach as in Figure 4.23. The model has been spline-interpolated by a factor of 4 for a smoother

[6]The background level corresponds to the fluorophore distance to the graphene in the folded state which, in theory, should be zero.

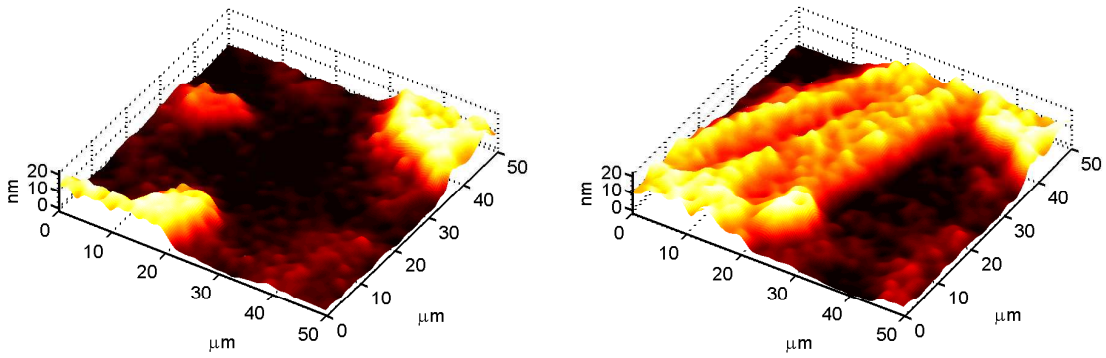

Figure 4.24: 3D representation of the biosensor before (a) and after (b) the addition of target DNA. A large fraction of the scanned area shows an increase of 8.4 ± 2.3 nm in the fluorophore distance to graphene after hybridization. Regions where non-specific binding occurred show distances tending to infinity (colored in white).

surface.

At the regions where non-specific binding occurred (bright-colored areas in Figure 4.24(a)) the distance tends to infinity. Elsewhere, the distance tends to zero and to 8.4 ± 2.3 nm before and after the addition of target DNA, respectively.

4.2.4 DNA Binding Kinetics Using Time-Lapse FLIM

The results presented in Sections 4.2.2 and 4.2.3 are representative of the initial and final state of the DNA biosensor, however important information can also be extracted from the characterization of its temporal behavior. A sequence of time-lapse FLIM images was measured with a collection time of 4 minutes and 45 seconds per image, from 10 to 252 minutes (52 images) after the beginning of the addition of target DNA. Figure 4.25 shows nine selected FLIM images which are representative of the fluorescence lifetime gradient over time.

The lifetime distribution histograms of each FLIM image plotted in Figure 4.26(a). A prominent shift on the modal value of the distributions was observed (Mo(t = 10 min) $\approx$ 0.54 ns $\rightarrow$ Mo(t = 10 min) $\approx$ 1.30ns), suggesting a continuous increase in the lifetime over time, rather than a binary transfer of abundance from the initial to the final lifetime.

Each histogram of the sequence was fitted with five Gaussian curves. The fitting parameters (peak position and FWHM) were obtained by iterative fittings of the initial and final measurements, until both could be properly fitted using the same parameters and only different amplitudes. Then, the whole sequence was fitted by using the results of each fit as the starting parameters for the next[7]. The identified positions for the Gaussian peaks can be regarded as the characteristic fluorescence lifetime components of the

[7]The peak positions for each fit were allowed to change up to 1% (below or above) their previous values for an enhanced fitting quality.

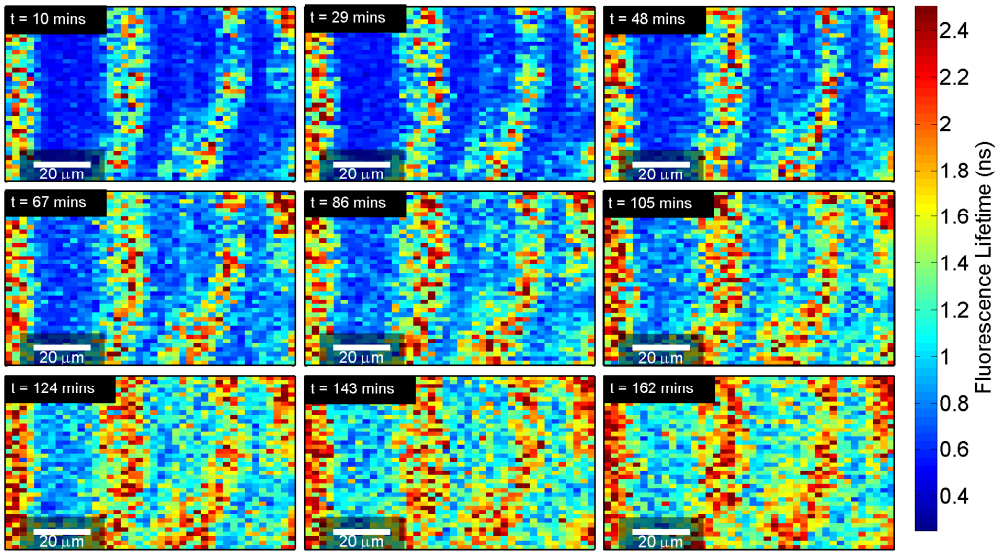

Figure 4.25: Time lapse FLIM images of the graphene-based DNA-Beacon biosensor after the addition of target DNA. A total of 52 images were acquired, with a collection time of 4 minutes and 45 seconds per image, showing the hybridization process from 10 to 252 minutes. The time points are given at the top-left corner of each image.

experiment, whose abundance was traced over time. These characteristic lifetime values have been converted to nanoscale distances using Equation 4.8 and the same approach as in Section 4.2.3. The results can be found in Table 4.4. The characteristic lifetime of 2 ns corresponds to the fluorescence lifetime of the fluorophores in free solution and therefore $r(\tau = \tau_0) \to \infty$. Three histograms of the sequence, associated with the initial, an intermediate and final time points of the sequence are shown along with the respective Gaussian curve-fits in Figure 4.26(b).

Using the area under the curve of each Gaussian component, the relative abundance of the characteristic lifetime has been calculated and plotted over time in Figure 4.27(a). The results show that the shortest lifetime component (dark blue) started as the most abundant and completely vanished after 150 minutes of reaction, while an intermediate component (cyan) increased and vanished with a lifespan of about 85 minutes and the longer components (green and orange) progressively increased over time. The longest lifetime component (red) matches the previously identified free-space lifetime of the fluorophore (Section 4.2.2.2) and also shows an increase in abundance over the reaction time.

In order to obtain a qualitative graphical representation of the reaction kinetics, the linear anti-correlation[8] between the histograms at a given time point and that of the first

[8]Here anti-correlation stands for $1 - r_{xy}$, where r_{xy} is the Pearson's correlation coefficient between the curves x and y. The results were obtained using the standard function `corr` in MATLAB.

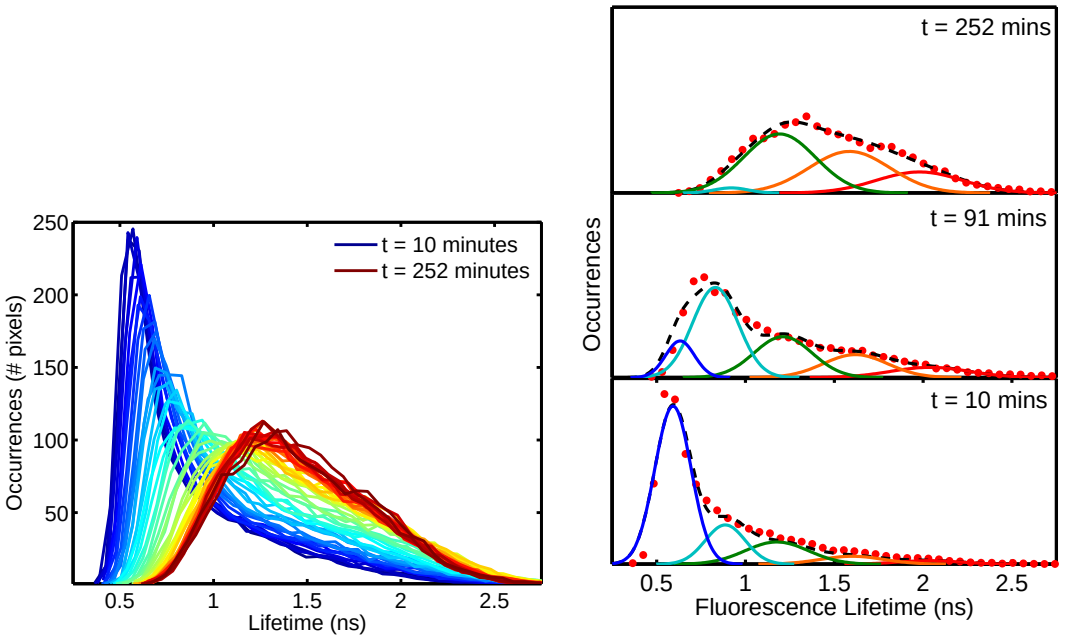

(a) (b)

Figure 4.26: Time-lapse fluorescence lifetime distributions of the DNA molecularr beacon biosensor during DNA hybridization. (a) Histograms of 52 FLIM measurements. The modal value of the distributions shifts continuously over time (Mo(t = 10 min) ≈ 0.54 ns → Mo(t = 10 min) ≈ 1.30ns) indicating a progressive increase in lifetime, rather than a binary transfer of abundance between the initial and final biosensor states. (b) Multiple-Gaussian fits to three lifetime distributions from (a), which are representative of the general evolution of the distribution and fit quality. Curve parameters: (dark blue) τ_0 = 0.60 ns, FWHM= 0.23 ns; (cyan) τ_0 = 0.92 ns; FWHM= 0.30 ns; (green) τ_0 = 1.19 ns; FWHM= 0.47 ns; (orange) τ_0 = 1.59 ns; FWHM= 0.54 ns; (red) τ_0 = 1.98 ns; FWHM= 0.56 ns.

measurement has been plotted over time in Figure 4.27(b). The time for the complete DNA hybridization has been estimated from the point of saturation of the smoothed (red) curve in Figure 4.27(b) to be 185 minutes for a temperature of 19° Celsius.

Table 4.4: Conversion of the identified characteristic fluorescence lifetime components of the hybridization reaction to nanoscale distances. The conversion of fluorescence lifetime to distance was performed analogously to the analysis presented in Section 4.2.3. The free-space lifetime was considered to be τ_0 = 2 ns, and therefore $r(\tau = \tau_0) \to \infty$, which stands for fluorophores in solution located outside the range of RET to the graphene.

Lifetime (ns)	0.6	0.9	1.2	1.6	2
Distance (nm)	<1	2	4	8	>8

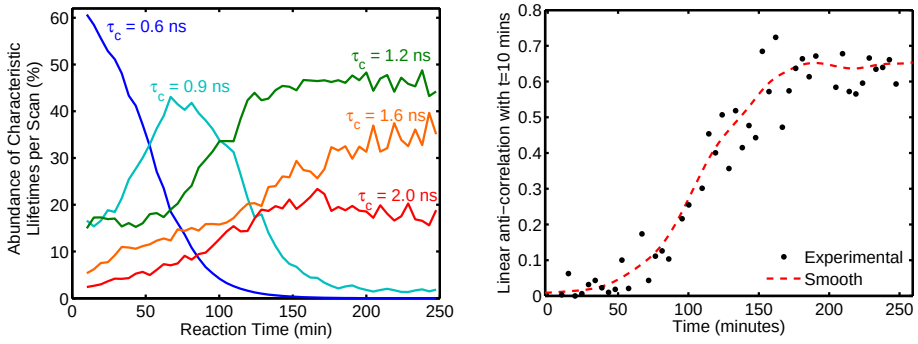

(a) (b)

Figure 4.27: (a) Time-dependent abundance of the identified characteristic fluorescence lifetimes per FLIM image. The most abundant component at the beginning of the reaction (dark blue - shorter lifetimes) completely vanished after about 150 minutes. An intermediate state (cyan - intermediate lifetimes) increased to a maximum and decreased afterwards, showing a lifespan of about 85 minutes. The final states (green and orange - longer lifetimes) show a prominent increase at the moment the intermediate state started to decrease. The longest lifetime component (red) shows free-space lifetime of the fluorophore ($\approx$ 2 ns). (b) Linear anti-correlation between the lifetime distribution at a given time point and initial state. From an applied perspective, the shape of this curve qualitatively indicates the kinetics of the reaction. It shows a sharp increase for reaction times between 85 and 160 minutes and a saturation point at 185 minutes (room temperature 19° Celsius).

4.2.4.1 Discussion of the Results

The results of Figure 4.27(a) show a very interesting complement to the interpretation devised in Section 4.2.2.2. In addition to the initial (folded) and final (stretched) hybridization states, they reveal the existence of intermediate (temporary) states, which are most likely due to incomplete hybridization configurations (see derived molecular model in Figure 4.28). The curves in Figure 4.27(a) can be interpreted as follows: dark-blue line corresponds to isolated DNA-beacons, the cyan to partially hybridized strands, the green and orange lines to the fully hybridized state and the red line to the non-interacting lifetime of the fluorophores in solution. Together with Figure 4.27(b), the results trace the movement of the fluorophores in their ascent from the substrate to DNA-top position.

Comparing the absolute fluorescence lifetime values to those of Figure 4.22 reveals a similar non-interacting lifetime (around 2 ns) but a slightly shorter lifetime for the final hybridization state. A possible explanation for this is that in the results of Section 4.2.2, the selected graphene patch displayed a very homogeneous surface (Figure 4.18), whereas for the kinetics analysis the sample was more irregular (Figure 4.25). The irregularities of the sample may lead to the existence graphene-patch edges, which interact with the fluorophores in a less expressive way (Section 4.2.2.2).

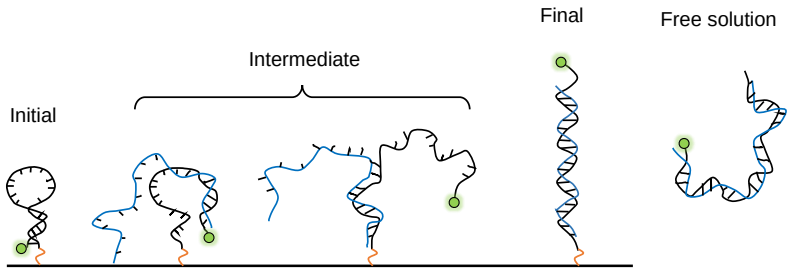

Figure 4.28: Derived molecular model of the DNA unfolding process during hybridization with the target DNA. The temporal analysis of the kinetics of hybridization revealed the existence of intermediate states, where the biosensor probe and target DNA are only partially bonded.

4.3 Comparison of Fluorescence Lifetime Determination Algorithms

One of the most crucial issues of this work was the determination of the fluorescence lifetime from a TCSPC decay curve. Particularly for the determination of very short lifetimes, choosing the fitting method becomes critical and an accurate analysis should take into consideration the Instrument Response Function (IRF), that is characteristic of the experimental setup.

This section presents several lifetime-determination approaches such as single and multiple-exponential curve-fitting approaches, multiple-exponential curve-fitting with IRF reconvolution and deconvolution approaches and an intensity-based approach developed in this work for the fast calculation of FLIM images.

4.3.1 Multi-Exponential Method

The simplest way of addressing a TCSPC decay curve is to use a single-exponential curve fitting. According to Section 2.1.2, this should be the case of an homogeneous sample emitting light with a single fluorescence lifetime τ. However, a TCSPC decay curve can comprise multiple lifetimes [78], in which case a multi-exponential curve-fit can be used.

$$I = \sum_{i}^{N} (a_i \exp(-t/\tau_i)) \tag{4.9}$$

where I is the measured intensity, N is the number of lifetimes, a_i are the weights of each lifetime τ_i.

In practice, and especially in complicated chemical environments like those at study in this work, very seldom can a TCSPC decay curve be properly fitted with a single exponential curve-fit. Figure 4.29 shows the same TCSPC measurement fitted with single, double and triple-exponential curve-fits in Figures 4.29(a), 4.29(b) and 4.29(c), respectively. The single-exponential curve-fit can hardly pass through the experimental points; the double-exponential curve-fit nearly perfectly fits the entire curve; and the triple-exponential curve-fit is also able to properly fit the experimental points. However, any n^{th} order exponential fit, with $n > 2$ will in principle provide a decently looking curve-fit, although it will most likely generate an over-fitting situation. In such case, the curve is likely to be fitting irrelevant background noise-originated features or simply inserting artifacts.

A major fault of these models is that they do not take into consideration the IRF, which accounts for the characteristic "signature" of the detection system.

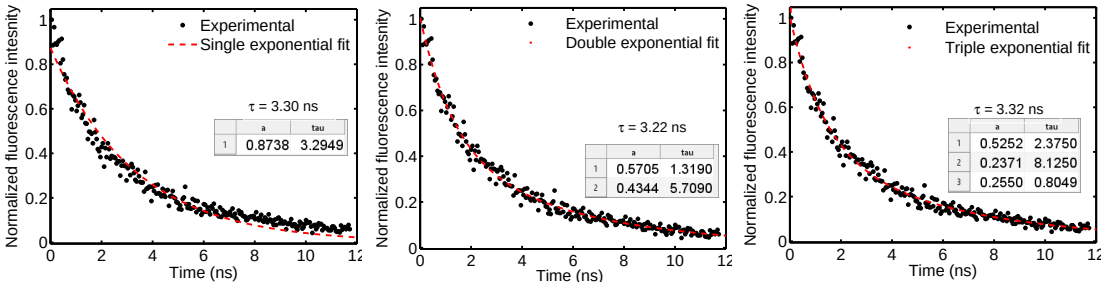

(a) (b) (c)

Figure 4.29: Fluorescence lifetime determination using exponential curve-fits. (a) Single-exponential fit. The resulting curve does not properly fit the experimental points. (b) Double-exponential fit. The resulting curve fits the experimental points nearly perfectly (c) triple-exponential fit. The third exponential is not necessary to fit the experimental points.

4.3.2 IRF Reconvolution and Deconvolution Methods

Figure 4.30 shows the measurement of the IRF. There are two approaches for compensating the IRF effects from the measurements: **Re**convolution: model an IRF and take its effect into consideration directly on the equation of fitting model; and **De**convolution: measure the IRF and deconvolve it from the data [79].

In principle, deconvolution algorithms are more descriptive of the experimental setup used for that particular measurement. However, the fittings are more noise-sensitive and more likely to produce artifacts, which may be difficult to distinguish from real effects. The functions in MATLAB for IRF deconvolution and reconvolution used in this work

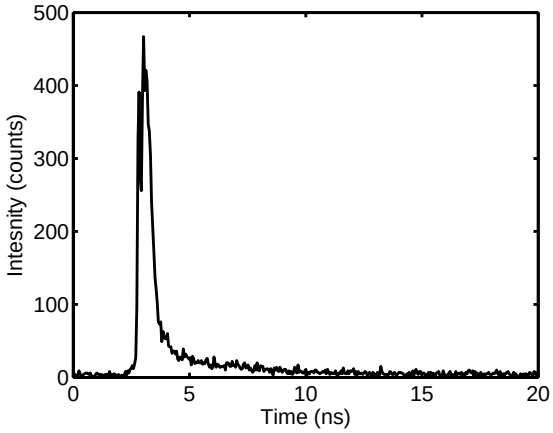

Figure 4.30: TCSPC measurement of the IRF. The instrument's response to an infinitely short light pulse as a consequence of the transit-time spread of the photoelectrons through the detector. The IRF can be taken as the signature of the particular custom-built setup used in the measurements and its effects should be compensated in the determination of the fluorescence lifetime.

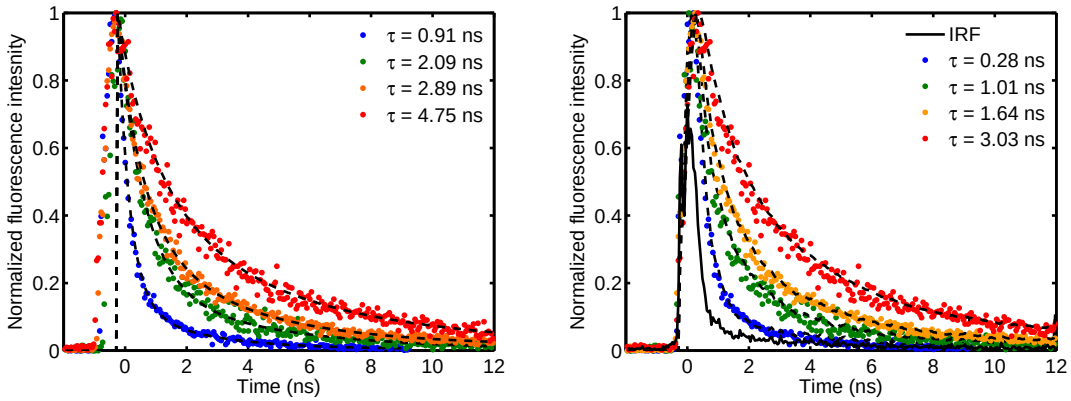

(a) (b)

Figure 4.31: Experimental decay curves (dots) and multi-exponential fits (dashed lines) for three different fluorescence lifetimes. (a) Using a modeled IRF reconvolution. (b) Using a measured IRF deconvolution. Fluorescence lifetimes calculated using IRF deconvolution are consistently lower than those for which IRF reconvolution was used.

were implemented using algorithms developed by Jörg Enderlein [80] (See Appendix A.2.1). Both algorithms automatically evaluate the suitable number of exponential components to use for the fit and reconvolve (deconvolve) the modeled (measured) IRF from the measurements.

Figure 4.31 shows the results of four TCSPC measurements and the respective lifetimes calculated with IRF reconvolution (Figure 4.31(a)) and deconvolution (Figure 4.31(b)). The fifth curve (black line) in Figure 4.31(b) shows the IRF (measured according to Section 4.3.2). With IRF deconvolution and all lifetimes become slightly lower than using IRF reconvolution. This is because the first few picoseconds of the measurement are regarded as the signature of the detector.

4.3.3 Fast Calculation Intensity Threshold Method

A big disadvantage of lifetime determination methods based on curve-fitting is that they most commonly recur to `for` loops, where the lifetime of each pixel is determined individually, therefore consuming a great lot of time. Alternatively, the method proposed in this work evaluates the lifetime of the entire image at once, making it much faster.

The principle of this algorithm is illustrated in Figure 4.32. It calculates and normalizes the integral of a curve and determines the time t_i' at which it crosses the threshold $1 - 1/e$. Then, it compares it with the equivalent time t_{IRF}' for the IRF, such that the fluorescent lifetime is given by

$$\tau = t_i' - t_{IRF}' \tag{4.10}$$

This way, the effects of the measured IRF are compensated without having to deconvolve it from every measured curve. In spite of the simplicity of this method, the

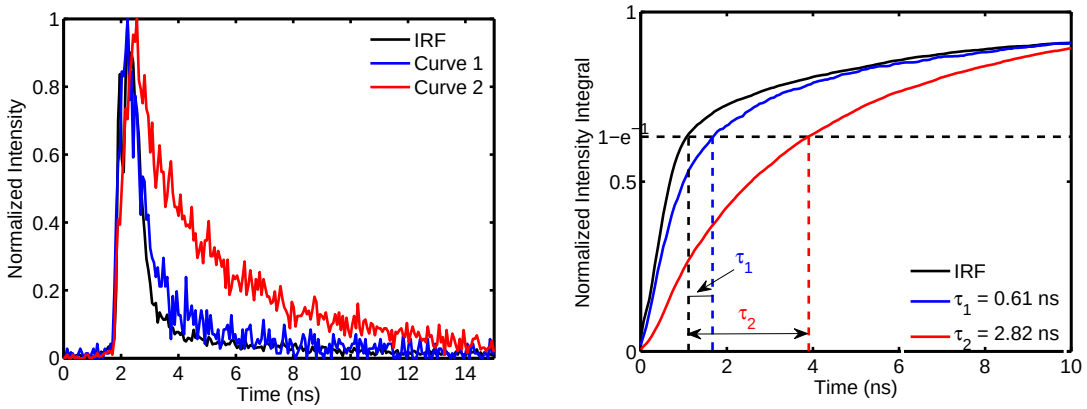

(a) (b)

Figure 4.32: Intensity threshold lifetime determination method. (a) Measurement of the IRF and two example curves. (b) The lifetime is given by difference between the times at which the integrals of a given measurement and the IRF reach the intensity threshold $1 - 1/e$. The matrix calculations can be performed for large data 3D matrices at once and therefore FLIM images are calculated much faster than other individual curve fitting-based algorithms.

results are very similar to those of the IRF reconvolution and deconvolution algorithms (a comparison of the three methods is shown in Section 4.3.4). This algorithm was fully developed during this master thesis and the most relevant parts of the MATLAB script is shown in the appendix A.2.2.

4.3.4 Comparison of the Methods

This section focuses on lifetime determination algorithms that compensate for the effects of the IRF (be that a modeled or a measured one). In particular, Figure 4.33 shows the final state of the DNA biosensor discussed in Section 4.2.2 calculated by the two Enderlein's algorithms (IRF deconvolution and reconvolution) and the intensity threshold algorithm developed for fast FLIM analysis. The fluorescence lifetime distribution of each method is presented in Figure 4.33(d). The results show that a) the IRF deconvolution and reconvolution algorithms output very different distributions - the former shows lower lifetimes and a much stronger contrast; b) the intensity threshold method algorithm is closer to the IRF deconvolution for short lifetimes but closer to the IRF reconvolution for longer lifetimes - its contrast resembles that of the former, but not quite so strong.

In general, the results from the intensity threshold method can be regarded as a mixture of the two curve-fitting based algorithms. Time consumption-wise, Figures 4.33(a), 4.33(b) and 4.33(c) required evaluation times of 138.03 s, 37.27 s and 1.97 s, respectively, meaning that the intensity threshold method was 70 times faster than the IRF deconvolution algorithm.

The three methods were used to calculate distance-dependent fluorescence lifetime

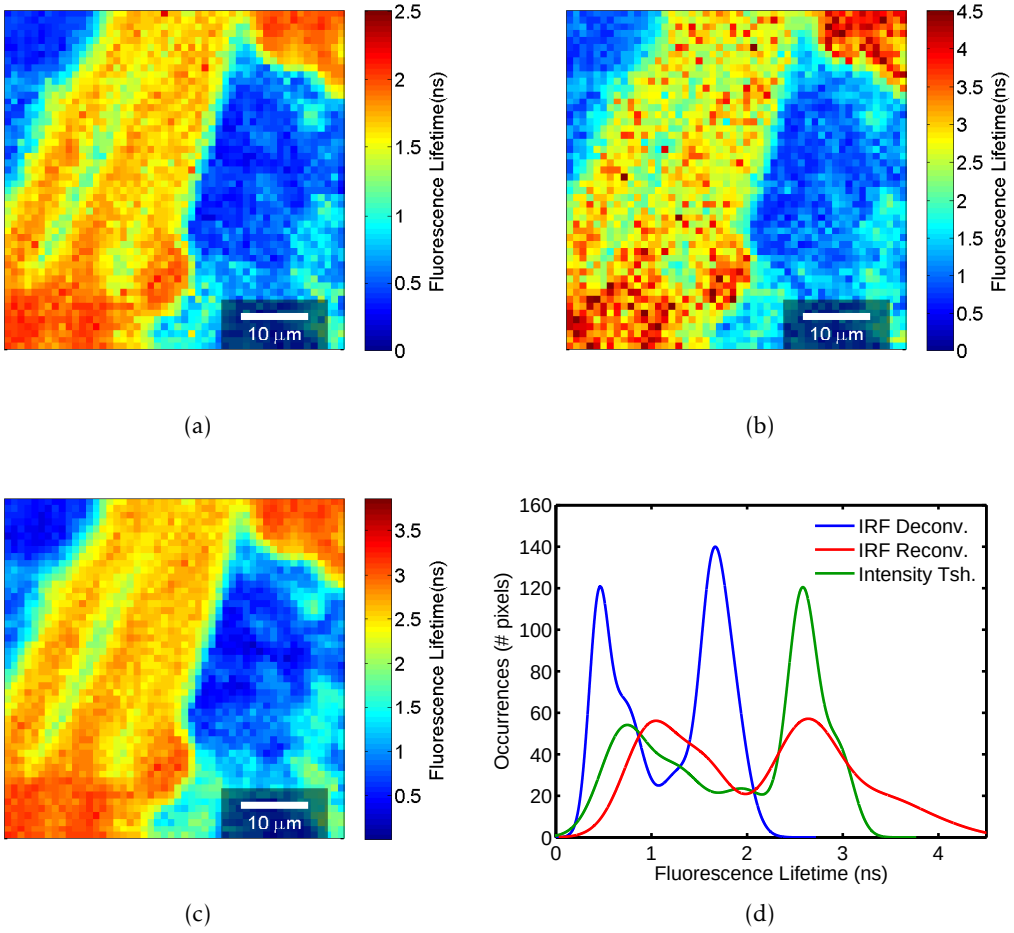

Figure 4.33: Comparison between different lifetime determination models and integration times (t_{integ}). (a) IRF deconvolution algorithm (t_{integ} = 138.03 s). (b) IRF reconvolution algorithm (t_{integ} = 37.27 s). (c) Intensity threshold algorithm(t_{integ} = 1.97 s). (d) Fluorescence lifetime distributions of the images in (a), (b) and (c). The intensity threshold method spreads over a fluorescence lifetime span that is intermediate to the other two algorithms, but took far less time to integrate. In the FLIM images, the IRF deconvolution shows perhaps the clearest structural contrast.

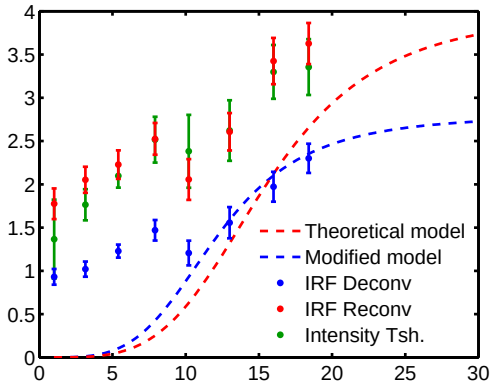

Figure 4.34: Comparison of distance-dependent fluorescence lifetime calibration curves, calculated with the three different models. The results are compared with the theoretical model from Gaudreau et al [25] and the semi-empirical model derived in Section 4.1.4.

calibration curves from the FLIM images of Figure 4.11 and the results are compared in Figure 4.34. In this plot, the intensity threshold method (green dots) is compared to the curves of Figure 4.15(b). A naked eye comparison of the methods indicates that the intensity threshold results are similar to those of IRF reconvolution, but actually slightly closer to theory (red curve).

The intensity threshold method implemented in this thesis is much faster than the other and can therefore be used as for fast determination of FLIM images. For a more accurate analysis however, well established fitting algorithms such as those implemented by Jörg Enderlein should be used. Both functions of Jörg Enderlein for IRF deconvolution and reconvolution have been implemented as standard algorithms in the MATLAB toolbox developed in this thesis (see Section 4.4), for user selection. Because the deconvolution of the experimental IRF in principle provides more accurate results, this method has been used for the fitting of all the results shown this thesis report.

4.4 Development of an Analysis Software in MATLAB

In parallel to the experimental work, a FLIM analysis platform was built in MATLAB for a user-friendly high-level interface. Figure 4.35 shows the FLIM analysis tab of the interface.

When a measurement is performed, data files are outputted from the LabVIEW device control software of the custom-built TCSPC-based FLIM setup, developed by Dr. Edite Figueiras and Dr. Jana B. Nieder (version 2017/01). The data is saved in a .bin file while the header information which contains scanner parameters as well as additional information is saved on a .hdf5 file. The measured fluorescence arrival time histograms are associated to a specific nanoscanner position, which can be derived from the header information and LabVIEW software-generated file name to form an image.

The program allows the user to a) import data files; b) to visualize the fluorescence intensity image and single TCSPC measurements within the image; c) to test a fitting algorithm for a single curve; d) to evaluate the FLIM image using IRF deconvolution or reconvolution models; e) to calculate the fluorescence lifetime distribution of the FLIM image and perform multiple-Gaussian curve fitting to the distribution; f) to build the reduced fluorescence lifetime distribution image; g) to export the results. More details about the interface can be found at the appendix A.3.1, about the toolbox internal structure in appendices A.3.2 and the its main functions in appendices A.3.3 to A.3.6

The internal structure of the toolbox was engineered such that users can have access to all variables and callbacks from the command window. Therefore the user can remotely call the in-built functions of the toolbox and input new variables, making it accessible for user-built extensions. The command window on the left pane also allows the user to run code and call other functions.

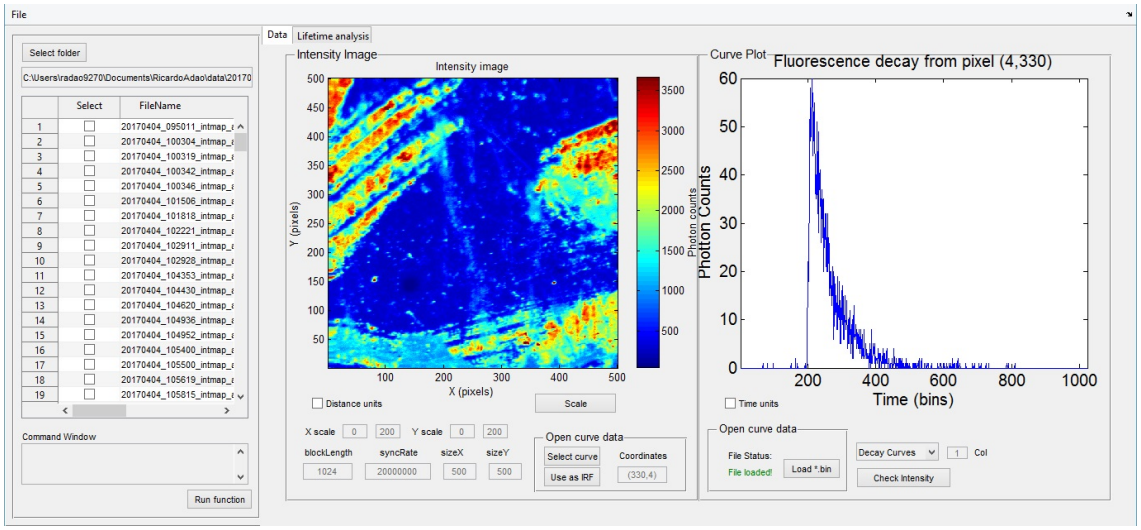

(a)

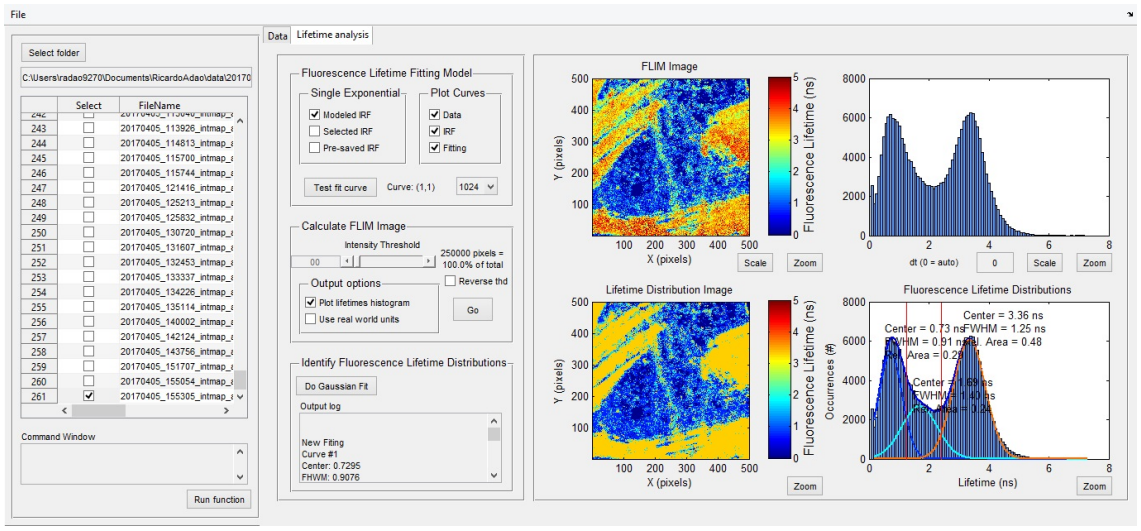

(b)

Figure 4.35: FLIM analysis interface of toolbox developed for MATLAB. The user can select a folder with multiple data files and the file to be open on the left pane. (a) Data visualization tab. The fluorescence intensity image and singular TCSPC measurements can be visualized. (b) Fluorescence lifetime analysis tab. The FLIM image, fluorescence lifetime distribution and reduced fluorescence lifetime image can be calculated and are displayed together in the same window.

Chapter 5

Conclusions and Outlook

The work developed throughout this master thesis experimentally confirmed the strong dependence of the fluorescence lifetime of a fluorescent dye with the nanoscale distance to graphene, in the range of 1 to 19.4 nm and its applicability for DNA biosensing.

The results for the lifetime dependence with distance showed, using a custom-built FLIM setup and a simple and innovative sample nanofabrication design, a partial agreement with theory that allowed the establishment of a semi-empiric calibration-curve. It was therefore shown to be possible to implement an axially-resolved nanoscale-distance sensing technique in a FLIM setup.

At an applied level, it was demonstrated that this method is suitable for the imaging of biological systems in aqueous solution, and its applicability for DNA biosensing. Particularly, it was possible to determine the spatial distribution of the bonding of DNA molecules in a functionalized graphene surface and the time-resolved monitoring of the DNA hybridization process, which allowed a study of the kinetics of reaction.

Two very distinct fluorescence lifetime features were identified, with correspondence to the probe DNA-beacon in its single-stranded folded configuration and its double-stranded hybridized configuration, which provided an estimation of the DNA molecular length that is in accordance with the expected length of the specific DNA sequence used. Furthermore, an intermediate state of the DNA hybridization was observed, where the biosensor probe and target molecules were only partially bound and the distance to the graphene was shorter than the full length of the strand.

An analysis software with a user-friendly interface was developed in MATLAB, which provided the tools analyzing the results presented in this report. This toolbox included features such as the construction of a FLIM image from TCSPC measurements, the calculation and Gaussian curve-fitting of its lifetime distribution, and reconstruction of a reduced lifetime distribution image for enhanced structural contrast.

Several fluorescence lifetime determination methods were compared, and can be selected by the user of the toolbox. The molecular architecture of the DNA sample allowed identifying the most accurate fitting algorithm, which is multiple exponential curve-fitting with deconvolution of the measured IRF of the setup from the measured decays. Furthermore, a fast lifetime-determination algorithm was implemented for up to 70 times faster integration times than IRF deconvolution, and similar results to well established curve fitting-based algorithms.

A manuscript for a scientific publication summarizing the work developed in this thesis is currently in preparation.

In future research, further development of the biosensor based on fluorescent lifetime measurements would include the study of the sensor's sensitivity to target concentration and specificity to the target strand sequence. Furthermore, the methods here used might be suited to analyze mutations in DNA strands and thus could have an impact in various sectors ranging from biology to medicine. Additionally, optimizing the experimental conditions to obtain a single-molecule regime, and study of the DNA binding spatial distribution and kinetics of hybridization reaction in single-molecule conditions in order to decouple eventual collective molecular group effects.

Bibliography

[1] A Draaijer and P. M. Houpt. "A Standard Video-Rate Confocal Laser-Scanning Reflection and Fluorescence Microscope". In: *SCANNING* 10 (1988), pp. 139–145.

[2] D Axelrod, N. L. Thompson, and T. P. Burghardt. "Total internal inflection fluorescent microscopy." In: *Journal of microscopy* 129.Pt 1 (1983), pp. 19–28.

[3] D. Braun and P. Fromherz. "Fluorescence interference-contrast microscopy of cell adhesion on oxidized silicon". In: *Applied Physics A: Materials Science & Processing* 65 (1997), pp. 341–348. DOI: 10.1007/s003390050589.

[4] J. R. Lakowicz, H. Szmacinski, K. Nowaczyk, K. W. Berndt, and M. Johnson. "Fluorescence Lifetime Imaging". In: *ANALYTICAL BIOCHEMISTRY* 202 (1992), pp. 316–330.

[5] P Bastiaens. "Fluorescence lifetime imaging microscopy: spatial resolution of biochemical processes in the cell". In: *Trends in Cell Biology* 9.2 (1999), pp. 48–52. DOI: 10.1016/S0962-8924(98)01410-X.

[6] M. A. Bopp, Y. Jia, L.-Q. Li, R. J. Cogdell, and R. M. Hochstrasser. "Fluorescence and photobleaching dynamics of single light-harvesting complexes." In: *Proceedings of the National Academy of Sciences of the United States of America* 94.20 (1997), pp. 10630–5. DOI: 10.1073/pnas.94.20.10630.

[7] D. J. Stephens and V. J. Allan. "Light Microscopy Techniques for Live Cell Imaging". In: *Sciences* 300.2003 (2003), pp. 82–86. DOI: DOI:10.1126/science.1082160.

[8] S. Trautmann, V. Buschmann, S. Orthaus, F. Koberling, U. Ortmann, and E. Rainer. *Fluorescence Lifetime Imaging (FLIM) in Confocal Microscopy Applications: An Overview*. 2013.

[9] T. Nieh, I. Gregor, B. Kr, R. Rahn, M. Patting, F. Koberling, R. Enderlein, and M. Sauer. "Multi-target spectrally resolved fluorescence lifetime imaging microscopy". In: *Nature Methods* (2016), pp. 1–6. DOI: 10.1038/nmeth.3740.

[10] T. Förster. "Energiewanderung und Fluoreszenz". In: *Die Naturwissenschaften* 33.6 (1946), pp. 166–175. DOI: 10.1007/BF00585226.

[11] T. Förster. "Zwischenmolekulare Energiewanderung und Fluoreszenz". In: *Annalen der Physik* 437.1-2 (1948), pp. 55–75. DOI: 10.1002/andp.19484370105.

[12] T. Förster. "Energy migration and fluorescence". In: *Journal of Biomedical Optics* 17.1 (2012), pp. 166–175. DOI: 10.1117/1.JBO.17.1.011002.

[13] E. V. Mielczarek, E. S. Greenbaum, and R. S.R. S. Knox. *Biological physics*. American Institute of Physics, 1993, p. 421.

[14] H. Kuhn and D. Mobius. "Systems of Monomolecular Layers-Assembling and Physico-Chemical Behavior". In: *Angewandte Chemie International Edition* 10.9 (1971), pp. 620–637.

[15] R. R. Chance, A Prock, and R Silbey. "Molecular Fluorescence and Energy Transfer Near Interfaces". In: *Advance in Chemical Physics* 37 (1978), pp. 1–65.

[16] G. W. Ford, W. O. Weber, and W. H. Weber. "Electromagnetic Interactions of Molecules with Metal Surfaces". In: *PHYSICS REPORTS (Review Section of Physics Letters)* 113.4 (1984), pp. 195–287.

[17] C. H. D.H. Waldeck, A.P. Alivisatos. "Nonradiative Damping of Molecular Electronic Excited States by Metal Surfaces". In: *Surface Science* 158 (1985), pp. 103–125.

[18] G. Schneider, G. Decher, N. Nerambourg, R. 1ssa Praho, M. H. V. Werts, and M. Blanchard-Desce. "Distance-Dependent Fluorescence Quenching on Gold Nanoparticles Ensheathed with Layer-by-Layer Assembled Polyelectrolytes". In: *Nano Letters* 6.3 (2006), pp. 530–536. DOI: 10.1021/nl052441s.

[19] T. L. Jennings, M. P. Singh, and G. F. Strouse. "Fluorescent Lifetime Quenching near d) 1.5 nm Gold Nanoparticles: Probing NSET Validity". In: *Journal of the American Chemical Society* 128.16 (2006), pp. 5462–5467. DOI: 10.1021/ja0583665.

[20] G. P. Acuna, M. Bucher, I. H. Stein, C. Steinhauer, A. Kuzyk, P. Holzmeister, R. Schreiber, A. Moroz, F. D. Stefani, T. Liedl, F. C. Simmel, and P. Tinnefeld. "Distance Dependence of Single- Fluorophore Quenching by Gold Nanoparticles Studied on DNA Origami". In: *ACS Nano* 6.4 (2012), pp. 3189–3195. DOI: 10.1021/nn2050483.

[21] M. Berndt, M. Lorenz, J. Enderlein, and S. Diez. "Axial nanometer distances measured by fluorescence lifetime imaging microscopy". In: *Nano Letters* 10.4 (2010), pp. 1497–1500. DOI: 10.1021/nl100593x.

[22] A. I. Chizhik, J. Rother, I. Gregor, A. Janshoff, and J. Enderlein. "Metal-induced energy transfer for live cell nanoscopy". In: *Nature Photonics* 8 (2014), pp. 124–127. DOI: 10.1038/nphoton.2013.345.

[23] N. Karedla, A. I. Chizhik, I. Gregor, A. M. Chizhik, O. Schulz, and J. Enderlein. "Single-molecule metal-induced energy transfer (smMIET): Resolving nanometer distances at the single-molecule level". In: *ChemPhysChem* 15.4 (2014), pp. 705–711. DOI: 10.1002/cphc.201300760.

[24] R. J. Moerland and J. P. Hoogenboom. "Subnanometer-accuracy optical distance ruler based on fluorescence quenching by transparent conductors". In: *Optica* 3.2 (2016), p. 112. DOI: 10.1364/OPTICA.3.000112.

[25] L. Gaudreau, K. J. Tielrooij, G. E.D. K. Prawiroatmodjo, J. Osmond, F. J. García de Abajo, and F. H. L. Koppens. "Universal Distance-Scaling of Non-radiative Energy Transfer to Graphene". In: *Nano Letters* 13 (2013), pp. 2030–2035. DOI: 10.1103/PhysRevB.75.205418.

[26] O. Salihoglu, N. Kakenov, O. Balci, S. Balci, and C. Kocabas. "Graphene as a Reversible and Spectrally Selective Fluorescence Quencher". In: *Scientific Reports* 6.1 (2016), p. 33911. DOI: 10.1038/srep33911.

[27] F. Federspiel, G. Froehlicher, M. Nasilowski, S. Pedetti, A. Mahmood, B. Doudin, S. Park, J.-O. Lee, D. Halley, B. Dubertret, P. Gilliot, and S. Berciaud. "Distance dependence of the energy transfer rate from a single semiconductor nanostructure to graphene". In: *Nano Letters* 15.2 (2015), pp. 1252–1258.

[28] H. Gonçalves, C. Bernardo, C. Moura, R. A. S. Ferreira, P. S. André, T. Stauber, M. Belsley, and P. Schellenberg. "Long range energy transfer in graphene hybrid structures". In: *Journal of Physics D: Applied Physics* 49.31 (2016), p. 315102. DOI: 10.1088/0022-3727/49/31/315102.

[29] R. S. Swathi and K. L. Sebastian. "Distance dependence of fluorescence resonance energy transfer". In: *Journal of Chemical Sciences* 121.5 (2009), pp. 777–787. DOI: 10.1007/s12039-009-0092-x.

[30] R. S. Swathi and K. L. Sebastian. "Resonance energy transfer from a dye molecule to graphene". In: *J. Chem. Phys.* 129.054703 (2008), pp. 1–9. DOI: 10.1063/1.2956498ÍŤ.

[31] N. C. Seeman. "Biochemistry and structural DNA nanotechnology: An evolving symbiotic relationship". In: *Biochemistry* 42.24 (2003), pp. 7259–7269. DOI: 10.1021/bi030079v.

[32] P. Malik, V. Katyal, V. Malik, A. Asatkar, G. Inwati, and T. K. Mukherjee. "Nanobiosensors: Concepts and Variations". In: *ISRN Nanomaterials* 2013 (2013), pp. 1–9. DOI: 10.1155/2013/327435.

[33] P. Martins-Lopes, S. Gomes, L. Pereira, and H. Guedes-Pinto. "Molecular markers for food traceability". In: *Food Technology and Biotechnology* 51.2 (2013), pp. 198–207.

[34] J. R. Fernandes, L. Pereira, P. Jorge, L. Moreira, H. Gonçalves, L. Coelho, D. Alexandre, J. Eiras-Dias, J. Brazão, P. Clímaco, M. Baleiras-Couto, S. Catarino, A. Graça, and P. Martins-Lopes. "Wine fingerprinting using a bio-geochemical approach". In: *BIO Web of Conferences* 5 (2015), pp. 1 –4. DOI: 10.1051/bioconf/20150502021.

[35] E. E. Ferapontova. "Hybridization Biosensors Relying on Electrical Properties of Nucleic Acids". In: *Electroanalysis* 29.1 (2017), pp. 6–13. DOI: 10.1002/elan.201600593.

[36] C. Fan, K. W. Plaxco, and A. J. Heeger. "Electrochemical interrogation of conformational changes as a reagentless method for the sequence-specific detection of DNA". In: *Proceedings of the National Academy of Sciences* 100.16 (2003), pp. 9134–9137. DOI: 10.1073/pnas.1633515100.

[37] J. M. Chalovich and E. Eisenberg. "Folding-based electrochemical biosensors: the case for responsive nucleic acid architectures". In: *Biophysical Chemistry* 43.4 (2010), pp. 496–505. DOI: 10.1016/j.immuni.2010.12.017.Two-stage.

[38] E. Farjami, L. Clima, K. Gothelf, and E. E. Ferapontova. "'off-On' electrochemical hairpin-DNA-based genosensor for cancer diagnostics". In: *Analytical Chemistry* 83.5 (2011), pp. 1594–1602. DOI: 10.1021/ac1032929.

[39] P. Atkins and J. De Paula. *Physical Chemistry*. Oxford University Press, 2010.

[40] B. Valeur. *Molecular Fluorescence: Principles and Applications*. Ed. by W. V. V. HmbH. Vol. 8. New York, 2001, p. 399. ISBN: 3-527-60024-8.

[41] S. Prahl. *Fluorescein*. 2017. URL: http://omlc.org/spectra/PhotochemCAD/html/037.html (visited on 06/20/2017).

[42] J. Albani. *Principles and applications of fluorescence spectroscopy*. 2008, pp. 96–100.

[43] I. Medintz and N. Hildebrandt. *FRET - Förster Resonance Energy Transfer*. 2013, p. 33. DOI: 10.1002/9783527656028.

[44] W. L. Barnes. "Fluorescence near interfaces: the role of photonic mode density". In: *Journal of Modern Optics* 45.4 (1998), pp. 661–699. DOI: 10.1080/095003498151582.

[45] L. A. Blanco and F. J. García De Abajo. "Spontaneous light emission in complex nanostructures". In: *Physical Review B - Condensed Matter and Materials Physics* 69.20 (2004), pp. 1–12. DOI: 10.1103/PhysRevB.69.205414.

[46] R. S. Swathi and K. L. Sebastian. "Long range resonance energy transfer from a dye molecule to graphene has (distance)-4 dependence". In: *Journal of Chemical Physics* 130.8 (2009), pp. 128–131. DOI: 10.1063/1.3077292. arXiv: 0703030 [physics].

[47] R. R. Nair, P. Blake, A. N. Grigorenko, K. S. Novoselov, T. J. Booth, T. Stauber, N. M. R. Peres, and A. K. Geim. "Fine Structure Constant Defines Visual Transparency of Graphene". In: *Science* 320.5881 (2008), p. 1308. DOI: 10.1126/science.1156965.

[48] L. M. S. Loura. "Simple estimation of Förster Resonance Energy Transfer (FRET) orientation factor distribution in membranes." In: *International journal of molecular sciences* 13.11 (2012), pp. 15252–70. DOI: 10.3390/ijms131115252.

[49] M. Wahl. *Time-Correlated Single Photon Counting*. Berlin, 2014.

[50] J. B. Pawley. *Handbook of Biological Confocal Microscopy*. Springer US, 1995.

[51] W. Becker, A. Bergmann, M. Hink, K. König, K. Benndorf, and C. Biskup. "Fluorescence lifetime imaging by time-correlated single-photon counting". In: *Microscopy Research and Technique* 63.1 (2004), pp. 58–66. DOI: 10.1002/jemt.10421.

[52] E. P. Buurman, R. Sanders, A. Draaijer, H. C. Gerritsen, J. J. F. Van Veen, P. M. Hour, and Y. K. Levinet. "Fluorescence Lifetime Imaging Using a Confocal Laser Scanning Microscope". In: *SCANNING* 14 (1992), pp. 155–159.

[53] C. To and W. Becker. "Fluorescence lifetime imaging – techniques and applications". In: *Journal of Microscopy* 247.2 (2012), pp. 119–136. DOI: 10.1111/j.1365-2818.2012.03618.x.

[54] H.-J. Lin, P. Herman, and J. R. Lakowicz. "Fluorescence Lifetime-Resolved pH Imaging of Living Cells". In: *Cytometry* 52A (2002), pp. 77–89. DOI: 10.1002/cyto.a.10028.

[55] K. Okabe, N. Inada, C. Gota, Y. Harada, T. Funatsu, and S. Uchiyama. "Intracellular temperature mapping with a fluorescent polymeric thermometer and fluorescence lifetime imaging microscopy". In: *Nature Communications* 3 (2012). DOI: 10.1038/ncomms1714.

[56] C. V. Raman and F. R.S. Plate. "A New Radiation". In: *Indian J. Phys* 2 (1928), pp. 387–398.

[57] R. Singh. "C.V. Raman and the Discovery of the Raman Effect". In: *Physics in Prespective* 4 (2002), pp. 399–420.

[58] H. Edwards. *Handbook of Raman Spectroscopy*. Marcel Dekker, Inc., 2001.

[59] E. C. Le Ru and P. G.P. G. Etchegoin. *Principles of surface-enhanced Raman spectroscopy : and related plasmonic effects*. Elsevier, 2009, p. 663.

[60] H. W. Qiu, S. C. Xu, P. X. Chen, S. S. Gao, Z. Li, C. Zhang, S. Z. Jiang, M. Liu, H. S. Li, and D. J. Feng. "A novel surface-enhanced Raman spectroscopy substrate based on hybrid structure of monolayer graphene and Cu nanoparticles for adenosine detection". In: *Applied Surface Science* 332 (2015), pp. 614–619. DOI: 10.1016/j.apsusc.2015.01.231.

[61] A. C. Ferrari, J. C. Meyer, V Scardaci, C Casiraghi, M Lazzeri, F Mauri, S Piscanec, D Jiang, K. S. Novoselov, S Roth, and A. K. Geim. "Raman Spectrum of Graphene and Graphene Layers". In: *Physical Review Letters* 97 (2006). DOI: 10.1103/PhysRevLett.97.187401.

[62] L. Biomass. "Ellipsometry". In: *Polarized Light*. Vol. 20. 2005. Chap. 24, pp. 2–5. DOI: 10.1016/B978-0-12-386944-9.50024-8.

[63] B. Alberts, A. Johnson, J. Lewis, M. Raff, K. Roberts, and P. Walter. "Basic Genetic Mechanisms". In: *Molecular biology of the cell*. 4th. Garland Science, 2002. Chap. 4 - 5, p. 1464.

[64] T. G. G. Inc. *DNA Hybridization facts, information, pictures | Encyclopedia.com articles about DNA Hybridization*. 2009. URL: http://www.encyclopedia.com/science-and-technology/biology-and-genetics/genetics-and-genetic-engineering/dna-hybridization (visited on 07/23/2017).

[65] V. Georgakilas. *Functionalization of graphene*. Ed. by V. Georgakilas. Wiley, 2014, p. 424. ISBN: 9783527335510.

[66] T. Nolan and S. A. Bustin. *PCR technology : current innovations*. Ed. by T. Nolan and S. A. Bustin. 3rd ed. CRC Press, 2013, p. 435. ISBN: 9781439848050.

[67] V. K. Kodali, J. Scrimgeour, S. Kim, J. H. Hankinson, K. M. Carroll, W. A. De Heer, C. Berger, and J. E. Curtis. "Nonperturbative Chemical Modification of Graphene for Protein Micropatterning". In: *Langmuir* 27.3 (2011), pp. 863–865. DOI: 10.1021/la1033178.

[68] W. Becker. *16 Channel TCSPC / FLIM Detectors*. Berlin: Becker & Hickl, 2016, p. 63.

[69] PicoQuant. *How to Measure the Instrument Response Function (IRF) - Time Correlated Single Photon Counting Wiki*. 2016. URL: http://www.tcspc.com/doku.php/howto:how{_}to{_}measure{_}the{_}instrument{_}response{_}function{_}irf (visited on 04/06/2017).

[70] R. S. Swathi and K. L. Sebastian. "Resonance energy transfer from a dye molecule to graphene". In: *Journal of Chemical Physics* 129.5 (2008). DOI: 10.1063/1.2956498.

[71] S. H. Gage. "Modern Dark-Field Microscopy and the History of Its Development HISTORY OF ITS DEVELOPMENT". In: *Source: Transactions of the American Microscopical Society* 39210237.2 (1920), pp. 95–141.

[72] X. H. Kong, H. X. Ji, R. D. Piner, H. F. Li, C. W. Magnuson, C Tan, A Ismach, H Chou, and R. S. Ruoff. "Non-destructive and rapid evaluation of chemical vapor deposition graphene by dark field optical microscopy". In: *Citation: Appl. Phys. Lett* 103.043119 (2013). DOI: 10.1063/1.4816752.

[73] O. Optics. *NanoCalc - Ocean Optics*. 2017. URL: https://oceanoptics.com/product/nanocalc/ (visited on 07/18/2017).

[74] ISS. *ISS Data Tables | Lifetime Data of Selected Fluorophores*. 2017. URL: http://www.iss.com/resources/reference/data{_}tables/LifetimeDataFluorophores.html (visited on 10/01/2017).

[75] Connell Group. *Selected Bond Energies and Bond Lengths*. Texas, 2009. URL: http://www.chem.tamu.edu/rgroup/connell/linkfiles/bonds.pdf.

[76] R Kiralj and M. M. C. Ferreira. "On Heteroaromaticity of Nucleobases. Bond Lengths as Multidimensional Phenomena". In: *Journal of Chemical Information and Computer Sciences* 43 (2002), pp. 787–809. DOI: 10.1021/ci0200523.

[77] H. F. Lodish. *Molecular cell biology*. W.H. Freeman, 2008. ISBN: 0716743663.

[78] Leica Microsystems. *FRET with FLIM, Quantitative In-vivo Biochemistry*. 2009.

[79] T. O'Haver. *Intro. to Signal Processing:Deconvolution*. 2008. URL: https://terpconnect.umd.edu/{~}toh/spectrum/Deconvolution.html (visited on 06/16/2017).

[80] J. Enderlein and R. Erdmann. "Fast fitting of multi-exponential decay curves". In: *Optics Communications* 134 (1997), pp. 371–378.

Appendix A

Developed MATLAB Scripts for Data Visualization and Analysis

A.1 Determination of Physical parameters for Graphene RET Model

The equations from the Förster theory shown in Section 2.1.4.1 depend on the emission wavelength λ of donor and the dielectric constant ϵ of the medium. Considering the medium to be SiO_2 spacer, the two quantities were calculated using the emission spectrum of fluorescein and the wavelength dependent refractive index of SiO_2.

In the script, the dielectric constant c_E_Si02 is determined by multiplying the normalized emission spectrum by the SiO_2 refractive index, which is then converted into the dielectric function using $\epsilon = (n + i\kappa)^2$. The average emission wavelength is calculated simply by weighting the emission spectrum of the fluorescein. The resulting values were $\epsilon = 2.19$ and $\lambda = 534.0$ nm.

```
f_ES = fluorescein_EmissionSpectrum; % normalized emission spectrum
SiO2_DF = SiO2_refractiveIndex;   % Refractive index of SiO2
c_E_SiO2 = 0;
% Calculate weighted average dielectric constant
for i = 1 : size(f_ES,1)
    % get wavelength
    w = f_ES(i,1);
    % find the closest value in the dielectric function
    [~,w_i] = min(abs(w-SiO2_DF(:,1)));
    c_E_SiO2 = c_E_SiO2 + (SiO2_DF(w_i,2)+SiO2_DF(w_i,3))^2*f_ES(i,2);
end
% calculate the mean wavelength
wv0 = sum(f_ES(:,1).*f_ES(:,2));
```

A.2 Lifetime Determination Algorithms

This appendix presents the most important fractions of MATLAB script used in the implementation lifetime determination algorithms used in this thesis.

A.2.1 IRF Reconvolution

The IRF reconvolution and deconvolution functions were implemented using scripts from J org Enderlein, in this case, the `DistTailfit` and `DistFluoFit`, respectively [80]. For simplicity, this section shows only how to use the IRF reconvolution algorithm, but the IRF deconvolution using `DistFluoFit` is very similar. To produce a FLIM image, this script is called inside a `for` loop, to calculate the lifetime of each pixel.

The variable `dataCol` is a column array that contains one TCSPC measurement. First, it is determined where the signal and the fluorescence intensity peak are located, using a custom-built function `findPeak`. Then, the `DistTailfit` function is called by inputting the data curve `y`, the time resolution `dt` and the probability of photos on excitation `epsilon`. `cx` and `tau` are weights and lifetime values of the n-exponential fit, respectively. The lifetime is calculated according to Equation 2.12.

```
%Find the signal start and end and trim data
signalStart = find(dataCol,1);
signalEnd = find(dataCol,1,'last');
dataCol = dataCol(signalStart:signalEnd);
% Find the initial and final positions of the curve
[peakStart,peakEnd] = findPeak(dataCol,ADCresolution);
y = dataCol(peakStart:peakEnd);
x_y_0 = signalStart+peakStart;
pxDwellTime = 0.006;  %Dwell time of the detector
% calculate time interval dt
p = double(10^9/syncRate);
dt = p/length(dataCol);
epsilon = sum(y)/pxDwellTime/syncRate; %probability to detect a photon between
    two excitation pulses
% use IRF reconvolution algorithm from Jorg Enderlein
[cx, tau, offsetM, z, tM, err,irfM,M0] = DistTailfit(double(y), dt, [], [],
    [], [], epsilon);
% Calculate lifetime
lifetime = sum(cx.*tau)/sum(cx);
```

A.2.2 Intensity Threshold Method

The key for the fast determination of the lifetimes is to evaluate the entire image ate once, therefore avoiding time-consuming `for` loops. The variables `data` and `irf` contain the TCSPC measurements of the image and the IRF, respectively[1]. The integrals of

[1] IRF is a 1D array and data is a 3D matrix.

the data and IRF are calculated and each integral is normalized to its maximum. Then the positions at which the integrals cross `intFact` are determined, where `inteFact = 1 - 1/exp(1)` and the lifetimes are calculated according to Equation 4.10. All these calculations are performed using the function `bsxfun`, which is a standard function in MATLAB for operations between multi-dimensional matrix

In the complete script, once this first approximation is found, the curves are interpolated around `ts` and `ts_irf` in order to increase the resolution of the output lifetimes.

```
% calculate the integral from the max to end
integ = cumsum(data,3);
integ_irf = cumsum(irf);
%normalized integ
integ = bsxfun(@rdivide,integ,max(integ,[],3));
integ_irf = integ_irf/max(integ_irf);
% find where the integral reaches intFact
[~,ts] = min(abs(bsxfun(@minus,integ,intFact)),[],3);
[~,ts_irf] = min(abs(integ_irf-intFact));
% Calculate FLIM image
flimImage = dt*((ts-1)-(ts_irf-1));
```

A.3 Analysis Software Package for MATLAB

This appendix describes some of the main features of the software package in MATLAB developed for the analysis of FLIM results. The internal structure of the program and some of its main variables will be briefly described. The most relevant fraction of the MATLAB scripts and functions will be presented.

A.3.1 Interface

The interface of the software is shown in Figure 4.35 and it is divided into three main structures: the file selecting panel on the left, the data visualization tab and the lifetime analysis tab.

The "Select folder" button prompts an explorer window for the user to select the directory where the data is stored and the list of .hdf5 files appears on the left panel. The command window below the file list can be used for running small scripts or calling extension functions. If the 'Run function' button is pressed with an empty command window, a window prompt allows the user to browse for a previously saved function.

On the data visualization tab (Figure 4.35(a)), once a user-selected file is opened, the intensity image is shown and the user can use the "Select curve" button to visualize a specific TCSPC measurement (Figure A.1(a)). For the case of ultra-short lifetime measurements, the "Use as IRF" button defines the currently selected curve as the experimentalIRF.

On the lifetime analysis tab (Figure 4.35(b)), the lifetime determination properties can be selected on the "Fluorescence Lifetime Fittin Model" and "Calculate FLIM image"

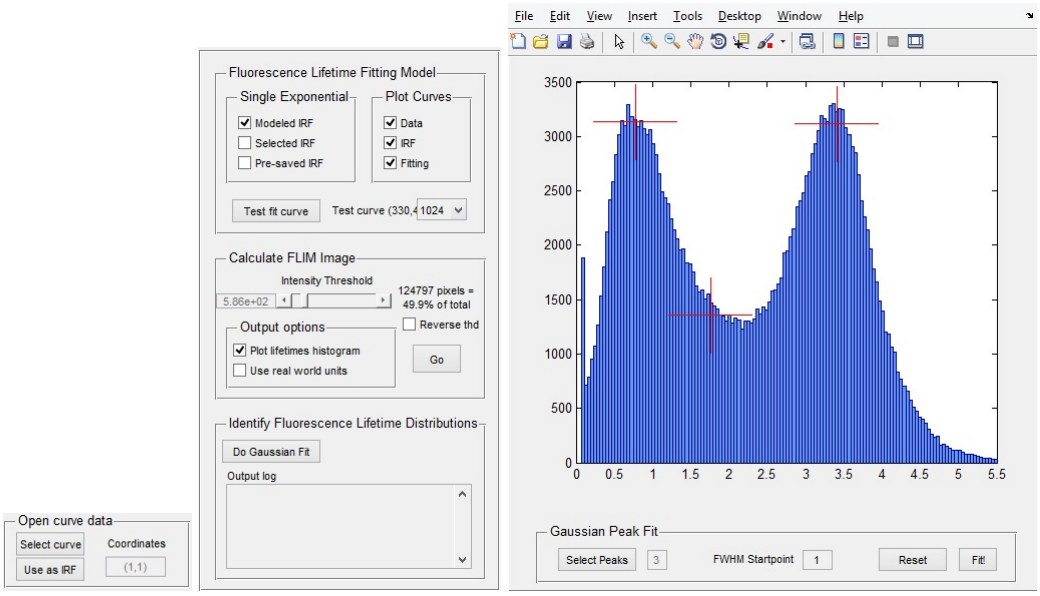

(a) (b) (c)

Figure A.1: Features of the interface. (a) Panel for selection of single curve visualization and IRF selection from the current dataset. (b) Panel with lifetime analysis options. (c) Interface for Gaussian curve-fitting of the lifetime distribution.

panels (Figure A.1(b)). The former selects the lifetime fitting algorithm and the latter defines an intensity threshold for a partial image evaluation. If the "Go" button is presses, the lifetime image is calculated and displayed on the top left set of axes. If the "Plot lifetimes histogram" checkbox is activated, the lifetime distribution is calculated and displayed on the top-right set of axes. After the lifetime distribution has been calculated, pressing the 'Do Gaussian fit' opens a curve-fitting GUI (Figure A.1(c)) where the user can select the starting parameters for the position and width of 1 to 8 Gaussian peaks. The results of the Gaussian Curve-fitting re shown on the bottom right set of axes and the reduced lifetime distribution image is calculated from the fit results and displayed on the bottom left set of axes.

A.3.2 Internal structure

The `NanoPhotonicsToolbox` in MATLAB saves all its contents into two variables: `flim` and `vars`. From the user point of view, the `flim` is the main variable of the toolbox, for it contains all the data and analysis results.

Once the user selects a directory in the interface, `flim` assumes the form of an array of `struct` variables with `N+1` indexes, where `N` is the number of datasets in the selected folder. The first index of the structure `flim(1)` is a *floating structure* that is reserved for data of the currently open dataset, so its contents will change every time the user selects a different file. The remaining indexes of `flim(2:end)` contain the information regarding the $(n-1)^{th}$ file in the folder.

Table A.1: The "flim" structure. List of all the fields and sub-fields where data is stored in the flim structure.

flim	analysisSettings	fluorescenceLifetimeModel intensityThreshold plotHist getDistributions useSameStartPoints	
	navigation	directory	
	fileName		
	head	blockLength syncRate sizeX sizeY startX endX startY endY	
	intensity	raw calculated	
	data		
	lifetimes	image histogram	
		histogramFit	curveCoefficients fwhm relativeAreas distInterceptions histGaussFitParams lifetimeDistributionIndexCurve

The fields of the `flim(1)` are shown in Table A.1. The field `flim(1).analysisSettings` holds the main analysis options selected by the user, such that the same parameters can be used for multiples files. The field `flim(1).navigation` holds the chosen directory. Only `flim(1)` contains these two fields for they are common to all the others. The field `flim(1).fileName` contains the name of the currently open file. The field `flim(1).head` contains information regarding acquisition parameters of the measurement. The field `flim(1).intensity` contains the fluorescence intensity image of the measurement. The field `flim(1).data` contains all the TCSPC measurements of the currently open dataset.

The data from an image with 50×50 pixels typically weights around 10 MB and it scales linearly with its area (or width the square of its width for a squared image). This means that an image with 100×100 pixels weights 40 MB and an image with 200×200 weights 160 MB. Therefore, to avoid loading all this data into MATLAB, only `flim(1)` will have this field filled with data of the currently open dataset. All the others will be empty. The field `flim(1).lifetimes` contains all the lifetime analysis results.

Table A.2: Structure of the Nanophotonics toolbox. The numbers in brackets indicate the number of files in each directory.

NanoPhotonicsToolbox.m	
File (7)	File_Loading (5) File_Saving (1)
FLIM_Structure (12)	
Data_Management (26)	Fitting (15)
Data_Files (7)	
GUI (99)	Assigns (2) Callbacks (50) Closing (2) Initialization (19) Update_Values (26)
Extensions (22)	DataProcessing (3) Exports (6) LifetimeCalculations (3) LoadFiles (2) Maths (1) Plots (6) Subfiles (1)
Auxiliary (15)	General (11) Maths (4)

The files of the toolbox are divided into the seven folders shown in Table A.2. "File" contains the functions for file loading and saving. "FLIM_Structure" contains the functions for storing, transferring and organizing the variables in the `flim` structure. "Data_Management" contains the functions that are most specific of the FLIM data processing. The most important functions for the analysis shown in this master thesis can be found in this directory. "Data_Files" contains *.mat files with useful variables like `colormaps` and calibration curves. "GUI" contains the functions for generating the interface. "Extensions" contains functions that complement those functions that are available on the interface. This toolbox is built in such way that users can easily expand it for their own needs. "Auxiliary" folder contains generic functions that are transversal to many applications. These are usually modifications to standard functions of MATLAB or simply small useful functions.

A.3.3 Importing Data

The scripts shown in this section are excerpts from function:

```
1 [dataHDF5,syncRate,blockLength,sizeX,sizeY,dataBIN,startX,endX,startY,endY] =
      flimLoadFileName(filename)
```

When a measurement is performed, data files are outputted from the LabVIEW device control software of the custom-built TCSPC-based FLIM setup, developed by Edite Figueiras and Jana Nieder (version 2017/01). The data is saved in a .bin file while the

header information which contains scanner parameters as well as additional information is saved on a .hdf5 file.

When the user selects the file to open in the interface, the path and file name are stored in the variable `filename`. The variables `sizeX`, `sizeY` and `blocklength` are extracted from the *.hdf5 file and correspond to the number of pixels in the x and y directions, and the number of bins in the time domain (temporal resolution of the TCSPC measurement). The TCSPC measurements themselves are arranged in a single 1D array `dataBIN` of length `sizeX*sizeY*blockLength` which is extracted from the .bin file.

```
binFilename = [filename,'.bin'];  %Add the bin extension
fileID = fopen(binFilename);    %Open the *.bin file
dataBIN = fread(fileID,[nrows ncols],'uint', 'b');  %Read *.bin file
```

To facilitate the access to the data, the `dataBIN` is rearranged into a 3D matrix such that at the position of each pixel there is a 1D array of data containing its respective TCSPC measurement. The success of the loading of data is confirmed by calculating the integral of the TCSPC measurement of each pixel `dataHDF5` and comparing with the intensity image stored in the *.hdf5.

```
dataBIN = reshape(dataBIN,[blockLength sizeX*sizeY]); % reshape to side-by-
    size columns
dataBIN = reshape(dataBIN',[sizeX sizeY blockLength]);  % reshape to 3D format
dataBIN = permute(dataBIN,[2 1 3]); % permute x and y
dataHDF5= sum(dataBIN,3); % intensity image
```

A.3.4 Calculating a FLIM Image

The script shown in this section are excerpts from function

```
lifetimes = fitAllData(flim,flimIndex,shiftFromPeak,fitOptions,nData,intFactor
    ,maxInt)
```

The script in this appendix shows an example for the determination of a FLIM image using IRF deconvolution, where the function `fitTCSPC_irf` uses a J org Enderlein algorithm for the fitting. For IRF reconvolution, a function `fitTCSPC` was implemented which is called in MATLAB using the same parameters as `fitTCSPC_irf` except that no `irf` input is required.

In the script, the data and an experimental IRF measurement are loaded from the `flim` structure to the variables `data` and `irfA`, respectively. A `for` loop is used to scan through the `data` matrix and uses the function `fitTCSPC_irf` to calculate the lifetime in each pixel of the matrix `lifetimes`.

Because each curve is treated individually, the algorithm can take several seconds or even minutes to evaluate the full image. The IRF deconvolution from the data is also be very much time-consuming, as the function `fitTCSPC_irf` takes approximately 3.7 times longer than `fitTCSPC` to evaluate the same data set.

```
data = flim(flimIndex).data;    % load data
irfA = vars.variables.arrays.irf; % load IRF
for mx = 1:size(data,1)
  for my = 1:size(data,2)
    % Only evaluate where pixels2Calculate == 1
    if pixels2Calculate(mx,my)
      y = squeeze(data(mx,my,:));
      [lifetimes(mx,my),tau,cx,y,irf,zLI] = fitTCSPC\_irf(y,irfA,flim(
          flimIndex).head.syncRate,fitOptions(4));
    end
  end
end
```

A.3.5 Fluorescence Lifetime Distribution

The fluorescence lifetime distribution represents the occurrences of lifetime values obtained in one FLIM image in the form of a histogram. Its shape can then be Gaussian curve-fitted to extract relevant information.

A.3.5.1 Calculation of the Lifetime Distribution

The Listings shown in this section are excerpts from function

```
[histResults,yHistGaussFit,binWidthGaussFit,xFirstGaussFit] = plotNewHistogram
    (axesIn,matrix)
```

In the script of the function, the variable `matrix` contains the fluorescence lifetime image. The variable `dtUser` contains the width of the histogram bins, defined by the user. If this parameter is set to zero in the interface, then the number of bins is determined using the Freedman-Diaconis rule. The fluorescence lifetime distribution is calculated using the standard MATLAb function `hist` using the number of bins `nbins`.

```
vecRaw = matrix(:);  % Reduce FLIM image to a 1D array
if dtUser ~=0  % Define the number of bins based on the user defined bin width
    dt
  dt = dtUser;
  lm = min(min(matrix(matrix>0)));
  lM = max(matrix(:));
  nbins = round((lM-lm)/dt);
else  % calculate the number of bins based on the Freedman-Diaconis rule
  n = double(numel(vec));
  h = 2*double(iqrRA(vec))*double(n^(-1/3));
  nbins = double(max(vec)-min(vec))/h;
end
axes(axesIn);     % Axes for plotting the histogram
[counts,centers] = hist(vec,nbins); % Save the results
hist(vec,nbins);          % Plot the histogram
histResults = [centers;counts]';  % Histogram results
```

A.3.5.2 Gaussian Curve-Fitting

The script shown in this section are excerpts from function

```
[histGaussCoeff,FWHM,areaRel,histGaussFitParams] = doHistGaussFit(
    histogramResults,histGaussPeaks,c)
```

In the script of the function, the variable `histGaussPeaks` is a 2D matrix that contains the starting fitting parameters for the peak intensity and position in the first and second columns, respectively. The fitting function to use is defined according to the number of peaks selected by the user on the GUI of Figure A.1(c). The starting points and upper and lower limits for the fitting are defined from the parameters in the variable `histGaussPeaks` and the fluorescence lifetime distribution (variables `x` and `y`) is fitted with the standard MATLAB function `fit`. From the fitting results, the Gaussian coefficients (intensity, position and width of each curve) are extracted and the FWHM is calculated using a developed `calculateFWHM` function.

```
histGaussFitNCurves = size(histGaussPeaks,1);   % number of peaks selected by
    the user
fitfunc = sprintf('gauss%d',histGaussFitNCurves); % fitting function
startPoint = zeros(1,3*histGaussFitNCurves);
for ii = 0:histGaussFitNCurves-1
  % Define the starting points of each parameter
  startPoint(1+ii*3) = histGaussPeaks(ii+1,2);
  startPoint(2+ii*3) = histGaussPeaks(ii+1,1);
  startPoint(3+ii*3) = c;
end
% Define upper and lower values around the starting points
lower(1:3:3*histGaussFitNCurves) = startPoint(1:3:3*histGaussFitNCurves)*0.7;
upper(1:3:3*histGaussFitNCurves) = startPoint(1:3:3*histGaussFitNCurves)*1.5;
% (this is also done for all the others...)
% Do the fitting
histGaussFitParams = fit(x,y,fitfunc,'StartPoint',startPoint,'Lower',lower,'
    Upper',upper);
% Get the function coefficients fromt he fitting results
% fi = ai*exp(-((x-bi)/ci)^2)
histGaussCoeff = coeffvalues(histGaussFitParams);
FWHM = calculateFWHM(histGaussCoeff); % FWHM of each curve
```

A.3.6 Reduced Fluorescence Lifetime Distribution Image

The script shown in this section are excerpts from function

```
getLifetimeDistributionImage(imageAxes,inStruct,sIndex)
```

After the fluorescence lifetime distribution is calculated, the interceptions of the Gaussian curves are calculated and saved in the variable `distInterceptions`. In the script of this function it is sorted which pixels belong within each of the intervals defined by consecutive interceptions, according to Equation 4.2. The upper and lower limits of

each lifetime intervals are saved in the variables l1 and l2, respectively. The central values bi are then saved in the variable lifeMatrix according to the interval to which each pixel belongs to form the reduced fluorescence lifetime distribution image.

```
% define the limits l1 and l2 such that all pixels with l1<tau<l2 receive the same values.
l1 = zeros(NCurves,1);  % lower limit
l2 = zeros(NCurves,1);  % upper limit
l1(1) = 0;  % Lowest lifetime limit = 0;
% Lower limit of each interval
l1(2:end) = inStruct(sIndex).lifetimes.histogramFit.distInterceptions(1:end);
% Upper limit of each interval
l2(1:end-1) = inStruct(sIndex).lifetimes.histogramFit.distInterceptions(1:end);
% Highest value possible is the x limit of the lifetime histogram
l2(end) = x(end);
% Center value of each distribuion
bi = double(coeff(2:3:end));
lifeMatrix = zeros(size(inStruct(sIndex).lifetimes.image));
for ii = 1 : NCurves % Create the distribution image
  lifeMatrix = lifeMatrix + bi(ii)*((l1(ii) < inStruct(sIndex).lifetimes.image) & (inStruct(sIndex).lifetimes.image <= l2(ii)));
end
```